Department of Physics and Astronomy
Heidelberg University

Bachelor Thesis in Physics
submitted by

Antonia Schaffert

born in Erlangen (Germany)

2024

Towards the precision measurement of a potential XUV-clock transition in highly charged lead

This Bachelor Thesis has been carried out by Antonia Schaffert at the
Max-Planck-Institute for Nuclear Physics in Heidelberg
under the supervision of
Apl. Prof. Dr. José R. Crespo López-Urrutia

Abstract

This thesis focuses on the spectra of different charge states of highly charged lead, which are analyzed using an electron beam ion trap (FLASH-EBIT) at the Max-Planck Institute for Nuclear Physics. The objective is to determine the energy of the metastable state $^2H_{11/2}$ in Pb XLII, the upper level for a potential extreme ultraviolet (XUV) clock transition more precisely. The energy of this metastable state was first determined in [1] to be 31.2(8) nm
The lead atoms injected in the EBIT are collisionally ionized by the electron beam, which can produce different charge states by varying the kinetic energy of the electrons. The energy at which Pb^{41+} is visible was determined, and a longer measurement was conducted at this energy to get more defined line positions and to be able to distinguish weak lines from the background. The results were compared to theoretical calculations using the Flexible Atomic Code and AMBiT.
The energy of the metastable state determined in this thesis is 32.044 ± 0.010(stat) ± 0.011(sys) eV
and is in agreement with the experimental and theoretical values from previous measurements.

Zusammenfassung

Diese Arbeit befasst sich mit den Spektren verschiedener Ladungszustände von hochgeladenem Blei, die mit einer Elektronenstrahl-Ionenfalle (FLASH-EBIT) am Max-Planck-Institut für Kernphysik analysiert werden. Ziel ist es, die Energie des metastabilen Zustands $^2H_{11/2}$ in Pb XLII, dem oberen Niveau für einen möglichen extremen ultravioletten (XUV) Atomuhrenübergang, genauer zu bestimmen. Die Energie dieses metastabilen Zustands wurde erstmals in [1] als 31.2(8) nm bestimmt.
Die in die EBIT injizierten Bleiatome werden durch den Elektronenstrahl stoßionisiert, der durch Variation der kinetischen Energie der Elektronen verschiedene Ladungszustände erzeugen kann. Die Energie, bei der Pb^{41+} sichtbar ist, wurde bestimmt, und es wurde eine längere Messung bei dieser Energie durchgeführt, um genauere Linienpositionen zu erhalten und schwache Linien vom Hintergrund unterscheiden zu können. Die Ergebnisse wurden mit theoretischen Berechnungen des Flexible Atomic Code und AMBiT verglichen.
Die in dieser Arbeit ermittelte Energie des metastabilen Zustands beträgt 32.044 ± 0.010(stat) ± 0.011(sys) eV und steht in Übereinstimmung mit den experimentellen und theoretischen Werten aus früheren Messungen.

Contents

1 Introduction

Optical atomic clocks are used to measure time with extremely high precision and serve as advanced frequency standards [2]. Some optical clocks using single-ion Paul traps have reached stable frequency until $2 \cdot 10^{-16}/\sqrt{\tau/\mathrm{s}}$ [3]. With this high precision, a standard for frequency measurements is set, and one can search for physics beyond the standard model. Temporal or spatial variation of fundamental constants [4][5] or violations of Einstein's equivalence principle through tests of local position invariance [6] are some examples of research beyond the standard model, which make use of such stable frequency standards.
Highly charged ions (HCIs), such as highly charged lead, are ions that have lost a great part of their shell electrons. The low-energy transitions have been shifted to higher energies, and therefore, HCIs are well-suited for next-generation optical clocks at a higher energy range.
In order to find stable clocks in the extreme ultraviolet (XUV) range, metastable states at high energies are needed. This is because they decay very slowly, making their spectral lines narrow and allowing for more accurate energy determination. Recently, such a metastable electronic state has been found in highly charged, Nb-like lead [1] using mass spectrometry in a Penning-trap [7]. In the next step, a more precise wavelength determination is needed before setting up a suitable laser system to study the transition in laser spectroscopy and eventually use it for an XUV clock. An optical clock based on the transition found in [1] would greatly benefit from further improvements in the precision of its known transition wavelength. Such long-lived states cannot be probed with standard spectroscopic methods. Therefore, this experiment presents complementary measurements by measuring decay pathways, allowing the determination of the energy of the metastable state via Ritz combination. These and other adjacent transitions are identified, and their energies are determined using an electron beam ion trap (EBIT) [8].
An EBIT provides a method of researching HCIs in the laboratory. It can produce and trap HCIs by ionizing neutral atoms with a compressed electron beam. These ions are trapped in the radial direction due to the space charge of the electron beam and in the axial direction due to a potential well. This simplifies the process of recording a spectrum by gathering a large amount of data over a long time period.

In this thesis, first, some theoretical foundations for HCIs, theoretical calculations, and EBITs are explained. This is followed by the experimental setup of the FLASH-EBIT used for measurements. Lastly, the spectra are analyzed and compared to spectra, which were generated with theoretical calculations. The identified transitions, and especially the ones relevant to the determination of the energy of the metastable states, are described. The conclusion gives a summary and an outlook on the continuation of the research on this potential clock candidate.

2 Theoretical foundations

For the understanding of the data in this experiment and the comparison to theoretical calculations, some foundations of atomic physics are necessary. The relevant information will be explained in this chapter. First, some basics of atomic configurations and electronic transitions are described. This is followed by the structure of highly charged lead, which is researched in this experiment. Afterward, the methods for the theoretical calculation of the lead spectra are presented. Lastly, the atomic processes inside an electron beam ion trap (EBIT) and its principles are illustrated.

2.1 Highly charged ions

The ions of interest for this experiment are highly charged ions (HCIs); in particular, highly charged lead is analyzed. HCIs have lost a large number of shell electrons and, therefore, have a high positive charge and a simpler shell structure compared to neutral atoms of their elements.
Often, HCIs are identified with the element that has the same number of electrons in neutral atoms. So, for example, 41 times positively charged lead with the atomic number $Z = 82$ as Pb^{41+} is Nb-like because Niobium has 41 electrons and the atomic number $Z = 41$.

2.2 Atomic shells

When filling up the shell of an atom or ion with electrons, the optimal distribution is that which minimizes the energy, called the energetic ground state. However, not all electrons can be in the same energy state due to the Pauli principle [9]. This states that two electrons must be distinguishable in at least one of the first four quantum numbers in Table 2.1 and can, therefore, not be in the same state. This leads to $2n^2$ electrons fitting into each shell and $2l + 1$ electrons in each subshell,

where n is the principal and l is the orbital quantum number.
In order to minimize the energy, the electrons always fill the least energetic subshell before filling the next least energetic subshell.

2.3 Level notation

An overview of all relevant quantum numbers is displayed in Table 2.1. The first four are the main quantum numbers.

Table 2.1: Quantum numbers describing the properties of electrons in an atomic shell and their notation

Quantum number	Quantity	Symbol and values
Principal	Shell assignment	n: 1, 2, 3, ...
Orbital	Orbital angular momentum	l: 0, 1, 2, ..., n-1
Magnetic	Magnetic angular momentum	m_l: $-l$, ..., -1, 0, 1, ..., l
Spin	Spin angular momentum	m_s: $-\frac{1}{2}$, $\frac{1}{2}$
Angular momentum	Total angular momentum	j: $\|l-s\|$, $\|l-s\|+1$, ..., $l+s$
Secondary ang. mom.	Angular momentum projection	m_j: $-j$, $-j+1$, ..., $j-1$, j

The electron configurations can be written as the occupancy for the different shells and subshells with the according number of electrons in each. The shells and subshells are labeled in letters, where the n = 1, 2, 3, 4, 5, ... of the shells correspond to K, L, M, N, O, ... and the l = 0, 1, 2, 3, 4, ... of the subshells correspond to s, p, d, f, g, ... Therefore in our example Pb^{41+} becomes: $1s^2$ $2s^2$ $2p^6$ $3s^2$ $3p^6$ $3d^{10}$ $4s^2$ $4p^6$ $4d^5$. The sum of the numbers in the exponents is 41, which is the number of electrons in Pb^{41+}. One can simplify this by comparing the electron configuration of the nearest noble gas. The configuration can then be written as [Kr]$4d^5$. This is because Krypton has three filled shells up to the M shell.

For each electron configuration, terms can be defined, which include the orbital angular momentum L and another quantum number, the spin angular momentum S. The multiplicity of the spin is given by $M = 2S + 1$. The term is defined by ${}^{M}L$.
In the classical case, all configurations with the same total electron spin S but different values of the orbital angular momentum L have the same energy. When considering spin-orbit interaction, this degeneracy is lifted. This is done by adding another quantum number for the total angular momentum $J = L+S$. The energy

level is then given by ${}^{M}L_J$.
In order to accurately describe an energy state, one has to give the additional magnetic quantum number m_J. An energy state is fully defined with the magnetic quantum number m_J and its corresponding level ${}^{M}L_J$.

2.4 Selection rules

When measuring a certain spectrum, not all possible transitions are visible in the spectrum. This is because the conservation of energy and, angular momentum and certain symmetry rules have to be met. These selection rules include parity conservation, orbital angular momentum conservation, spin conservation, angular momentum conservation, and the rules for the magnetic quantum number. The according quantum number to each quantity is displayed in Table 2.1. An overview of each quantity with the corresponding selection rule is given in Table 2.2.

Table 2.2: Selection rules for atomic transitions based on parity conservation, orbital angular momentum conservation, spin conservation and angular momentum conservation

Physical quantity	Selection rule
Orbital angular momentum	$\Delta l = 0, \pm 1$
Spin	$\Delta S = 0$
Total angular momentum ($J = L + S$)	$\Delta J = 0, \pm 1$, but $J = 0 \nrightarrow J = 0$
Magnetic quantum number	$\Delta m = 0, \pm 1$

The transitions for which these selection rules apply are classically allowed transitions and more probable than transitions, where at least one selection rule mentioned in Figure 2.2 does not apply. These are called "forbidden" transitions and have a much lower transition probability than allowed transitions. If a state has the option to de-excite via an allowed or a forbidden transition, it will most likely decay with the allowed path.
These selection rules are one reason why some atomic lines in a spectrum are stronger than other lines. Another cause is the difference in cross sections for certain processes, which will be explained in section 2.9.1. The spectral lines can only be measured if their intensity is distinguishable from the noise of the measurement coming mainly from the electronic readout. This makes it difficult to directly measure forbidden transitions.

2.5 Metastable states

Metastable states are useful for clock transitions due to their longer lifetime compared to other excited states. Therefore, they have a narrow linewidth, allowing for more accurate energy determination. This is often because all their possible transitions are forbidden according to the selection rules (see Table 2.2).
The electron state investigated in this work and relevant for XUV clock research [1] is a metastable state and is shown in Figure 2.1 at $J = \frac{11}{2}$ with a theoretical energy of 31.518 eV. Even though the transition to the ground state is forbidden because the total angular momentum would be $\Delta J = 3$, it will still decay by this path since there are no other options, as can be seen in the Grotrian diagram in Figure 2.1. However, the transition rate is far too low compared to noise and neighboring transitions to be able to be measured with an electron beam ion trap (EBIT).

2.6 Structure of Pb^{41+}

The charge state of lead with the atomic number $Z = 82$ researched in this experiment is Pb^{41+}, which has been stripped of 41 electrons and, therefore, has 41 electrons left. This means it has a ground state configuration of $[Kr]4d^5$ with five electrons in the 4d-subshell (see section 2.3). These are relevant for the transitions which are observed in the experiment.
A Grotrian diagram containing the energy levels and M1-transitions needed to calculate the energy of the metastable state is shown in Figure 2.1. It was generated using AMBiT calculations (see section 2.8.2). M1-transitions are magnetic dipole transitions. They couple states with the same parity in contrast to E1-transitions (electric dipole transitions), which couple states with different parity. Because this presents a violation of the classical selection rules, the M1-transitions have lower transition probabilities than E1-transitions. However, the transition probabilities are still higher than those of the metastable state presented in [1] because it violates fewer selection rules and is, therefore, less forbidden.
Therefore, typical spontaneous emission coefficients for E1-transitions are $A_{21} = \frac{1}{g_2} \cdot 2.0261 \cdot 10^{15} \frac{S'_{12}}{\lambda^3}$ and $A_{21} = \frac{1}{g_2} \cdot 2.6972 \cdot 10^{10} \frac{S'_{12}}{\lambda^3}$ for M1-transitions [10]. The transition rates for M1-transitions are a factor 10^5 weaker than E1-transitions.
On the x-axis of the Grotrian diagram in Figure 2.1, the quantum number J is marked. The energy levels are placed on multiples of $J = \frac{1}{2}$. This is because of the relations of the quantum numbers described in Table 2.1. The energy is marked

on the y-axis and calculated with the Hartree-Fock method, explained in section 2.7.

Since the electron state relevant for XUV clock research [1] is a metastable state and, therefore, has a long lifetime, it cannot be measured with an EBIT. However, by measuring the wavelength of an excited state decaying to this metastable state and the wavelengths of the decay path of this excited state to the ground state, one can calculate the wavelength of the metastable state. So, the relevant transitions to calculate the wavelength of the metastable state are:

1. $J = \frac{7}{2}$: 30.485 eV $\longrightarrow$ $J = \frac{5}{2}$: 0.000 eV (ground state)
2. $J = \frac{9}{2}$: 60.417 eV $\longrightarrow$ $J = \frac{7}{2}$: 30.485 eV
3. $J = \frac{9}{2}$: 60.417 eV $\longrightarrow$ $J = \frac{11}{2}$: 31.788 eV (metastable state)

These transitions are the strongest ones related to the metastable state and, therefore, measurable in the presented experiment. They have the additional benefit of being in a similar wavelength range. This means they can all be detected by the used spectrometers.
After determining the exact wavelengths for these three transitions experimentally, one can calculate the wavelength of the metastable state by adding energy 2 and energy 1 and then subtracting energy 3 of the list.
With the relation

$$E = \frac{hc}{\lambda} \tag{2.1}$$

one can determine the energy of this metastable state via the wavelength.

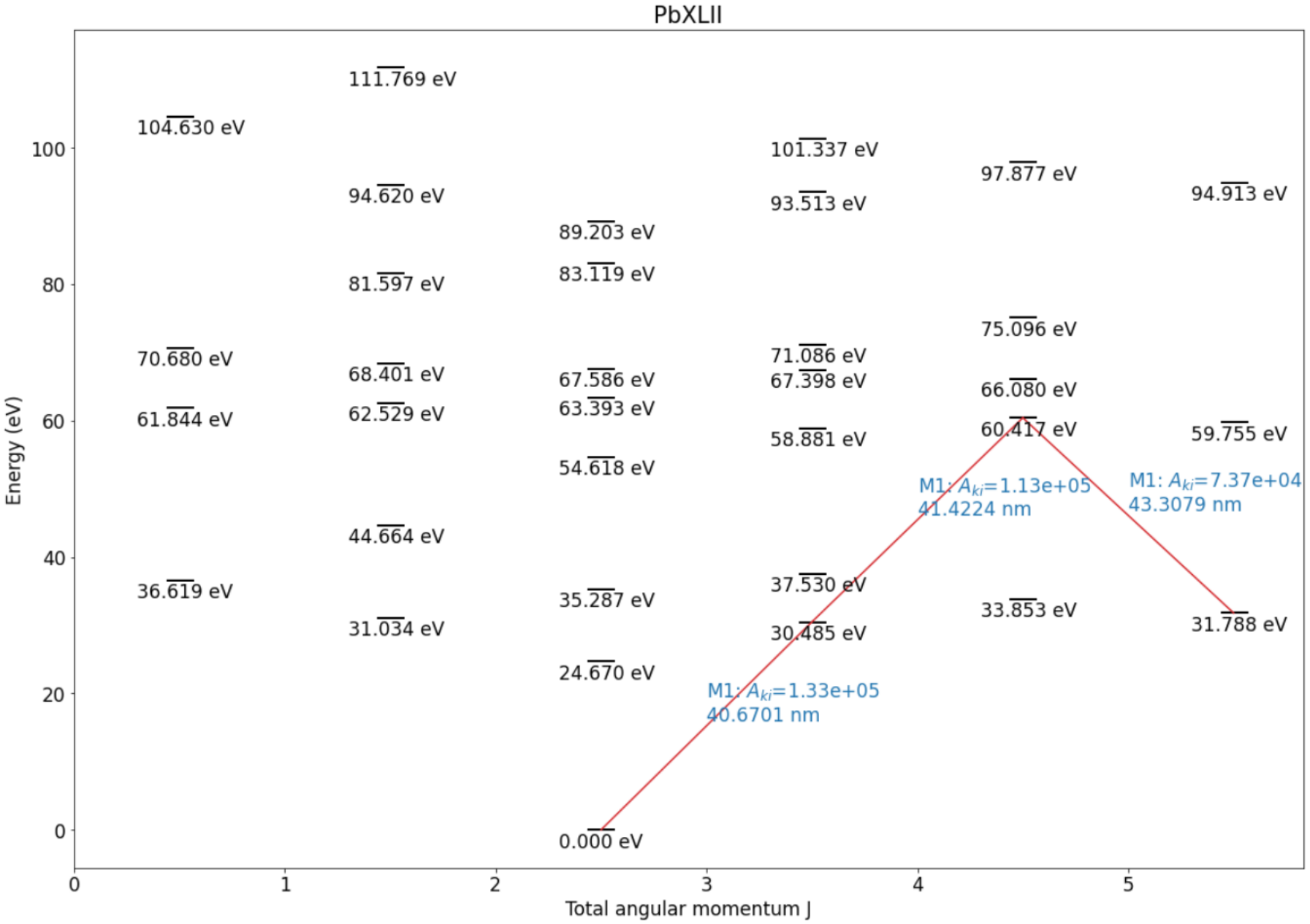

Figure 2.1: Grotrian diagram of Pb[41], the relevant decay path for this experiment is marked in red with the according type of transition, intensity, and transition wavelength in blue

2.7 Configuration interaction

The hydrogen atom only has one electron and is, therefore, the simplest atomic system and the only one with an analytically solvable electronic structure. For multi-electron systems with N electrons, such as neon or lead, the electronic structure has to be solved numerically.
One method for calculating the energy levels of each electron in a multi-electron system is the Hartree-Fock method, which is described in detail in [11]. It is an approximate solution of the stationary Schrödinger equation [9], achieved by combining many single-particle wave functions [9] for one electron configuration.

Another, more advanced method to solve a multi-electron system is configuration interaction (CI) [12], which is also used for the flexible atomic code (FAC [13]). Compared to the Hartree-Fock method, it also includes interaction between electron configurations in the form of basis functions of more than one configuration. The distribution of the electrons on each possible energy state is described by a Slater determinant [9]:

$$\Psi(\vec{r}_1, \vec{r}_2, ..., \vec{r}_N) = C \begin{pmatrix} \Psi_1(\vec{r}_1) & \Psi_1(\vec{r}_2) & ... & \Psi_1(\vec{r}_N) \\ \Psi_2(\vec{r}_1) & \Psi_2(\vec{r}_2) & ... & \Psi_2(\vec{r}_N) \\ ... & ... & ... & ... \\ \Psi_N(\vec{r}_1) & \Psi_N(\vec{r}_2) & ... & \Psi_N(\vec{r}_N) \end{pmatrix} \tag{2.2}$$

When taking the sum of the Slater determinants for different electron configurations, one gets a total wavefunction Ψ_{CI} [9]:

$$\Psi_{\mathrm{CI}}(\vec{r}, \vec{s}) = \sum_i c_i \Psi_i \tag{2.3}$$

where $\vec{r}$ is the location vector and $\vec{s}$ is the spin of an electron. The wavefunctions Ψ_i in the form of Slater determinants of each configuration can be obtained via the Hartree-Fock method [11] mentioned before. The weighting of these wavefunctions is determined by the coefficients c_i, which can be calculated by diagonalizing the Hamiltonian for N electrons, including electron-electron interaction for the non-relativistic case [9]:

$$\hat{H}_{\mathrm{tot}} = -\sum_{i=1}^{N} \left(\frac{\hbar}{2m} \Delta_{r_i} + V(\vec{r}_i) \right) + \sum_{j>i} \frac{e^2}{|\vec{r}_j - \vec{r}_i|} \tag{2.4}$$

In order to obtain the energy of a certain state, including components of configuration interaction, one can solve the Schrödinger equation [9]:

$$\hat{H}\Psi(\vec{r}, t) = E\Psi(\vec{r}, t) \tag{2.5}$$

The more configurations are considered, the more accurate the solution becomes. However, the dimension of the Hamiltonian matrix needed to determine the state coefficients c_i grows exponentially with the number of configurations included.

2.8 Theoretical calculations

The theoretical spectra in sections 4.2.2 and 4.3.2 were calculated with the software packages flexible atomic code (FAC) [13] and AMBiT[14]. The methods and their differences are described in the following sections.

2.8.1 FAC calculations

The flexible atomic code (FAC) uses configuration interaction (section 2.7) to determine the energies of atomic states. With these, the transition and collisional excitation probabilities, which are dependent on the kinetic energy of the electrons, can be calculated. These rates are determined using the single multipole approximation and Coulomb-wave Born approximation, both described further in [13].
In order to determine a theoretical spectrum, in addition to the transition rates, the populations of the excited states are needed. This is because the number of radiative transitions can be calculated from the population of the excited state as seen in equation (2.17). The populations can be obtained using a collisional radiative model, which is explained elaborately in [15]. In this model, a set of linear differential equations, which describe the populating and depopulating rates of an electronic state, is solved numerically.
For the calculation of a theoretical spectrum, the collisional excitation rate is equated with the radiative deexcitation rate. For this, the electron energy and density have to be inserted in the calculation. For this experiment, the electron energy was determined for each charge state using the experimental setup, and the electron density was chosen to be $5 \cdot 10^{10}$ cm^{-3}.
With the information on the energies of the atomic states and the transition rates and populations, one can calculate the theoretical spectra for different charge states of atoms.

2.8.2 AMBiT calculations

AMBiT calculations are based on the combination of configuration interaction (section 2.7) and many-body perturbation theory (MBPT) [16]. The electrons are divided into the relatively inert core electrons, calculated via the Hartree-Fock method (see section 2.7), and the valence electrons and hole, calculated with MBPT.
First, the basis orbitals of the core electrons are generated, and the configuration interaction between them is calculated. It is responsible for the main part of the solution, and the MBPT calculations add a small correction afterward. This is because the configuration interaction basis captures most of the energy of the atomic states, and the core-valence correlations and virtual core excitations can be treated as a perturbation. Their contributions are included in the total energy in second-order MBPT.
The resulting wavefunctions of the combination of configuration interaction and MBPT are used to calculate the transition matrix elements for electric, magnetic, and hyperfine multipole operators. The transition matrix elements are proportional to the wanted transition rates
The theoretical spectrum can then be generated for several charge states around Pb^{41+}. These results are then compared to the FAC calculations and the experimental data.

2.9 Atomic processes

There are several possible interactions between electrons and ions, leading to the production of ions and radiation inside an electron beam ion trap (EBIT). The relevant processes will be explained in this section.

2.9.1 Collisional ionization

Collisional ionization occurs mostly in the trap region between electrons and ions and is largely responsible for producing highly charged ions inside an EBIT. For this process, the kinetic energy E_{kin} of the impacting electron e^- has to be greater than the ionization potential E_{ion} of the target ion A with charge q. In that case, the shell electron with sufficiently low binding energy E_{ion} is ejected from the ion. Highly charged ions are produced when this process is repeated several times. The

reaction can be described with the following equation [17]:

$$A^{q+} + e^-(E_{\text{kin}}) \rightarrow A^{(q+1)+} + e^-(E_{\text{kin},1}) + e^-(E_{\text{kin},2}) \tag{2.6}$$

with the energy, which has to be conserved during the process:

$$E_{\text{kin}} - E_{\text{ion}} = E_{\text{kin},1} + E_{\text{kin},2} \tag{2.7}$$

The total cross section σ_{tot} can be calculated using the Lotz-formula [18]:

$$\sigma_{\text{tot}} = \sum_i \sigma_i = \sum_i a_i \frac{\ln(E_{\text{kin}}/P_i)}{E_{\text{kin}} P_i} \left(1 - b_i e^{-c_i\left(\frac{E_{\text{kin}}}{P_i} - 1\right)}\right) \tag{2.8}$$

where the index i describes the different electronic shells. The empirical constants a_i, b_i, and c_i are specific to different elements and charge states (for some examples, see also [18]), and P_i are the binding energies of the electrons.
Equation (2.8) indicates that the cross-section increases with increasing kinetic energy until it reaches a maximum at around $2\pi - 3\pi$. Therefore, during the measurements, the energy was always set to just below the energy, at which the next charge state would be produced in order to maximize the cross-section and, with it, the ion population and line intensity.

2.9.2 Collisional excitation

When a free electron and an ion collide, it is also possible for an electron to be excited into a higher energy state. This excited ion $[A^{q+}]^*$ can then either decay with a photon emission or autoionize afterward. The process of collisional excitation can be described with [17]:

$$A^{q+} + e^-(E_{\text{kin,in}}) \rightarrow [A^{q+}]^* + e^-(E_{\text{kin,out}}) \tag{2.9}$$

Due to energy conservation, the following equation can be applied:

$$E_{\text{kin,in}} - E_{\text{kin,out}} = E_{\text{transition}} \tag{2.10}$$

Therefore, the difference between the kinetic energy of the incoming electron $E_{\text{kin,in}}$ and the outgoing electron $E_{\text{kin,out}}$ has to be equal to the energy of exciting an electron into a higher energy state $E_{\text{transition}}$.

2.9.3 Radiative recombination

When a free electron collides with an ion, the electron also has the possibility to recombine in one of these vacant places. The energy is emitted in the form of a photon [17]:

$$A^{q+} + e^-(E_{\text{kin}}) \rightarrow A^{(q-1)+} + \hbar\omega_\gamma \tag{2.11}$$

Due to energy conservation, the photon energy has to be equal to the kinetic energy of the electron and the binding energy E_{binding} of the captured electron in the atomic shell:

$$\hbar\omega_\gamma = E_\gamma = E_{\text{kin}} + E_{\text{binding}} \tag{2.12}$$

2.9.4 Dielectronic recombination

Dielectronic recombination takes place when a free electron recombines with an ion and also excites a shell electron of the ion into a higher energy state. The ion is, therefore, excited and can either re-emit an electron (autoionization) or relax an electron and emit a photon, completing the dielectronic recombination. This process can be described by [17]:

$$A^{q+} + e^-(E_{\text{kin}}) \rightarrow [A^{(q-1)+}]^* \rightarrow [A^{(q-1)+}] + \hbar\omega_\gamma \tag{2.13}$$

This is a resonant process, and therefore, the kinetic energy of the electron has to be equal to the sum of its binding energy after recombination and the needed energy to excite the shell electron E_{exciting}. This leads to the following resonance condition [17]:

$$E_{\text{kin}} = E_{\text{binding}} - E_{\text{exciting}} \tag{2.14}$$

Due to this being a resonant process, it is very strong when electrons of the needed energy are present.

2.9.5 Spontaneous emission

An excited ion is always trying to reach a more stable electron configuration and, hence, minimize the energy of the system. Therefore, any atomic state except for the ground state may decay by the emission of a photon. This may happen

spontaneously or by external processes, such as a photon interaction with the ion. An example where this can happen is following collisional excitation. After an ion is excited during a collision, it can decay with the emission of a photon. This process can be described by:

$$[A^{q+}]^* \rightarrow A^{q+} + \gamma(\Delta E) \tag{2.15}$$

where the energy of the emitted photon corresponds to the energy difference ΔE between the state from which the electron decayed and the state to which it decayed. This state does not have to be the ground state but can also be a lower excited state, which can decay again.
It is not possible to determine exactly when this decay will happen, but an effective lifetime or average time until the state decays τ can be given to certain transitions. The exponential and time dependant decay of a population N of excited ions can then be described by [9]:

$$N(t) = N(t = 0)e^{-t/\tau} \tag{2.16}$$

Consequentially, the intensity of the emitted radiation I is given by:

$$I \propto \left|\frac{dN(t)}{dt}\right| = \frac{N(t = 0)}{\tau}e^{-t/\tau} \tag{2.17}$$

2.10 Principle of an electron beam ion trap

EBITs [19] produce highly charged ions by electron impacts using an electron beam. The process is described more in detail in section 2.9.1 and is limited by the energy of the electron beam. The electrons of this beam are emitted from a cathode and accelerated due to a difference in potential from the center of the trap and the cathode. On their way, they pass through an external magnetic field, which compresses the electron beam and guides it toward the center of the trap. There, the positively charged ions are trapped radially due to the negative space charge of the electron beam and axially due to electrodes, which build an electrostatic potential well to trap ions. In the last step, the electron beam reaches the collector electrode and is absorbed there, closing the electric circuit. Compared to many other ways of producing HCIs, the ions inside of an EBIT have a mean velocity of zero.

2.10.1 Space charge

The negative space charge of the electron beam is an integral part of an EBIT because it is responsible for the radial trapping of ions. However, it causes the energy that is set between the cathode and the center of the trap to be larger than the actual energy of the electron beam. Therefore, it has to be corrected by the space charge, which depends on the current and the energy that is set.
Using the approximation that the electron beam is an infinitely long cylinder of constant charge density ρ_e and radius r_H, the charge density can be described by [20]:

$$\rho_\mathrm{e} = \frac{I_\mathrm{e}}{\pi r_H^2 v_\mathrm{e}} \tag{2.18}$$

where I_e is the electron beam current, and v_e is the velocity of the electrons in the longitudinal direction. When inserting this into the Poisson equation for electrostatics:

$$\vec{\nabla}^2\Phi = -\frac{\rho_\mathrm{e}}{\varepsilon_0} \quad \Rightarrow \quad \frac{1}{r}\frac{\partial}{\partial r}\left(r\frac{\partial}{\partial r}\Phi\right) = -\frac{\rho_\mathrm{e}}{\varepsilon_0} \tag{2.19}$$

and looking at the two cases for $r \leq r_\mathrm{H}$ and $r > r_\mathrm{H}$ respectively, one gets an expression for the space charge as a function of the radius r [20]:

$$\Phi(r) = \begin{cases} \Phi_\mathrm{D} + \frac{I_\mathrm{e}}{4\pi\varepsilon_0 v_\mathrm{e}}\left[\left(\frac{r}{r_\mathrm{H}}\right)^2 + 2\ln\left(\frac{r_\mathrm{H}}{r_\mathrm{D}}\right) - 1\right] & r \leq r_\mathrm{H} \\ \Phi_\mathrm{D} + \frac{I_\mathrm{e}}{4\pi\varepsilon_0 v_\mathrm{e}} 2\ln\left(\frac{r}{r_\mathrm{D}}\right) & r > r_\mathrm{H} \end{cases} \tag{2.20}$$

where Φ_D is the potential at the surface of the central drift tube with inner radius r_D. This expression only contains constants and the parameters I_e and v_e. For this experiment, a classical description of the kinetic energy of the electrons with mass m_e can be assumed as the relativistic effects are low. For the classical approach, the velocity of the electron can be calculated with the following formula:

$$E_\mathrm{kin} = \frac{1}{2} m_\mathrm{e} v_\mathrm{e}^2 \tag{2.21}$$

For the relativistic approach, the velocity can be calculated with [9]

$$E_\mathrm{kin} = \left(\frac{m_\mathrm{e}}{\sqrt{1 - \left(\frac{v_\mathrm{e}}{c}\right)^2}} - m_\mathrm{e}\right) \cdot c^2 \tag{2.22}$$

where c is the speed of light. The results for the highest velocities in this experiment are $v_{\mathrm{e,classic}} = 2.875 \cdot 10^7\ \mathrm{m\,s^{-1}}$ and $v_{\mathrm{e,rel.}} = 2.865 \cdot 10^7\ \mathrm{m\,s^{-1}}$ and deviate the most. Since this is a relative difference of less than $0.4\,\%$ and the error calculated in section 4.1.3 is considerably larger, the relativistic effects are negligible.
Therefore, the classical expression is used, and the space charge can be calculated by multiplying a constant C_1 with a term depending on the current and the kinetic energy of the electrons in the electron beam:

$$\Phi = C_1 \frac{I_\mathrm{e}}{\sqrt{E_\mathrm{kin}}} \tag{2.23}$$

The constant with the unit $\left[\frac{\sqrt{\mathrm{eV}}}{\mathrm{mA}}\right]$ can be calculated from experimental measurements.

3 Experimental setup

After giving a short overview of the theoretical foundations, the experimental setup is described in this chapter. First, some essential parts of the FLASH-EBIT and their purpose are described. Since the most important part of the observation are the spectrometers, these are explained in more depth. Lastly, the measurement scheme of the different types of measurements is stated, as well as the mathematical determination of line position in these measurements.

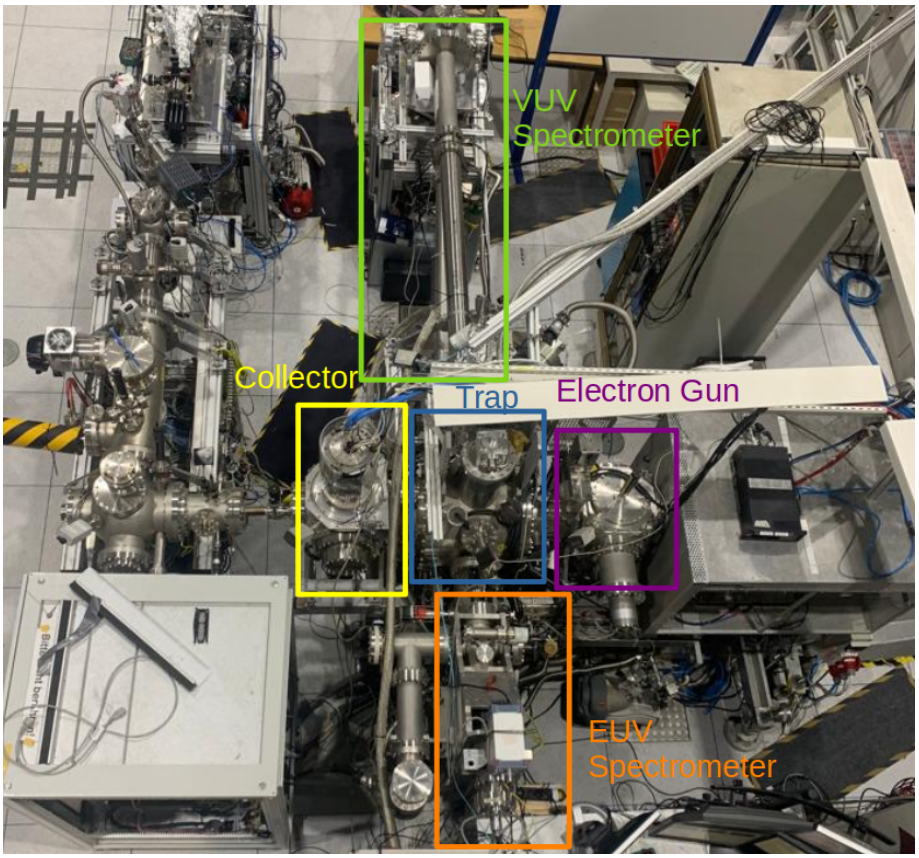

Figure 3.1: Birdseye view of FLASH-EBIT located at the Max-Planck-Institute for Nuclear Physics. The parts of the EBIT relevant to this experiment are labeled

3.1 FLASH-EBIT

The electron beam ion trap (EBIT) used in this experiment is the FLASH-EBIT [21], located at the Max-Planck Institute for Nuclear Physics in Heidelberg. Figure 3.1 shows a picture of the EBIT. The fundamental principles of an EBIT have been explained in section 2.10. In this section, the individual components of the FLASH-EBIT are described.

3.1.1 Electron gun

In order to start all processes inside an EBIT, the electron gun has to produce free electrons inside an electron beam. A model and scale of the electron gun and individual parts built into the FLASH-EBIT are shown in Figure 3.2.

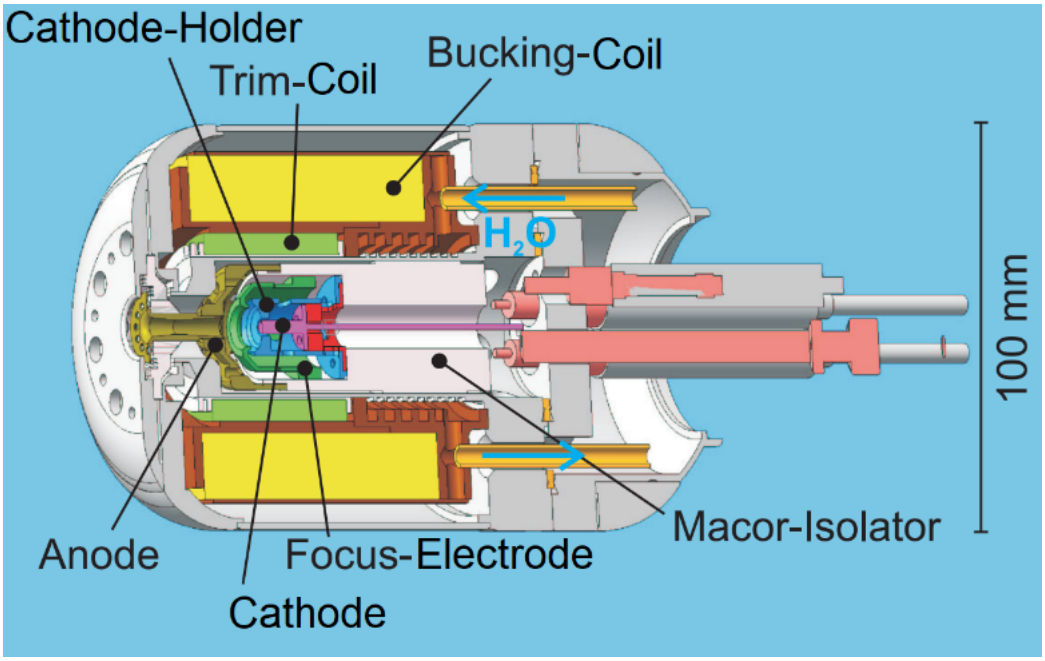

Figure 3.2: Model of the electron gun installed in FLASH-EBIT, adapted from [21]

The cathode inside the electron gun produces free electrons, which make up the electron beam. The cathode is made up of a tungsten-barium matrix [21] and heated to about 1300 K - 1500 K.
A focus electrode and an anode are placed in front of the cathode to produce a

steady stream of electrons. Tuning the potential of these electrodes allows controlling the emission current [21].
The cathode is surrounded by two magnetic coils, the bucking and trim coils. The bucking coil compensates for the strong magnetic field from the superconducting Helmholtz coils. The purpose of this is to focus the beam even further because the diameter of a beam that originates in a place without a magnetic field and then passes through one is smaller than that of a beam that originates in a place with a magnetic field [22]. The trim coil is responsible for fine-tuning the adjustment of the beam position but was not used in this experiment.
Since this setup with the cathode heater produces much heat, it is cooled by a water chiller connected to the gun socket.

3.1.2 Trap region

The free electrons produced by the cathode are accelerated towards the trap due to the potential difference between the cathode and the center of the trap. The trap of the FLASH-EBIT consists of nine copper trap electrodes, also known as drift tubes (DT). Seven are cylindrically shaped (electrodes C1, C2, C3, G1, G2, G3, and the electron in the center labeled "trap" in Figure 3.3), and the two outermost electrodes have a trumpet form (electrode trumpet C and G in Figure 3.3).

The trumpet drift tubes at each end of the trap region guide the electron beam in and out of the trap and shield the region of thermal radiation from warmer parts of the EBIT.
The potential on the drift tubes can be set individually to trap the ions axially. In this experiment, the drift tubes neighboring the central drift tube were set to the highest potential to keep the highly charged ions close to the center. Going outward, the drift tubes were set to lower potentials.
The central drift tube has the largest diameter and is labeled "trap" in Figure 3.3 because it is the main part of the trap. The potential of this drift tube is usually low in order to trap more ions. However, if one wants to eliminate unwanted ions from previous measurements or emitted by the cathode, a high positive potential can also be set. This can be done in a periodic interval and is called "dumping". The central drift tube also has some openings in the material, through which the neutral gas can be injected into the trap, and the photons can escape, leading them toward the spectrometers.
One can also set all drift tubes to a positive potential U_{DT}, also known as "drift

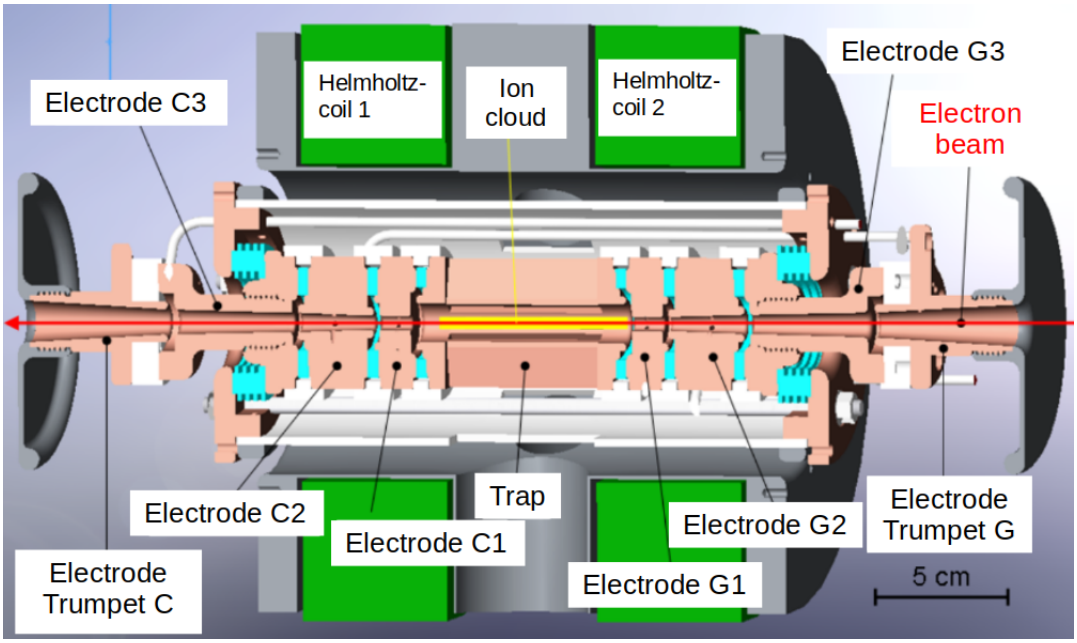

Figure 3.3: Model of the trap region and Helmholtz coils built in FLASH-EBIT, where the electron beam goes from right to left, adapted from [23]

tube bias", which contributes to the kinetic energy of the electrons:

$$E_{kin} = e(U_{\mathrm{DT}} - U_{\mathrm{cathode}} + \Phi) \tag{3.1}$$

where e is the elementary charge, U_{cathode} is the voltage of the cathode, and Φ is the space charge, for which an approximation is given in section 2.10.1. It is responsible for the radial trapping of the ions.
The whole region is connected to a cooling system based on liquid helium. This has the benefit of improving the achievable vacuum so that the electron beam does not interact with the residual gas before even reaching the trap region, where it is supposed to interact with the injected neutral gas. Residual gas can come from previous measurements, water vapor, or small leaks. Water vapor is present because the pumps cannot extract the condensation water inside the EBIT very well, and it can, therefore, evaporate. For this reason, some oxygen can always be detected in the trap.

3.1.3 Collector

After the electron beam has passed through the trap region, it decelerates due to the electric field produced by the drift tubes and then absorbed by the collector,

closing the electric circuit. It is made up of a hollow copper electrode, a suppressor, and an extractor. A model and scale of the collector and individual parts, which is built into the FLASH-EBIT, is shown in Figure 3.4.

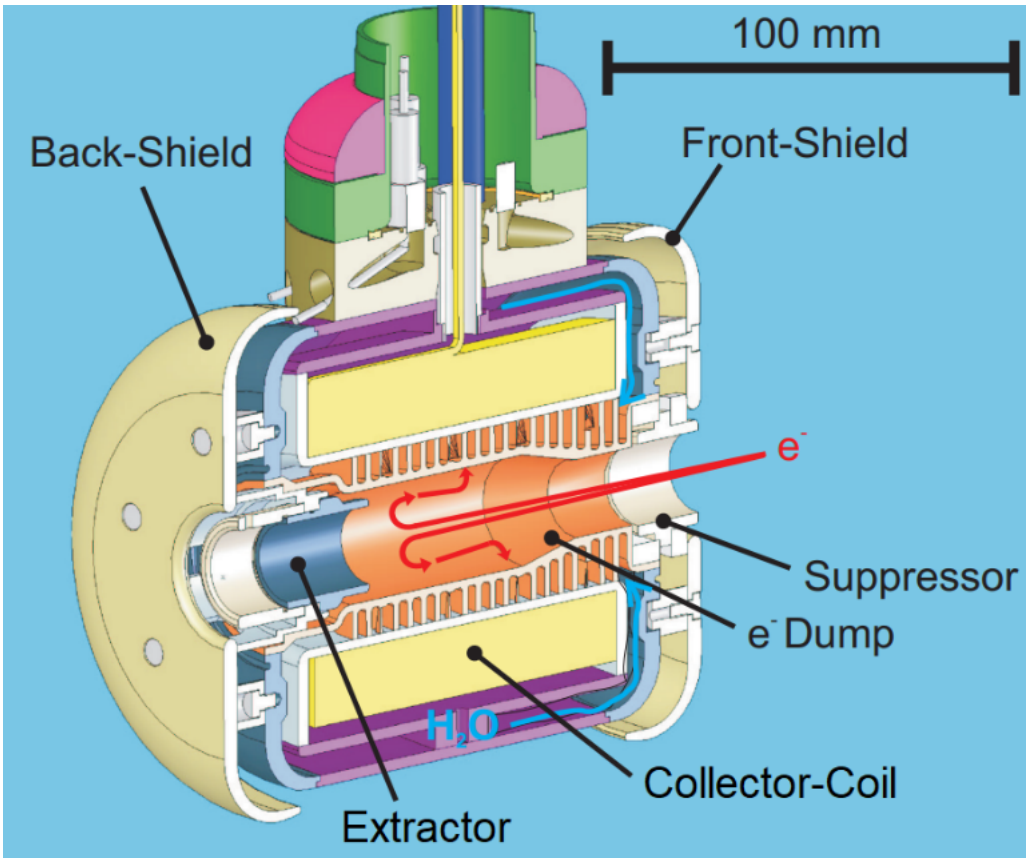

Figure 3.4: Model of the collector installed in FLASH-EBIT, adapted from [21]

The electron beam coming from the trap region has a high kinetic energy of a few kilo-electronvolts and, therefore, must be decelerated before reaching the collector to avoid damaging the EBIT.
The extractor at the end of the collector is set to a negative voltage higher than the cathode voltage, which achieves some defocusing of the electron beam and forces the electrons to turn around. Therefore, they do not puncture the collector. In addition, a collector coil around the collector compensates the magnetic field, which leads to further defocusing of the beam. The beam can be widened even further by setting potentials on the front-shield, back-shield, and suppressor electrodes. The suppressor has a slightly negative potential, which prevents the secondary electrons from leaving the collector. These secondary electrons are produced when the hollow electrode comes into contact with the electron beam.

The already widened beam reaches the inner walls of the collector, which absorbs the electrons. This heats the collector. Therefore, it is also connected to the water chiller, similar to the electron gun.

3.1.4 Magnetic field

In order to achieve a high current density of the electron beam, it has to be compressed and, therefore, focused by a magnetic field. For achieving a strong magnetic field of up to 6 T, the FLASH-EBIT has a superconducting pair of Helmholtz coils built in. These are built around the trap region, contributing to the radial trapping of the ions, as shown in Figure 3.3. The distance between the two coils is larger than in the usual Helmholtz coil setup because the magnetic field in the center of the trap region should remain nearly constant.
Since the magnets have to be superconducting to achieve a magnetic field of this strength, they have to be cooled cryogenically to about 4 K. This is done with liquid helium.

3.1.5 Injection system

The neutral atoms, which are turned into HCIs, are injected into the trap region by a differentially pumped injection system, which shapes them into an atomic beam. The atoms are then collisionally ionized and form an ion cloud. As a source for these atoms, a gas has to be injected. For lead, this can be done in the form of tetraethyl lead $(C_2H_5)_4Pb$. Neon, used for the calibration, and oxygen, used for optimizing the line width with the autofocus function, were injected directly as a gas because they are gaseous at room temperature. Therefore, for measurements with lead, there can be some contamination of carbon, but the measurements with neon and oxygen should not be contaminated.

In Figure 3.5, one can see that the gas injector consists of a dosing valve and two different chambers. The valve controls the amount of gas injected and acts as a nozzle. The two chambers are responsible for the differential pumping because they are divided by an aperture, which allows the pressure in the first chamber to have a maximum pressure of $5 \cdot 10^{-4}$mbar and still have a pressure of $5 \cdot 10^{-9}$mbar in the trap region. Another aperture is placed between the second chamber and the rest of the EBIT. This leads to two different pressure stages in each chamber and another pressure in the EBIT.

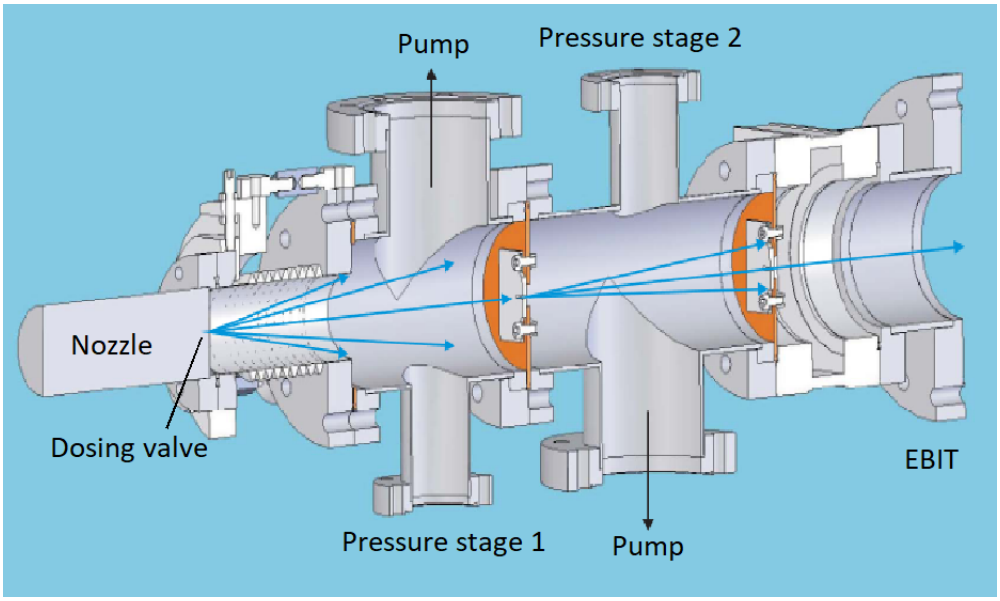

Figure 3.5: Model of the injection system installed in the FLASH-EBIT and the different pressure stages, adapted from [24]

The injection pressure p_{inj} mentioned in the following section 3.3 refers to the pressure in the first chamber of the injection system.

3.2 Detection system

Another essential part of this experiment is the detection system. The FLASH-EBIT has three detectors, each built differently and measuring other wavelength ranges, namely vacuum ultraviolet (VUV), extreme ultraviolet (EUV), and X-ray. Technically, VUV is defined as 10 nm to 200 nm, EUV as 10 nm to 121 nm and X-ray as 5 pm to 10 nm. However, in this experiment, the EUV detector measures between about 29 nm and 44 nm, the VUV detector between 55 nm and 110 nm, and the X-ray detector detected photons of at least 200 eV. Due to the wavelength ranges of the EUV and VUV spectrometer, the first order of a spectral line can be detected by the EUV spectrometer and the second order of the grating by the VUV spectrometer. The second order is produced at the double wavelength because of the reflective gratings in the spectrometers (shown in Figures 3.10 and 3.6). One can also detect the third or fourth order of strong lines.
The functionality of each of these detectors with the belonging spectrometer is described in the following section.

3.2.1 EUV spectrometer

The EUV spectrometer installed at FLASH-EBIT consists of two microchannel plates (MCP) [25] and a diffraction grating. The spectrometer is shown in Figure 3.6.

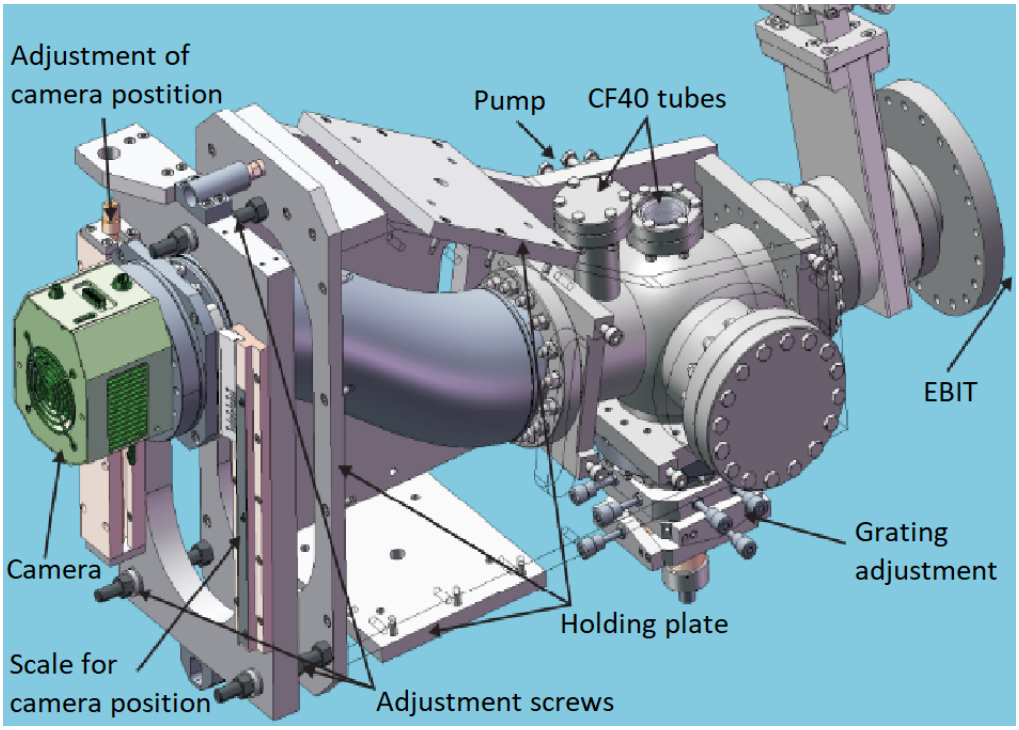

Figure 3.6: Model of the EUV spectrometer installed in FLASH-EBIT, adapted from [24]

An MCP is an array of holes in an insulating glass layer with two metal plates at the top and bottom. The holes act as miniature electron multipliers, tilted towards the metal plates' normal by 8°. This ensures that the arriving particles will impact the inner walls of the electron multipliers, which are coated with a semiconductor material. Due to this material, the impacting particle releases electrons and can replenish the charge with the help of an external voltage source.
The two metal plates of the MCP can be set on a high voltage potential difference, the plate on the back side being more positive than the front side. In this experiment, a voltage difference of 2400 V was used. Therefore, the electrons released from the semiconducting material are accelerated towards the more positive side. The accelerated electrons can hit the inner walls again, which leads to more

electrons being released. The resulting electron cascade is collected at the back side of the detector. This means that a particle entering the detector provokes an amplification of a factor of about 10^3 to 10^4, which can be detected easily.
In the FLASH-EBIT, two MCPs are stacked on top of each other with the electron multipliers tilted in different directions. This is called the "Chevron configuration" [25] and can be seen in Figure 3.7. With this configuration, one can detect particles even if they hit the detector at an angle of exactly 8° and would not be detected by just one detector. This leads to increased efficiency. In addition, the amplification of both MCPs is multiplied, leading to an amplification factor of at least 10^7.

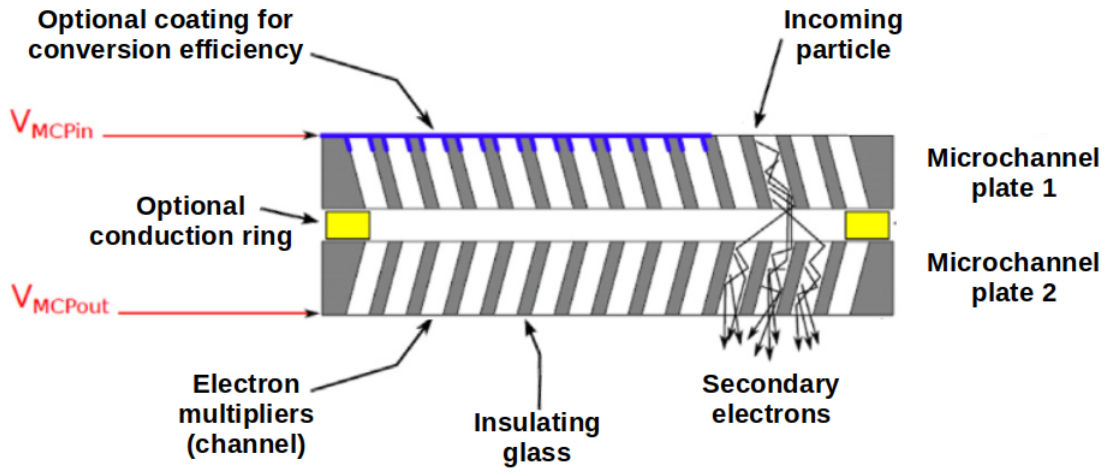

Figure 3.7: Chevron configuration using two microchannel plates. An incoming photon releases an electron in one of the channels upon impact, which accelerates. When this electron hits the wall of a channel again, secondary electrons are released, causing a cascade. Figure adapted from [26]

To find out where the incoming particle hit the MCP and, therefore, in which miniature electron multiplier or channel, a delay line anode [27] is installed. It consists of two wires, forming a mesh over the back side of the detector, as shown in Figure 3.8. The wires detect the electron cascades and transport them to the signal-processing electronics. Because of the particular shape of the wires, the delay time between the signals on each end of the wire can be assigned to the corresponding channel of the MCP.
However, the wires can have unwanted bends, leading to data errors. This effect can be seen when calibrating the EUV detector.

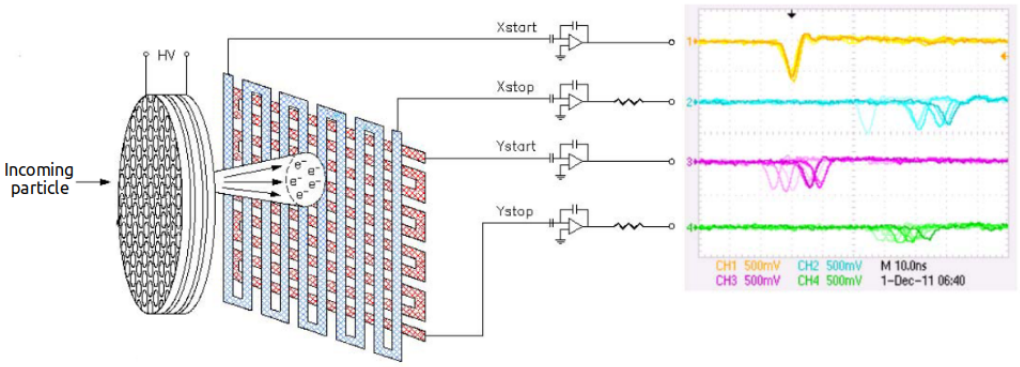

Figure 3.8: Delay line readout of the microchannel plate with exemplary signals, where one can see the shift in the signals for the corresponding position on the detector, adapted from [28]

Before reaching the MCP, the photons produced in the trap region are diffracted on a flat-field diffraction grating. The grating is located inside the chamber shown in Figure 3.6. The MCP can be moved up and down on the focal plane to change the angle and, hence, the wavelength of the photons that hit the MCP. The grating is designed for wavelengths between 5 nm and 35 nm. However, it can also be used for higher wavelengths, such as in this experiment, but the efficiency is lower than 36.3 % compared to the maximum efficiency at around 11 nm [24]. Therefore, before starting the measurements, the detector was moved higher to detect the expected wavelengths and then left at this position for all measurements.
The mounting of the MCP has three adjustable screws, as shown in Figure 3.6, which are responsible for the tilt of the MCP towards the left or right and towards the grating. This tilt can be varied in order to find the best focusing and, therefore, minimal line width at a certain height of the MCP. This was done as one of the preparatory measurements and is described in section 4.1.2.

When analyzing the data of the EUV spectrometer, some corrections have to be applied. First, the data has to be rotated because the MCP is not placed perfectly orthogonal on the dispersive axis of the grating. Since it is difficult and practically impossible to place it perfectly, it is easier to rotate the data afterward. This can be done by taking data of a strong line and dividing it into left and right sides of the detector. When looking at the projection of each side, the lines of each half should be at the same position.
After the data is rotated, a region of interest has to be chosen on the detector of which data to use when generating a spectrum. Due to the round shape of the MCP, the region of interest is round as well. Therefore, the spectrum has to be

weighted depending on the width of the region of interest at this position.
Lastly, the errors due to deformations in the delay line wires must be corrected. This can be done by finding a strong line and then moving the detector. If this is done evenly across a large part of the region of interest, some deformations can be made visible. These can be interpolated to a resulting shift matrix for the deformations of the MCP.
These corrections were done in previous work [29] on the FLASH-EBIT. Since no relevant changes were applied to the EBIT in the meantime, these corrections were used on all the data in this experiment. The spectra were compared to spectra without rotation and shift matrix to verify that these corrections enhance the data. It was confirmed that the line width remained minimal for the spectra with both corrections.

3.2.2 VUV spectrometer

The VUV spectrometer installed in FLASH-EBIT also uses a microchannel plate (MCP) as a detector and a concave grating with a 6 m radius to reflect the photons coming from the trap region. A photograph of the grating chamber of the VUV spectrometer is shown in Figure 3.9.

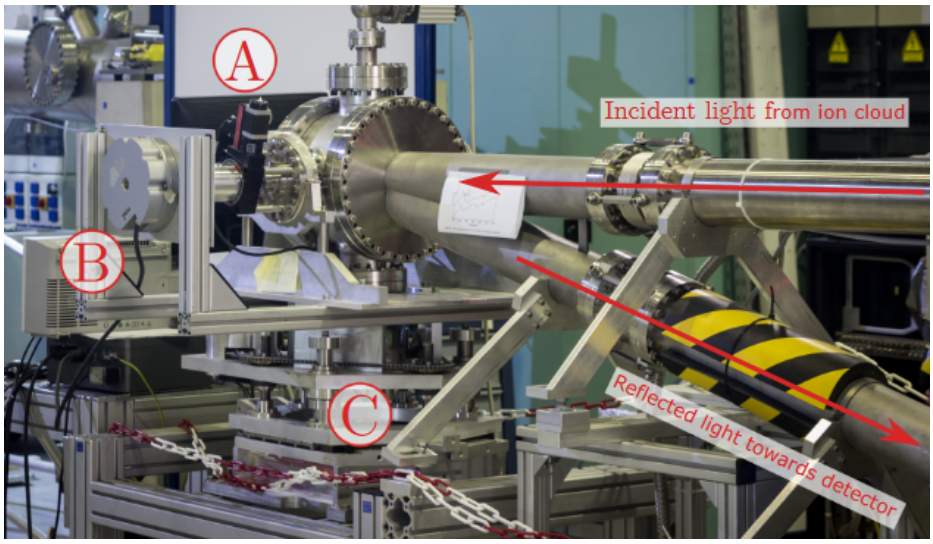

Figure 3.9: Photograph of the grating chamber of the VUV spectrometer with **A:** rotation stage used to generate the rotations, **B:** rotary encoder to measure the grating angle and **C:** mechanism for aligning the height of the grating, taken from [30]

Due to the concave grating, the spectrometer is similar to the simple reflective spectrometer published by Rowland [31]. A Rowland circle [31] as seen in Figure 3.10 of the same radius as the concave grating describes that the light of a point source on this circle is refocused onto another point on the same circle. The relation between the radius of the curved grating and the Rowland circle is by a factor $\frac{1}{2}$. Therefore, if the radius $2R$ of the is 6 m, then the entrance slit in the trap region, the grating, and the detector have to be on a circle with a radius R of 3 m. This leads to a fixed angle of 15° between the incident and reflected light, which is guided through tubes shown in Figure 3.9.

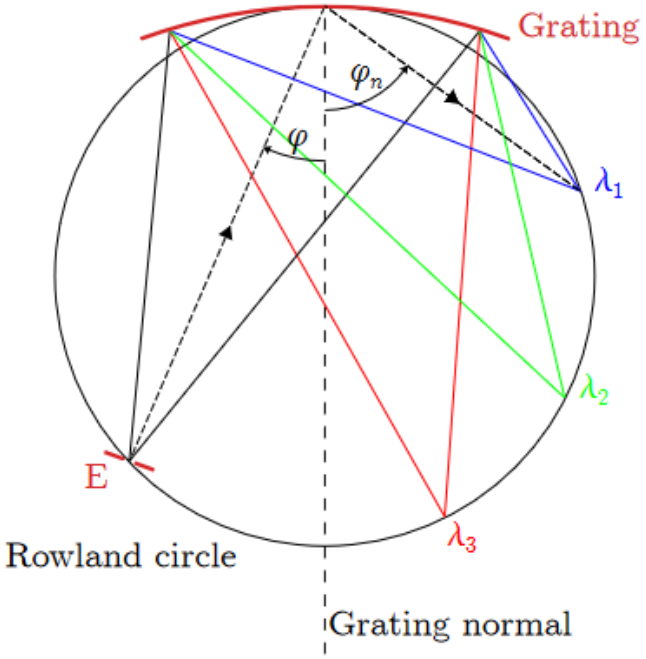

Figure 3.10: Rowland circle with an entrance slit E, where the incident light reaches the grating with angles φ and ist reflected to the focal positions λ_1, λ_2, λ_3 of the spectrometer on the circle with angles φ_n. The grating has a radius of $2R$ compared to the radius R of the Rowland circle, taken from [30]

In order to measure at different spectral ranges with the detector, the grating is rotated with respect to the incident light. In Figure 3.10, this means a change in the angle of incidence φ and a change in the reflection angle φ_n. For the detector to stay in the focal plane, it has to be moved according to the angle of the grating. The motor responsible for the position of the detector is linear. The position in dependence of the angle of the grating was part of the preparatory measurements and is described in section 4.1.1.

The detector used for the VUV range is an MCP, which was already explained in section 3.2.1. For increased efficiency, again, a chevron configuration [25] with two MCPs is installed. The choice of an MCP as the detector is very relevant for the VUV spectrometer because it has a time resolution, which is essential when assigning a count to the grating angle at that moment.
To read out the position of the incident photon, a wedge and strip anode is installed in the VUV spectrometer [32]. It calculates the center of a charge cloud using an algorithm based on the principle of charge partition. This charge cloud has a diameter of a few millimeters because a homogenous electronic field accelerates the electrons between the MCP and the anode.
A wedge and strip anode consists of discrete, nested electrodes installed on an insulating substrate. Half of the electrodes are wedges pointing in opposite directions, while the other half consists of complementary rectangles whose height is constant in total but whose height ratios vary across the anode, as shown in Figure 3.11. The wedge electrodes are responsible for the x-coordinate, while the strip electrodes are responsible for the y-coordinate.

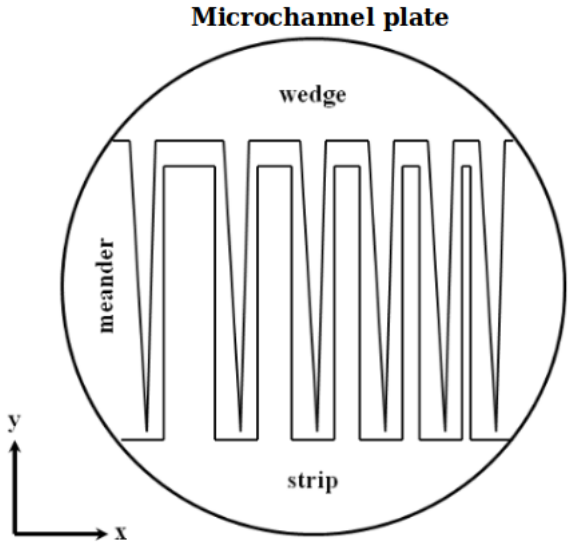

Figure 3.11: Model of a wedge and strip anode placed, such as the one placed on the back of an MCP in the VUV spectrometer, taken from [33]

In order to be able to encode the x- and y-coordinates linearly, the width of the electron cloud has to be about double the period width of the anode structure. The width can be varied by changing the electric field strength between the MCP and the anode. However, at the margin of the anode, some distortions occur because the whole electron cloud cannot be detected by the anode. This issue can be solved by reducing the size of the active anode area.

3.2.3 X-Ray detector

In order to detect x-rays produced in the trap region, a silicon drift detector [34] is installed at the FLASH-EBIT. A schematic representation can be found in Figure 3.12.

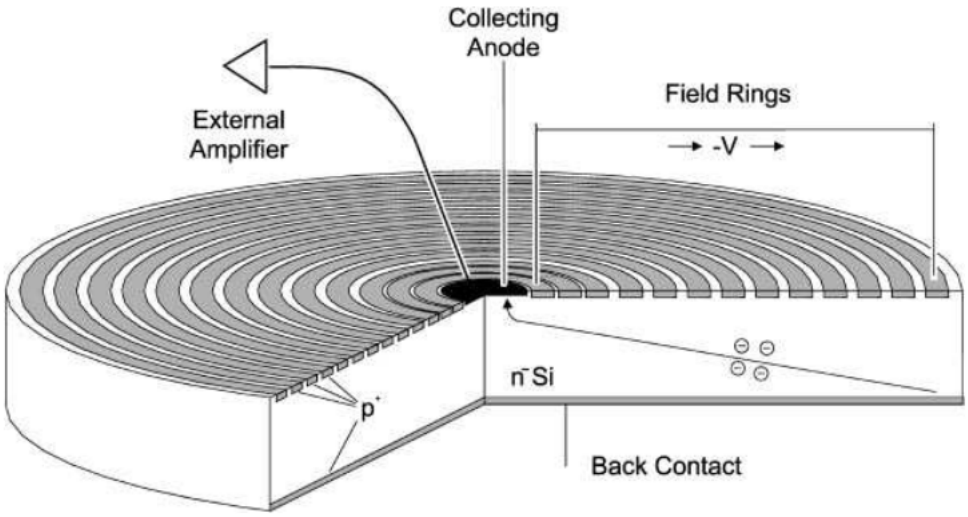

Figure 3.12: Schematic representation of a silicon drift detector. When photons impact on the detector, electron-hole pairs are produced, which are transported towards the collecting anode in the center. Figure taken from [34]

A silicon drift detector is a semiconductor detector consisting of an n-doped silicon cylinder. On the front side of the detector, p-doped rings are mounted with an n-doped anode in the center, which has a positive potential. The back of the detector has a p-doped contact with a negative potential.
Applying an external voltage between the negative potential of the p-doped rings and the positive potential of the n-doped silicon cylinder generates a space charge region between them. When photons with a high kinetic energy hit the back of the detector, they produce electron-hole pairs. Due to the voltage difference, these pairs are separated, and the electrons drift towards the front side. In addition, they drift towards the positive collecting anode in the center.
The potential of the rings increases stepwise in negativity towards the border of the detector, so the electrons fall towards the lowest potential, which is in the center. This distribution of the potential ensures that a large number of produced electrons are collected at the anode. Therefore, the efficiency and energy resolution

of the detector is improved.
When the electrons reach the anode, they produce an electrical pulse, amplified and converted into a digital voltage by the electronics. The height of the pulse is proportional to the energy of the recorded photon event.
The silicon drift detector measures the energy deposition of the X-ray photons instead of their position. The deposited energy of the photon is proportional to the number of electrons produced and, therefore, proportional to the strength of the signal.

3.3 Measurement scheme

During this experiment, three different types of measurements were conducted for various purposes: static measurements, energy ramps, and discrete energy scans. The functionality of these types of measurements, as well as their significance during this experiment, are illustrated in this section.

3.3.1 Static measurements

The purpose of static measurements is to do long-term measurements with constant settings to get a more resolved spectrum with enough events to have statistical significance. Static scans aid in determining line positions with higher accuracy and observing weaker lines, which can be mistaken for noise in shorter measurements.
This type of measurement was done with the EUV and VUV spectrometer in this experiment. The spectrometers can operate simultaneously and were therefore used at the same time in order to get a static measurement of the lead spectrum at an energy, where Pb^{41+} is visible, as can be seen in sections 4.2.2 and 4.3.2. The duration t_{meas} of this static measurement was around 65 hours.
The specific settings for the injected element, the cathode voltage U_{cathode}, voltage U_{focus} of the focus electrode, the current I, the drift tube bias U_{DT}, the injection pressure p_{inj}, the trap depth of the neighboring to the central drift tube U_{trap}, the dumping interval t_{dump} and voltage U_{dump} of the trap region, the bucking coil voltage U_{bucking} and the heater of the cathode I_{heater} can be seen in Table 3.1.
The higher the temperature of the cathode heater is set, the higher the current and countrate detected. However, with higher temperatures, more unwanted barium reaches the trap region and, therefore, the detectors. This makes it more challenging to interpret the resulting spectra.

Table 3.1: Settings of the EBIT for the static measurement

Element	U_{cathode} (V)	U_{focus} (V)	I (mA)	U_{DT} (V)	p_{inj} (mbar)	U_{trap} (V)	t_{dump} (s)	U_{dump} (V)
Pb	-1900	1500	197.6	380	$2.96{\cdot}10^{-7}$	30	40	200

Element	U_{bucking} (V)	I_{heater} (A)	t_{meas} (h)
Pb	0	1.29	65

3.3.2 Energy ramps

During these measurements with energy ramps, the energy of the electron beam is ramped to higher energies by changing the potential set on all drift tubes, the drift tube bias, according to equation (3.1). These ramps aim to identify processes that happen at a certain kinetic energy of the electron beam.
These energy ramps were conducted with the silicon drift detector to determine the space charge in section 4.1.3. The purpose of the ramps is to determine the energy at which dielectronic recombination takes place, as described in section 2.9.4. They are resonant processes and, therefore, have high amplitudes at specific electron beam energies.
In order to calculate the space charge, several measurements at different currents were conducted, meaning the resonances appeared at different electron energies in each measurement. With the channel position of the resonant peaks for each different measurement, the real energy of the resonant peaks can be extrapolated, and the space charge can be calculated.
When ramping the drift tube bias, the energy of the electron beam is being ramped as well. Additionally, a change in the electron beam current was observed. However, this is only a slight change that happens at energies higher than those of the resonant peaks, which are analyzed in section 4.1.3. They are, therefore, negligible for the measurements. The rest of the settings are constant during these measurements, as shown in Table 3.2. During this ramp time, t_{ramp}, the drift tube bias is constantly ramped to higher energies, and then the measurement is stopped.

Table 3.2: Settings of the EBIT for the energy ramps

Element	# measurements	U_{cathode} (V)	U_{focus} (V)	I (mA)	U_{DT} (V)	p_{inj} (mbar)
Pb	9	-1000	0 - 2000	41.2 - 162.8	0 - 3000	$5.8{\cdot}10^{-7}$

Element	U_{trap} (V)	dump	U_{bucking} (V)	I_{heater} (A)	t_{ramp} (s)
Pb	420	off	0	1.29	100 - 200

3.3.3 Discrete energy scans

For discrete energy scans, the energy of the electron beam is also varied, but in discrete steps. The energy of the electron beam can either be adjusted by setting the drift tube bias or the voltage of the cathode, as stated in equation (3.1). After the energy of the electron beam is set to each discrete value, the settings are held constant for the duration t_{step} of the measurement until the next energy of the electron beam is set.
The purpose of this type of measurement is to get an indication of how the spectrum changes at different energies and especially see at which energies new lines appear and, therefore, the ionization energy for a new energy level is reached.
These discrete energy scans are conducted with the EUV and VUV spectrometers simultaneously to see the same phenomena in both spectrometers. A continuous ramp of the energy, as presented in section 3.3.2, is more suited for this function, but the VUV grating is permanently rotating to produce a spectrum. If both settings change continuously, it becomes too difficult to determine which count belongs to which angle of the grating and to which energy. Therefore, the spectrum could not be generated.
These energy scans were conducted with neon for the calibration, as explained in section 4.1.4 and with lead in order to determine which lines belong to the charge state Pb^{41+}, as seen in sections 4.2.1 and 4.3.1. For both scans, the voltage of the cathode was varied. However, for the scan with lead, the maximal voltage of the cathode was reached, so for the last step of the scan, the drift tube bias was increased instead of the cathode voltage. This results in a lower count rate for the last step. This is because the ions are mostly produced in the trap center, but some also drift in from outside. These ions cannot enter the trap center if the drift tube bias is set to high voltages because both are positively charged.
Because these steps in electron beam energy are discrete, they are interpolated

in between to generate intensity matrices. Therefore, the lines do not necessarily appear at the energy where they are shown to appear but at an unknown energy between the energy step before and the step after. For the energy scans with neon, the steps were kept small with $U_{\text{step}} = 10\,\text{eV}$, but due to time issues, the steps during the scans with lead are $U_{\text{step}} = 50\,\text{eV}$, as shown in Table 3.3.
Most of the settings were kept constant during the whole scan. However, when changing the cathode voltage, the energy of the electron beam and, therefore, the current also changes. This results in a varying space charge. Since the error of the determination of the space charge in section 4.1.3 is larger than this variation, it was assumed to be constant.

Table 3.3: Settings of the EBIT for the discrete energy scans

Element	# steps	U_{cathode} (V)	U_{focus} (V)	U_{step} (V)	I (mA)	U_{DT} (V)
Ne	23	-(50 - 300)	70	10	2.9 - 8.7	0
Pb	8	-(1650 - 2000)	1700	50	196.4 - 216.7	300 - 350

Element	p_{inj} (mbar)	U_{trap} (V)	t_{dump} (s)	U_{dump} (V)	I_{heater} (A)	U_{bucking} (V)	t_{step} (min)
Ne	$8.87{\cdot}10^{-6}$	30	20	300	1.19	0.7	50
Pb	$2.83{\cdot}10^{-7}$	30	60	150	1.29	1	180

3.3.4 Line position determination

The position and width of spectral lines, including errors, are determined the same way in each part of the experiment. The lines are approximated using a Gaussian function [35]:

$$f(x) = \frac{1}{\sqrt{2\pi\sigma^2}} \exp\left(-\frac{1}{2}\left(\frac{x-\mu}{\sigma}\right)^2\right) \tag{3.2}$$

where σ is the standard deviation or the width of the line and μ is the mean or the expected position. Since the Lorentz profile vanishes in the resolution of the detector and the Doppler width, a Gaussian distribution is valid.
The Gaussian is fitted on the spectral line using a least-square technique. In this method, the best fitting function is determined by minimizing χ^2, which is given

by the following formula [36]:

$$\chi^2 = \sum_{i=1}^{n} \frac{(y_i - f(x_i))^2}{\sigma_i^2} \tag{3.3}$$

where x_i and y_i are the data points, $f(x)$ is the function to be fitted, in this case, a Gaussian, and the σ_i are the errors of the individual data points, determined through the fit. The reduced χ^2_{red} can be calculated by dividing the χ^2 by the degrees of freedom, which are the number of measured values minus the number of parameters and should be close to 1.
The errors $\Delta\lambda_{\text{fit}}$, $\Delta\sigma_{\text{fit}}$ of the parameters of the Gaussian are determined by diagonalizing an estimated approximate covariance of the optimal parameters [36]. For the calibration measurements, an additional error $\Delta\lambda_{\text{NIST}}$ of the NIST database was used. The total error was calculated with:

$$\Delta\lambda_{\text{tot}} = \sqrt{\Delta\lambda_{\text{fit}}^2 + \Delta\lambda_{\text{NIST}}^2} \tag{3.4}$$

4 Data analysis and results

In this chapter, the data will be analyzed. First, some preparatory measurements were done in order to optimize the line resolution for both spectrometers, determine the exact energy set between the cathode and the central drift tube, and calibrate both spectrometers. Afterward, measurements were conducted with lead to measure the transitions of interest in the first order with the EUV spectrometer and in the second order with the VUV spectrometer simultaneously with the same settings. Firstly, an energy scan was done to confirm that Pb^{41+} is visible and determine which lines belong to that charge state. After that, a longer measurement was conducted at a fixed energy, where the spectrum of Pb^{41+} was recorded. The measurements were then compared to the theoretical spectrum.

4.1 Preparatory measurements

Before being able to record the lead spectra, some preparatory measurements were carried out. First, the autofocus motor of the VUV grating (see section 3.2.2) was optimized using strong oxygen lines and different motor speed settings. Afterward, the EUV spectrometer was focused on the region of interest of the detector using the adjustable screws at the detector (see section 3.2.1). Lastly, the space charge of the EBIT was calculated for high electron energies. After these preparatory measurements, the spectra of lead can be analyzed, as shown in the following sections.

4.1.1 Autofocus optimization of the VUV spectrometer

Oxygen was injected into the EBIT to optimize the function of the autofocus motor. First, a spectrum of oxygen was taken to identify strong lines for the optimization. The strongest six lines were chosen, and the VUV grating was set to the angles of these lines separately. With different positions of the autofocus motor, the lines were recorded without rotating the grating, and the line width was

determined using a Gaussian least-square fit, as described in section 3.3.4. With these data points, a parabolic fit could be used to determine where the sigma width would be minimal. This and all following parabolic fits were done according to the least-squares method explained in section 3.3.4.
However, it became noticeable that changing the direction in which the autofocus motor moved increased the line width and changed the position, where the minimal width was expected. Hence, additional measurements were taken, where the speed of the autofocus motor was varied (Figure 4.1.1, left), and the hysteresis effect of moving back and forth (Figure 4.1.1, right) was analyzed. A parabola was fitted for each series of measurements, and the minima with corresponding motor position and line width were determined.

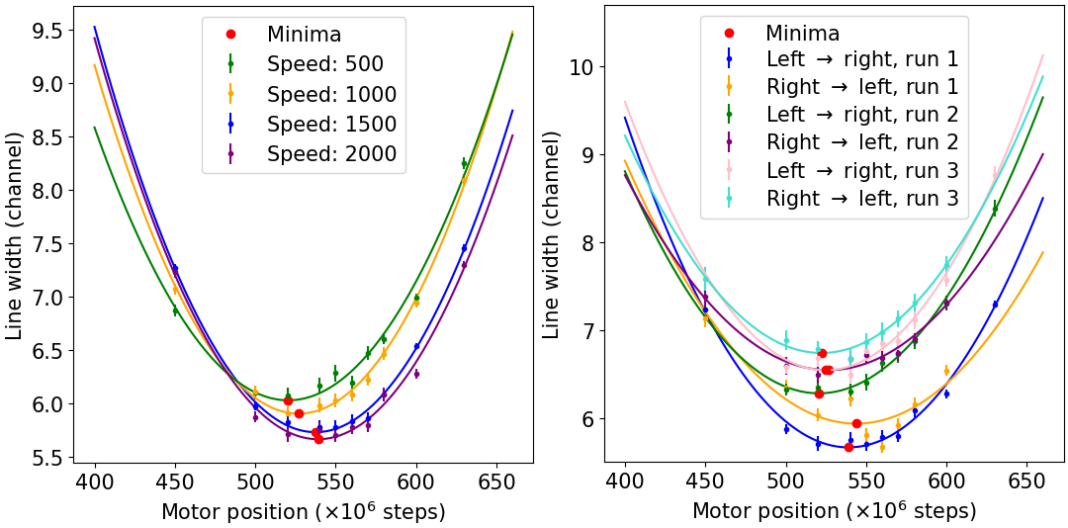

Figure 4.1: **Left:** line width at different motor positions with varied motor speed of the VUV autofocus motor in steps per second to determine the optimal position of the minimal line width. **Right:** Line width at different motor positions at changed direction to analyze the hysteresis effect

The speed in this Figure 4.1.1 is given in steps per second. The result of this series of measurements was that the fastest speed, 2000 steps per second, leads to the lowest sigma width and is therefore used for all following measurements. The measurements also confirmed that the sigma width increases when changing the direction of the motor movement in short intervals. Therefore, a multimeter was added to the experimental setup, which measures the resistance between two contact points on the rail of the motor, one in the middle and one at the end of the rail, further than the minimal position of the motor. The motor position in

steps and the resistance have a linear correlation, so they can easily be converted. Installing the multimeter reduced the hysteresis effect, but the value of the resistance and, therefore, the position strongly fluctuated. This leads to increased error bars in the y-direction. The error bar in the x-direction results from the position of the spectral line on the detector at a fixed angle. When taking the average fluctuation as the motor position, the position where the width is minimal could be determined again using a parabolic fit.
A parabola was determined for the autofocus function using the strongest six oxygen lines of the spectrum and the position of their minimal sigma width. This parabola is shown in Figure 4.2. The optimal motor position is described as a function of the angle θ of the grating with

$$x_{\text{motor}}(\theta) = -4.076 \cdot 10^4 \ \theta^2 - 7.275 \cdot 10^5 \ \theta + 2.718 \cdot 10^6 \tag{4.1}$$

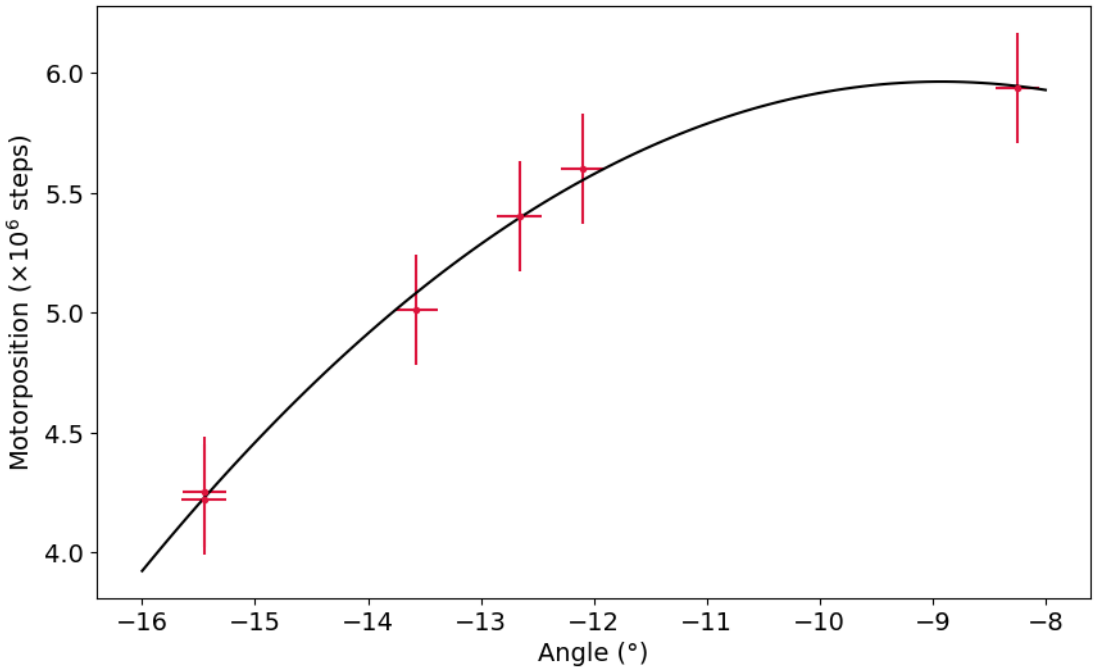

Figure 4.2: Polynomial for the autofocus function of the VUV focusing motor, the data points are the minimal positions for different spectral lines in oxygen. The error bar in the x-direction results from the position of the spectral line on the detector at a fixed angle. The error bar in the y-direction stems from the fluctuation on the encoder

4.1.2 Focusing of the EUV spectrometer

The EUV spectrometer was used for the main part of the experiment. In order to measure the expected wavelengths, it was moved far from its original position and, therefore, had to be focused again. This was done using three adjustable screws at the detector, with which it can be tilted left, right, and towards the grating, as described in section 3.2.1. Since the detector was already optimized towards left and right, the main changes were tried towards the direction of the grating.
These measurements were conducted with a closed injection, but some residual lead from previous measurements was still inside the trap. The width of certain lines was minimized to determine the spectral lines more accurately. Since the area of interest was expected to be seen between the middle and the top quarter of the detector, a line in that area was used to determine what the best position for the adjustable screws was. The spectra for different settings of the adjustable screws are shown in Figure 4.3.

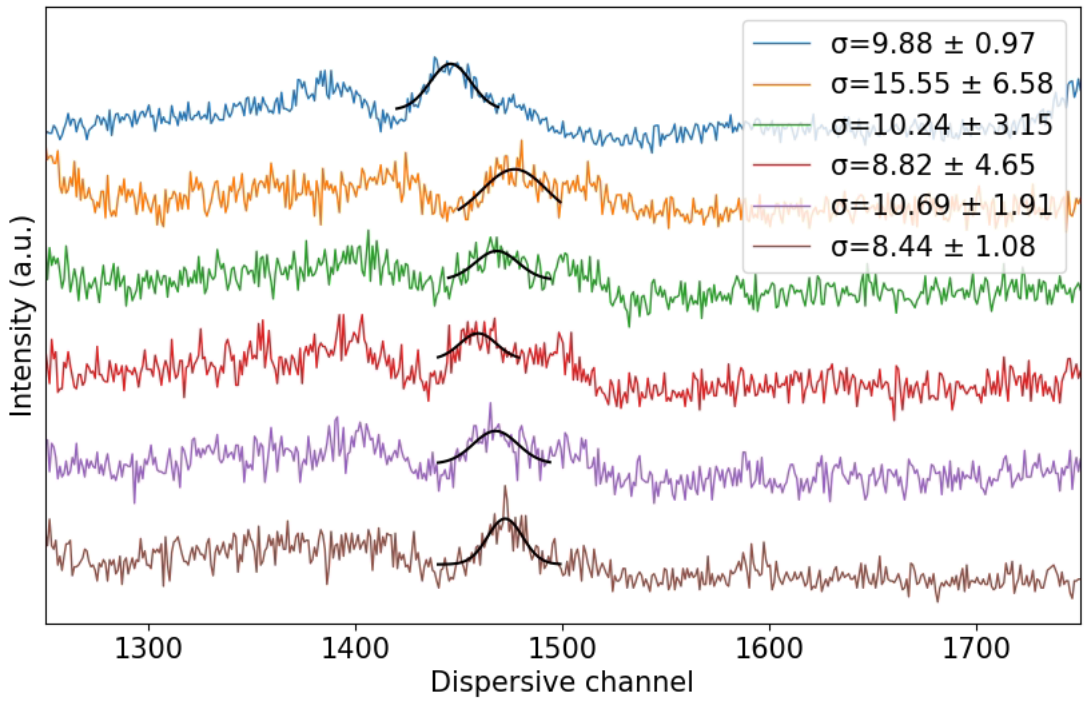

Figure 4.3: Gaussian least-square fit to find the minimal line width of a spectral line in the region of interest for EUV focusing. The measurements are time-normalized, and the width of the spectral line is shown in the legend

The line width was determined using a Gaussian least-square fit, described in section 3.3.4. Figure 4.3 shows a section of the spectrum where the line was optimized. The measurements were conducted starting from the top, and the last measurement was determined to be the optimal measurement, where the width was only $\sigma = 8.4 \pm 1.1$ channel. The measurements are time-normalized for better comparison.
After the optimal position was determined, the EUV detector remained in this position for all following measurements.

4.1.3 Space charge determination

The space charge of the electron beam is an integral part of an EBIT because it is responsible for the radial trapping of ions. However, it also shifts the electron energy according to equation 3.1, and therefore, the energy that is set between the cathode and the central drift tube is not equal to the energy of the beam itself.
The space charge potential is proportional to $\frac{I}{\sqrt{E_{\mathrm{kin}}}}$ as derived in section 2.10.1. By taking measurements of lead at different currents and electron beam energies, this ratio can be varied, and the space charge extrapolated to the currents and electron energies used for the main part of the experiment.
Dielectronic recombination (DR) is advantageous for determining space charge because each resonance only occurs at a specific electron energy. These were detected using the silicon drift detector of the EBIT described in section 3.2.3, which measures the X-ray spectrum. In order to find the exact electron beam energy at which the DR resonances occur, an energy ramp was conducted, as explained in section 3.3.2.

In Figure 4.4 one can see an example of an energy ramp. The top shows the photon energy dependent on the electron beam energy and the visible DR resonances. A projection was made onto the electron energy axis between the red lines to determine the position of these resonances. This projection is shown at the bottom. The positions of the resonances were determined using a least square Gaussian fit, as described in section 3.3.4.
The resonances in Figure 4.4 were determined with the help of FAC calculations as M-Nn resonances with $4 \leq n \leq 7$. This indicates that an electron is excited from the $n = 3$-shell to the $n = 4$-shell due to the recombination of another electron into the $4 \leq n \leq 7$-shell.
Figure 4.4 also shows that the thin lines of the MNN are specific resonances of different charge states, but especially for the MNO recombinations, only one broad peak is visible. The widths of these are approximately $\sigma_{\mathrm{broad}} = 196$ channel com-

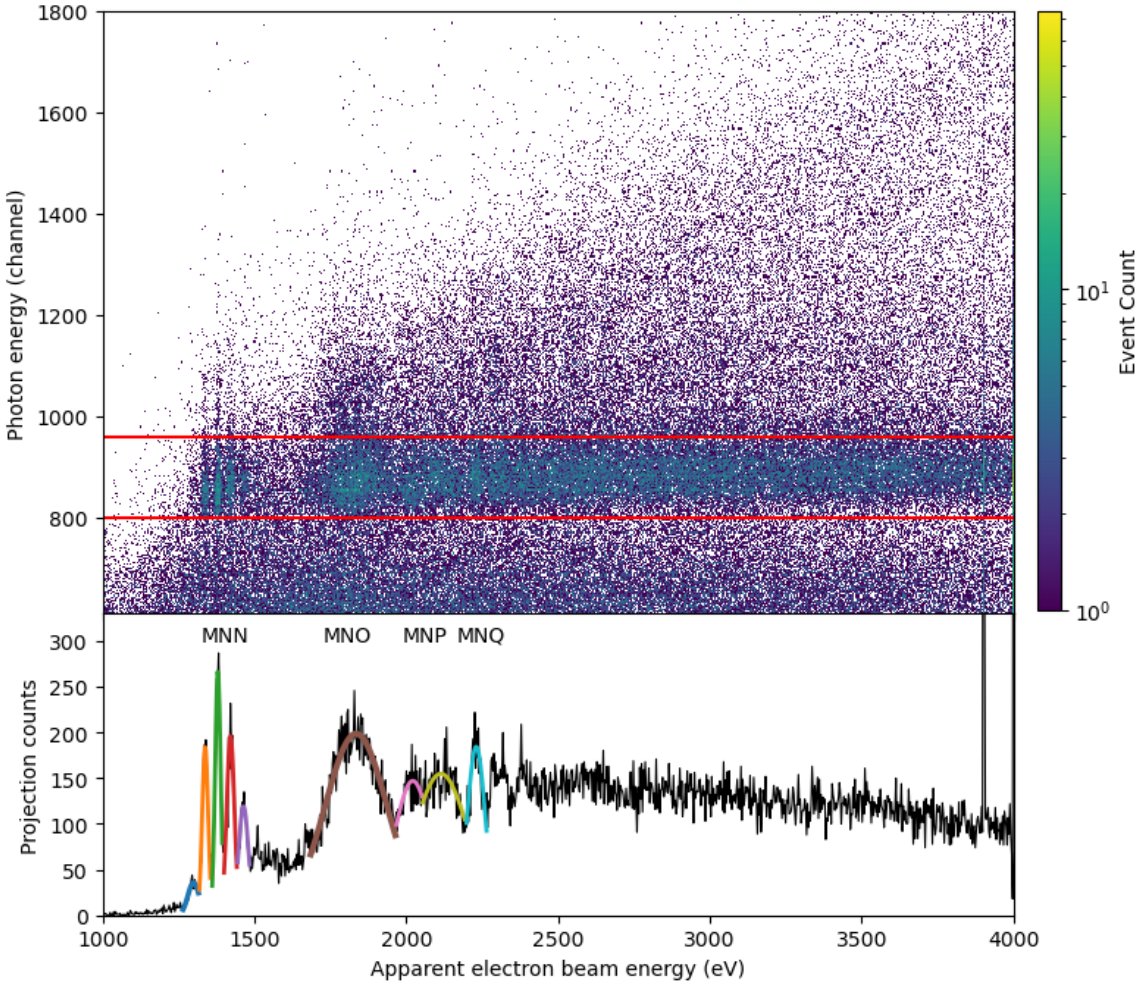

Figure 4.4: **Top:** Energy of the impacting photons, depending on the apparent energy of the electron beam, detected with the x-ray detector. The resonances of the di-electronic recombination (DR) can be seen at specific photon energies enclosed between the red lines. **Bottom:** X-projection of the counts between the red lines to determine the position of the DR resonances using a Gaussian function. The shells involved in the resonances are written above their corresponding resonances

pared to $\sigma_{\text{thin}} = 48\,\text{channel}$. Since the energy uncertainties of the electron beam are approximately constant, this implies that the broader peaks consist of several thinner peaks, which are too close together to be resolved individually. At different currents, different populations are present, which can change the shape and,

therefore, the position of the broad peak. Hence, only the MNN resonances were used to calculate the space charge.
The apparent positions of the DR resonances in each of the nine measurements can be used for a linear fit according to equation (2.23). The positions, as well as the linear fits of the MNN resonances, are shown in Figure 4.5.

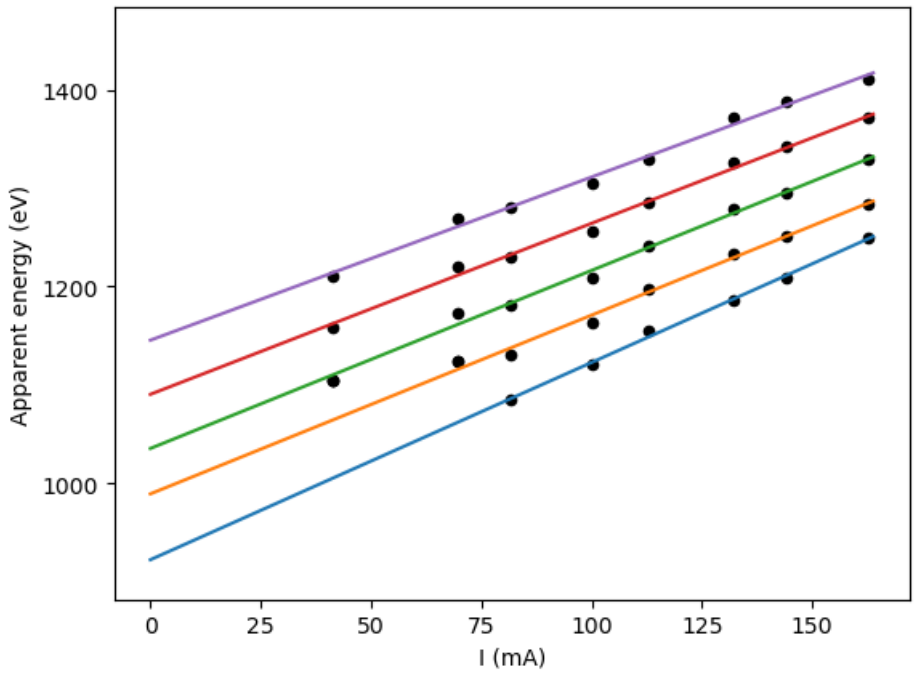

Figure 4.5: Linear fit of the apparent electron beam energies of first five resonances in the x-ray range at different currents

The resulting slope when averaging over the four upper linear fits seen in Figure (4.5) is determined as $65 \pm 3 \left[\frac{\sqrt{\text{eV}}}{\text{mA}}\right]$. The lowest fit is left out of the averaging because the resonances come from different charge states, whose populations depend on the electron beam current. Therefore, the resonance for this fit could only be found in the measurements above 75 mA. This results in a higher error proneness and was excluded from the calculation.
For the main part of the experiment the parameters used range between $I = 196.4\,\text{mA}$ with $E_{\text{kin}} = 1950\,\text{eV}$ and $I = 216.7\,\text{mA}$ with $E_{\text{kin}} = 2300\,\text{eV}$ (see Table 3.2) and therefore the space charge varies between: $\Phi_{\text{min}} = 284(8)\,\text{eV}$ and $\Phi_{\text{max}} = 288(9)\,\text{eV}$.
Similar injection pressure and dump frequency settings were used for the X-ray spectrum measurement compared to the final measurements. However, the trap depth for the X-ray measurements was 420 V (see Table 3.2) compared to 30 V for

the final measurements (see Tables 3.1, 3.3). Therefore, the space charge can be higher than expected in the main measurements because more ions can be inside the trap. However, the injection pressure was low for all measurements, which already limits the amount of ions in the trap, so the trap depth only leads to a slight change in the space charge. This will be analyzed in section 4.2.
The space charge will be subtracted from all following measurements, except for the calibration, because they were conducted at lower currents and energies, where the linear fit is not accurate anymore. This is because these measurements were conducted far away from the low settings for the calibration plots. Therefore, the errors increase substantially for this far extrapolation. In addition, the EBIT parameters differ a lot, so the compensation due to the trapped ions changes compared to high currents and energies.

4.1.4 Neon calibration

Before the actual measurements with lead, some measurements with neon were conducted to determine the correlation between the dispersive channel of the microchannel plate (MCP) or the angle of the VUV grating and the photon wavelength. Neon was chosen because it has a lot of strong lines in the EUV region, which can be seen in the second order in the VUV spectrometer as well. Oxygen was used for previous calibrations, but the amount of strong lines was insufficient for a calibration.
In order to enhance the quality of the calibration, a scan over multiple electron beam energies, which ranged from 80 eV to 300 eV in steps of 10 eV was conducted (see Table 3.3). Therefore, spectral lines of the charge states Ne^{2+} up to Ne^{8+} were visible. Using this type of scan also has the advantage of seeing when lines form or change intensity, which makes it clear to which charge state they belong. However, for the plots shown in Figures 4.6 and 4.8, the measurements were interpolated in order to show a complete energy ramp. This means that each measurement starts 5 eV before the actual value of the measurement and ends 5 eV after the actual value of the measurement, where it blends into the next measurement. Therefore, some lines do not necessarily appear where the Figures suggest.
For these discrete energy scans, a logarithmic color scale was chosen because the data spans over several orders of magnitudes and allows the visualization of both high- and low-intensity features. A logarithmic scale also highlights low-intensity lines, which are not visible with other scales.
As mentioned in section 2.10.1, the space charge was not subtracted for these measurements because it was calculated for extremely high electron beam energies compared to the neon measurements. However, because it is visible when new

lines occur in the different measurements, the space charge can be estimated to be around $\Phi \approx 10\,\mathrm{eV}$. This value was then subtracted for all measurements in this chapter.
The line positions and errors were determined using a Gaussian least-square fit, as explained in section 3.3.4. The atomic spectra database (ASD) of the National Institute for Science and Technology (NIST) was used to identify the spectral lines and their errors. For lines where there are numerous lines with short intervals, which cannot be resolved with the spectrometers used, the error was calculated to be from the center to the border of these lines.
Some spectral lines could not be identified because they possibly stem from barium, which is always emitted because the cathode comprises a barium-tungsten matrix. The amount of barium is dependent on the temperature of the cathode, but even if the temperature is low, some barium is still emitted. The lines that could be identified are seen in Tables 4.1 and 4.2 for EUV and VUV accordingly.

EUV spectrometer

The energy scan used to calibrate the EUV spectrometer can be seen in Figure 4.6. The horizontal black lines indicate the energies at which a new charge state of neon begins. They are taken from the NIST database ([37], [38], [39], [40], [41] and [42]). However, as mentioned before, the spectra are taken every 10 eV and interpolated, so some lines seem to appear at lower energies. For the lowest charge state, it is assumed that lines of Ne^{2+} as well as Ne^{3+} are present because it is not visible where each line starts.

The positions of the spectral lines were determined from the spectra of individual measurements in Figure 4.6 for different charge states. The position, fit errors, and widths of each line, as well as their according wavelength λ_{NIST} and error $\Delta\lambda_{\mathrm{NIST}}$ from the NIST database, charge state, and residuals to the resulting polynomial, are displayed in Table 4.1.

When using these lines for the calibration, it was determined via the χ^2_{red}-value that a polynomial of degree 3 is the best fit. This is shown at the top in Figure 4.7. The bottom shows the residuals for each wavelength and the errors of the residuals. These consist of the NIST database error, shown as the inner error bar in bright red, and the error of the Gaussian fit, shown as the outer error bar in dark red.
The values marked with a in Table 4.1 are not included in the fit because their error in the NIST database is substantially larger than the errors measured in this experiment. These data points would therefore falsify the result of the fit and the

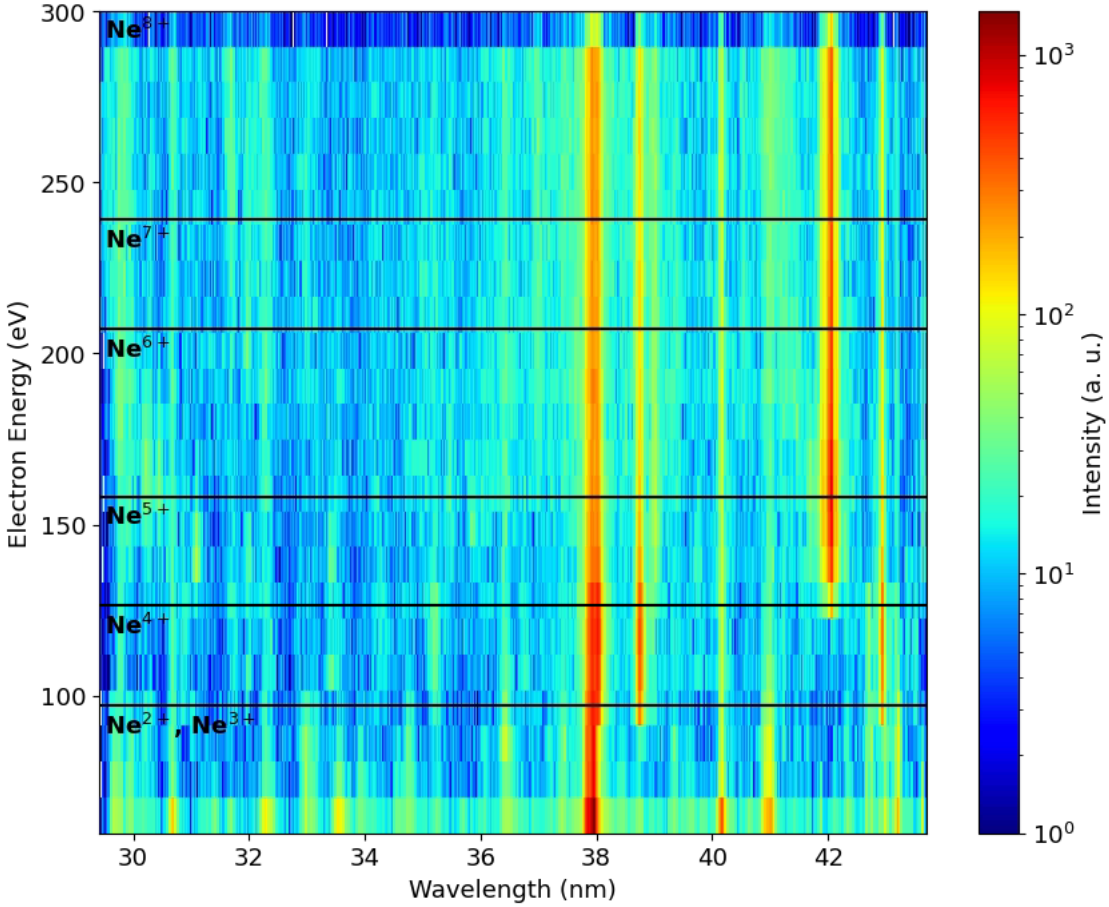

Figure 4.6: Discrete energy scan of neon used for EUV calibration to which the calibration has already been applied. The horizontal black lines indicate the ionization energies of new charge states taken from the NIST database ([37], [38], [39], [40], [41] and [42]). The corresponding charge states of neon for the ionization energies are written on the left side of the diagram

χ^2_{red}.
The resulting polynomial of degree 3 to calculate the wavelength λ is

$$\lambda(x) = \big(6.0(4) \cdot 10^{-10}\ x^3 - 3.56(13) \cdot 10^{-6}\ x^2 - 1.91(11) \cdot 10^{-3}\ x + 43.697(22)\big)\ \text{nm} \tag{4.2}$$

where x is the dispersive channel of the MCP minus 1876 divided by two. This correction has to be done due to the binning when calculating the spectrum.
For the calculation of χ^2_{red} the errors result from the error propagation of the NIST

Table 4.1: Spectral lines used for the EUV calibration with the experimentally determined dispersive channel, fit error, and width and the according wavelength λ_{NIST} and error $\Delta\lambda_{\mathrm{NIST}}$, taken from the NIST database. The * indicate values whose NIST errors are too large and are therefore not considered in the calibration

Charge State	Dispersive Channel	Width σ (channel)	λ_{NIST} (nm)	$\Delta\lambda_{\mathrm{NIST}}$ (nm)	Order	Residuals (nm)	Source
Ne III	29.7(3)	6.22	21.8131	0.005	2	0.0126	[43]
Ne III	675.3(4)	14.66	20.48	0.10*	2	0.0106	[44]
Ne III	1122.47(29)	9.15	37.93	0.0010	1	0.0126	[45]
Ne IV	190.1(6)	13.92	14.4019	0.013	3	0.0117	[43]
Ne IV	1717.5(7)	10.16	16.4795	0.011	2	0.0005	[46]
Ne V	268.8(3)	7.10	14.3219	0.007	3	0.0253	[39]
Ne V	326.6(10)	15.58	14.2441	0.008	3	0.0150	[39]
Ne V	1012.64(19)	5.94	12.9034	0.0010	3	0.0276	[39]
Ne V	1830.2(6)	7.39	15.9901	0.0021	2	0.0204	[47]
Ne VI	423.7(7)	9.56	14.095	0.010	3	0.0119	[48]
Ne VI	456.8(7)	8.10	42.17	0.10*	1	0.0289	[48]
Ne VI	476.7(5)	10.07	42.03	0.09*	1	0.0148	[48]
Ne VI	1931.5(4)	5.46	31.06	0.10*	1	0.0026	[48]
Ne VII	2029.1(4)	7.49	30.17	0.03	1	0.0160	[49]

database error, shown in Table 4.1 and the error of the Gaussian fit, as explained in section 3.3.4. The resulting $\chi^2_{\mathrm{red}} = 0.195$ is lower than the expected value of 1. This implies that the errors were overestimated.

Additionally, the resolution of the spectrometer can be determined using the spectral lines identified for the calibration. The full-width half maximum can be calculated from the line width σ with

$$\mathrm{FWHM} = 2\sigma\sqrt{2\ln(2)} \tag{4.3}$$

and the resolution can be determined with

$$R = \frac{\lambda}{\mathrm{FWHM}} \tag{4.4}$$

When taking the widths in Table 4.1 and calculating the wavelengths by inserting the channel in the calibration (see equation (4.2)), determined earlier, the resulting resolution is $R = 435(352)$. The error is the standard deviation of the resolutions for each spectral line.

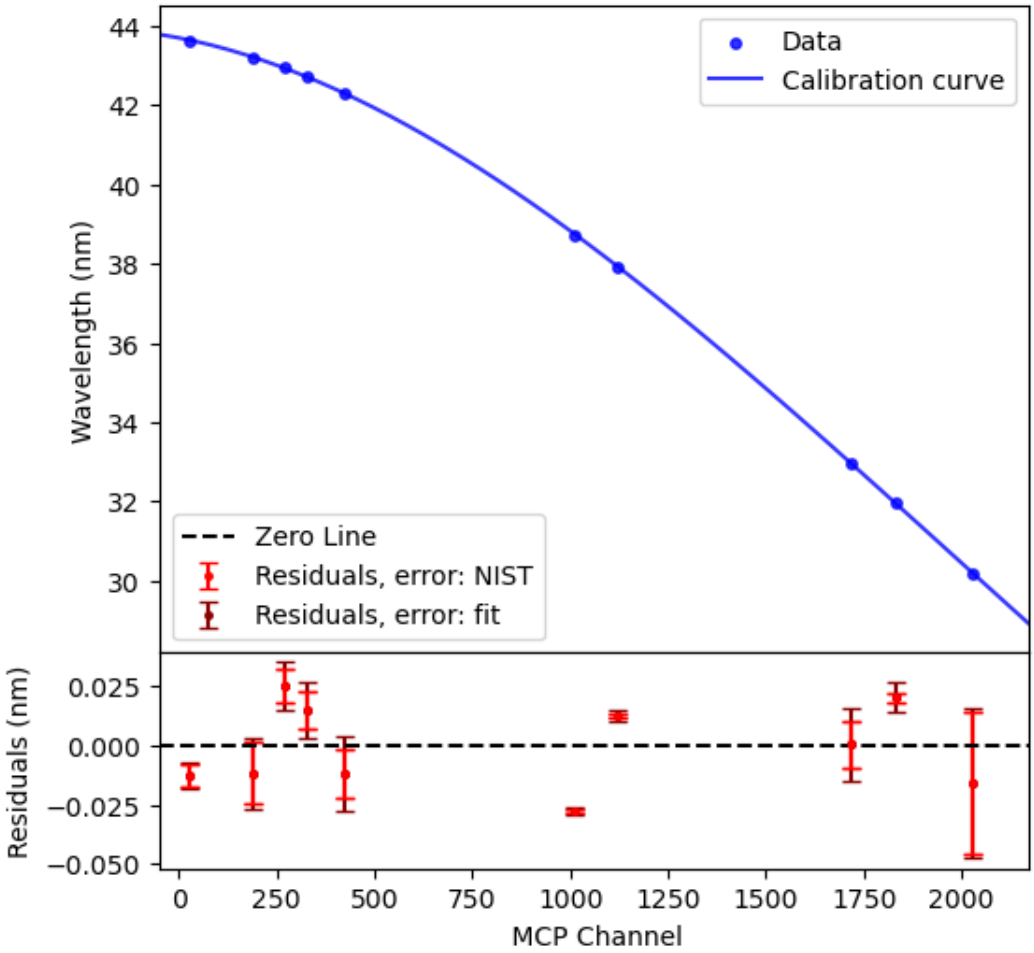

Figure 4.7: **Top:** Calibration of the EUV spectrometer using a polynomial of degree 3. The data points are the experimentally determined dispersive channel of the lines with their corresponding wavelength, taken from the NIST database. **Bottom:** Residuals of the data points in relation to the zero line of the optimal fit. The inner, light red errors are taken from the NIST database, and the outer, dark red errors are the errors of the determination of the line positions

VUV spectrometer

The energy scan used to calibrate the VUV spectrometer can be seen in Figure 4.8. The horizontal black lines indicate where a new charge state of neon begins. They are taken from the NIST database ([37], [38], [39], [40], [41] and [42]). For the lowest charge state, it is assumed that lines of Ne^{2+} as well as Ne^{3+} are present

because it is not visible where each line starts.

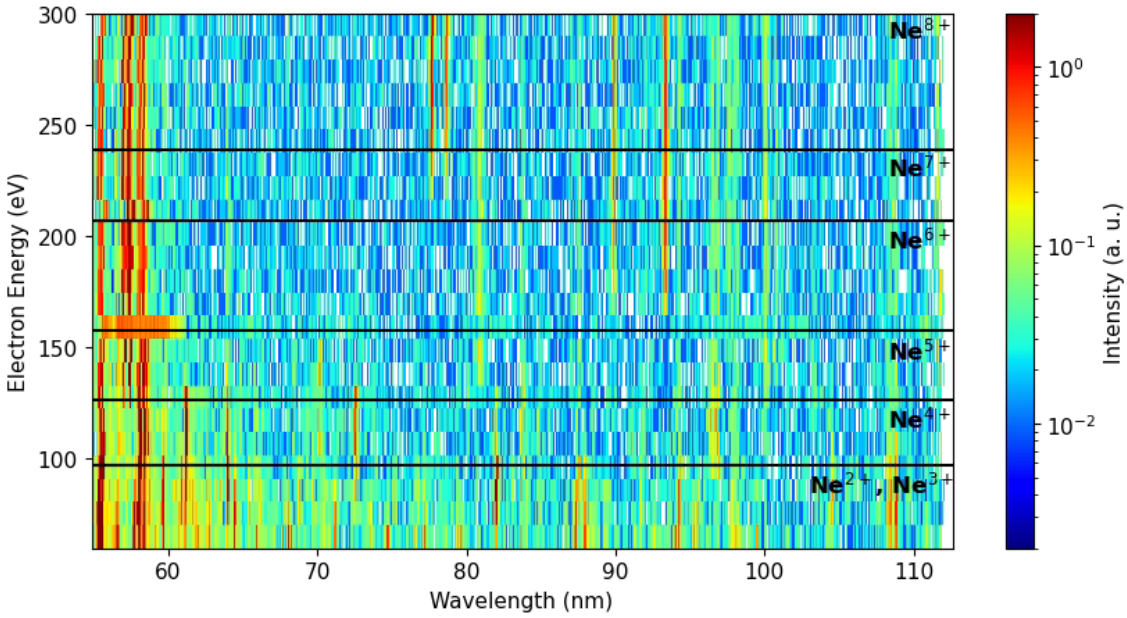

Figure 4.8: Discrete energy scan of neon used for VUV calibration to which the calibration has already been applied. The horizontal black lines indicate the ionization energies of new charge states taken from the NIST database ([37], [38], [39], [40], [41] and [42]). The corresponding charge states of neon for the ionization energies are written on the right side of the diagram

One can see that some of the spectral lines shift slightly in some of the measurements in Figure 4.8. These shifts are not constant, and whole spectra seem to be stretched or compressed compared to others. This can be analyzed by looking at the distance of the shifts and comparing it to the line width of individual measurements, as well as a static measurement.
The line width of the individual measurements of the energy scan, which lasted 50 min each is around $\sigma_{\text{short}} = 0.05\,\text{nm}$ and the line width of a static measurement, discussed in section 4.3.2, which lasted 65 h is around $\sigma_{\text{long}} = 0.3\,\text{nm}$. The largest shift seen in Figure 4.8 at about 1212° between the measurements at 210 eV and 220 eV is 0.35 nm. This suggests that stretching and compressing are happening during the measurements.
These shifts in angle cause problems when calibrating the detector. The calibration was done using measurements that showed the least shifts to other measurements and, therefore, the least deviation to spectral lines visible in multiple measure-

ments. However, it is still possible that these lines are stretched or compressed compared to the energy scan with lead, and the calibration is only reliable to the largest shift of $\lambda_{\text{shift}} = 0.35\,\text{nm}$.
After identifying the measurements with the least stretching or compressing, the line positions and widths were determined using a least-square Gaussian fit, as explained in section 3.3.4. The position, fit-error, and width of lines used for this calibration, as well as their according wavelength λ_{NIST} and error $\Delta\lambda_{\text{NIST}}$ from the NIST database, charge state, and residuals to the resulting polynomial, are displayed in Table 4.2.

Table 4.2: Spectral lines used for the VUV calibration with the experimentally determined angle, fit error, and width the according wavelength λ_{NIST} and error $\Delta\lambda_{\text{NIST}}$, taken from the NIST database. The * indicate values whose NIST errors are too large and are therefore not considered in the calibration

Charge State	Angle (°)	Width σ (°)	λ_{NIST} (nm)	$\Delta\lambda_{\text{NIST}}$ (nm)	Order	Residuals (nm)	Source
Ne III	−14.317 40(17)	0.00378	21.8131	0.005	4	0.0038	[43]
Ne III	−13.937 30(13)	0.00311	20.48	0.10*	4	0.0104	[44]
Ne IV	−15.852 80(16)	0.00441	54.3891	0.0006	2	0.0372	[44]
Ne IV	−14.7961(4)	0.00325	46.9872	0.006	2	0.0205	[44]
Ne IV	−12.791 80(15)	0.00305	16.4795	0.011	4	0.0189	[46]
Ne III	−12.1238(4)	0.00550	28.2495	0.0010	2	0.0466	[45]
Ne V	−12.652 10(8)	0.00290	15.9901	0.0021	4	0.0219	[47]
Ne VI	−16.058 90(22)	0.00289	55.8600	0.0005	2	0.0144	[40]
Ne VI	−15.2323(3)	0.00470	50.05	0.10*	2	0.0129	[48]
Ne VI	−12.181 60(3)	0.00280	14.352	0.006	4	0.0535	[40]
Ne VI	−15.4600(9)	0.00529	103.35	0.10*	1	0.0435	[48]
Ne VII	−14.5025(4)	0.00468	44.95	0.004	2	0.0228	[49]

The values marked with * in Table 4.1 are not included in the fit because their error in the NIST database is substantially larger than the errors measured in this experiment. These data points would, therefore, falsify the result of the fit and the χ^2_{red}.
The χ^2_{red}-value is used to determine whether a polynomial of degree 2 or 3 is a better fit. For the parabola, the χ^2_{red}-value was closer to 1 and is therefore used as a fitting function, which is shown at the top in Figure 4.9. The bottom shows the residuals for each wavelength and the errors of the residuals. These consist of the NIST database error, shown as the inner error bar in bright red, and the error of

the Gaussian fit, shown as the outer error bar in dark red.

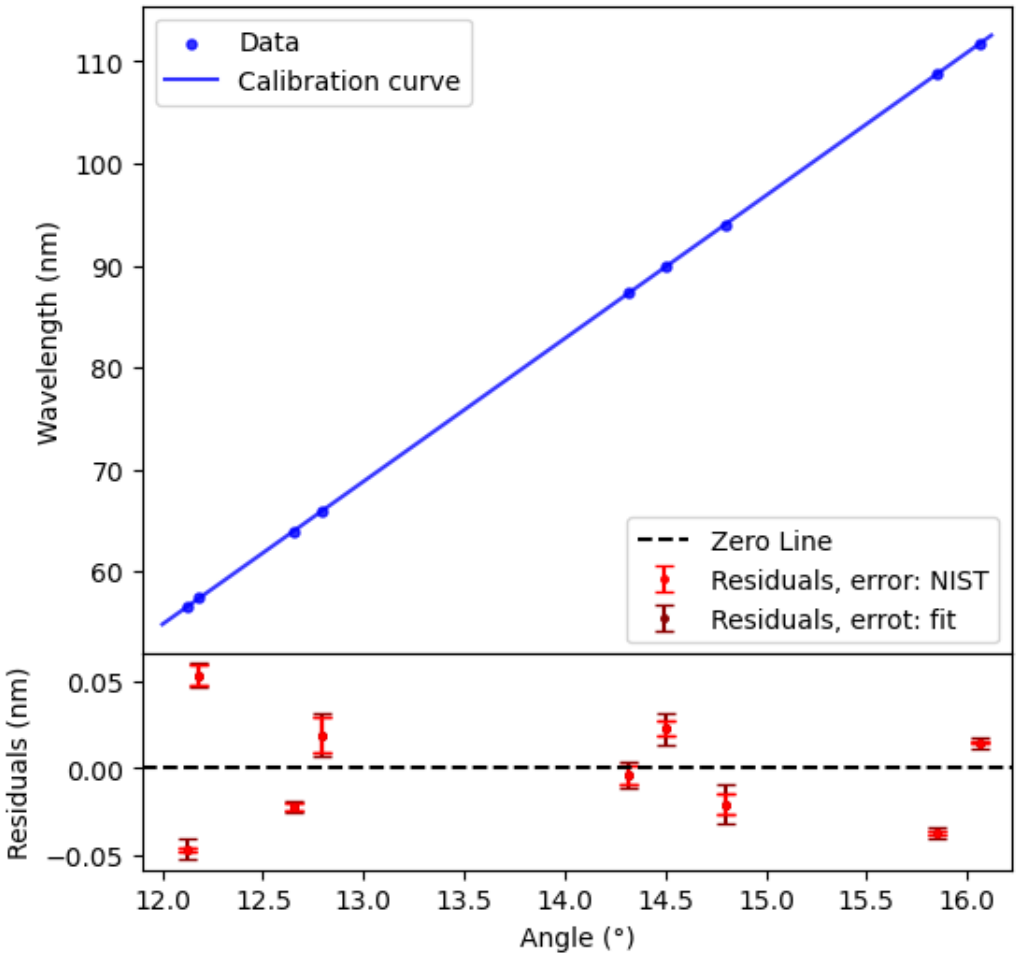

Figure 4.9: **Top:** Calibration of the VUV spectrometer using a polynomial of degree 2. The data points are the experimentally determined angles of the lines with their corresponding wavelength, taken from the NIST database. **Bottom:** Residuals of the data points in relation to the zero line of the optimal fit. The inner, light red errors are taken from the NIST database, and the outer, dark red errors are the errors of the determination of the line positions

The resulting parabola for the calibration is

$$\lambda(\theta) = \left(1.9(8) \cdot 10^{-3}\ \theta^2 - 13.96(23)\ \theta - 113.0(16)\right)\ \text{nm} \tag{4.5}$$

where θ is the angle of the VUV grating.
For the calculation of χ^2_{red} the errors result from the error propagation of the NIST

database error, shown in Table 4.1 and the error of the Gaussian fit, as explained in section 3.3.4. The resulting $\chi^2_{\text{red}} = 0.366$ is lower than the expected value of 1. This implies that the errors were overestimated.
Additionally, the resolution of the spectrometer can be determined using the spectral lines identified for the calibration. The full-width half maximum can be calculated from the line width σ with equation (4.3), and the resolution can be determined with equation 4.4.
When taking the widths in Table 4.2 and calculating the wavelengths by inserting the angle in the calibration (see equation (4.5)), determined earlier, the resulting resolution is $R = 709(221)$. The error is the standard deviation of the resolutions for each spectral line.

4.2 EUV measurements

After the preparatory measurements, lead was injected into the EBIT for the central part of the experiment. The EUV spectrometer can resolve the spectral lines of interest in the first order. Firstly, an energy scan was made to determine which lines belong to which charge state and specifically which are of Pb^{41+}. After that, a longer measurement was conducted at a fixed energy, where the spectrum of Pb^{41+} was expected. Both are compared to the theoretical spectra calculated with FAC and AMBiT, as explained in section 2.8.

4.2.1 Discrete electron energy scan

The discrete energy scan of lead with the settings of Table 3.3 is displayed in Figure 4.10.

After subtracting the space charge determined in section 4.1.3, the visible charge states of lead are Pb^{36+} to Pb^{42+}. Even though the space charge was determined with a deeper trap, and these measurements were conducted with a shallow trap, the space charge is suitable for this energy scan. This can be seen because the spectral lines appear close to the horizontal black lines, which indicate the ionization energy of a new charge state, taken from the NIST database [50], [51]. Especially the strong lines at around 37 nm appear at the new charge states Pb^{39+} and Pb^{41+}.
Therefore, it can be assumed that the space charge, determined in section 4.1.3, is valid for the measurements with lead even though the trap was deeper during the

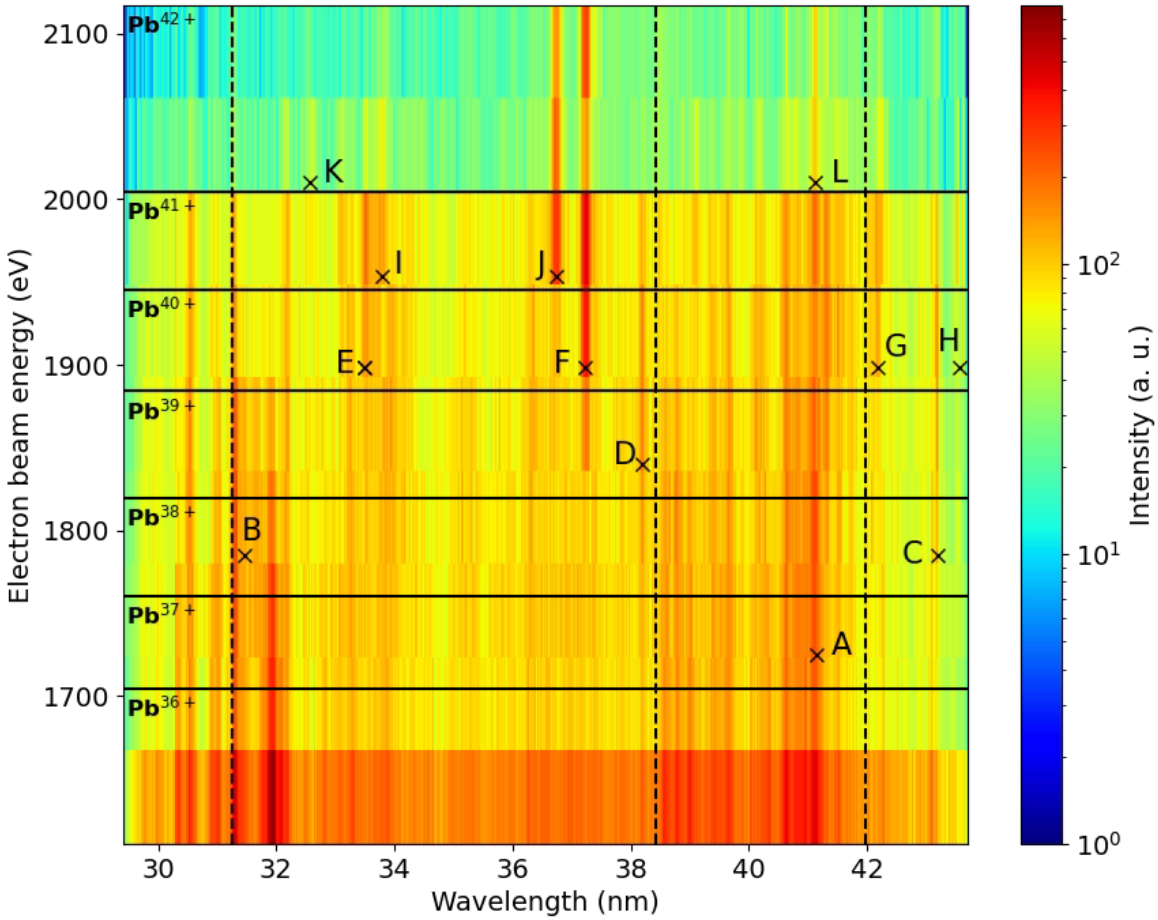

Figure 4.10: Discrete energy scan of lead, detected with the EUV spectrometer and corrected for space charge. The horizontal black lines indicate the ionization energies, taken from the NIST database [50], [51]. The corresponding charge states Pb^{36+} to Pb^{42+} are labeled on the right side of the diagram. The dashed vertical lines indicate theoretical positions of strong carbon lines [52]. The letters A-L mark spectral lines that appear or increase in intensity in this charge state

space charge determination. This can be explained by the low injection pressure, which limits the amount of trapped ions and, therefore, the compensation of the space charge by the positive ions, which would normally be dependent on the trap depth.
In Figure 4.10, one can also see that the count rate is higher in the first measurement than in the following measurements. Usually, it is expected to be the

opposite way because the measurements at higher energies also have higher currents, which increases the count rate. A possible explanation for this is that a lot of lead was injected initially but decreased over time. This could also explain the decreasing count rates for the two measurements at the highest energy.
In addition to lead, some carbon is also detected in this energy scan because tetraethyl lead $(C_2H_5)_4Pb$ is injected, which contains carbon. Hydrogen cannot be seen in this scan because it has no transitions in the wavelength range of the EUV detector. The vertical dashed lines in Figure 4.6 are at wavelengths where carbon has transitions with high intensities. These lines can be seen even though the ionization energy is four or five times lower than the energies of this energy scan. The values are taken from the NIST database [52]. The charge state, with Ritz wavelength λ_{NIST} and error $\Delta\lambda_{\mathrm{NIST}}$, spontaneous emission coefficient A_{ki} and the initial and final energy states E_i and E_k are shown in Table 4.3. These wavelengths can be seen in the first order with the EUV spectrometer.

Table 4.3: Strong transitions of carbon with wavelength λ_{NIST}, error $\Delta\lambda_{\mathrm{NIST}}$, spontaneous emission coefficient A_{ki}, and energies E_i and E_k of the involved charge states, taken from the NIST database [52]

Charge State	λ_{NIST} (nm)	$\Delta\lambda_{\mathrm{NIST}}$ (nm)	A_{ki} (s^{-1})	E_i (eV)	E_k (eV)
C IV	31.2420	0.0040	$4.63 \cdot 10^9$	0.0000	39.6851
C IV	38.4174	0.0010	$1.75 \cdot 10^{10}$	8.0084	40.2813
C IV	41.9714	0.0010	$2.85 \cdot 10^9$	8.0084	37.5485

The carbon line at 31.2420 nm aligns with an experimental line, which is visible throughout most of the charge states. This indicates, that this spectral line is part of carbon instead of lead. The carbon line at 38.4174 nm is also very close to a spectral line, which is visible in several charge states. The last carbon line at 41.9714 nm is not visible in the EUV spectrometer, but possibly in the VUV spectrometer, and is analyzed in section 4.3.1.
The letters A-L in Figure 4.10 mark spectral lines that appear or become more intense at new charge states. They will be discussed in more detail later in this section. Some of these weak lines are made visible due to the logarithmic scale applied to the diagram.

In addition to the experimental energy scan, two theoretical calculations of the charge states Pb^{36+} to Pb^{42+} were made with FAC and AMBiT, as explained in section 2.8. For each calculation, one column displays the transition energy, and another displays the spontaneous emission coefficient A_{ki}. For each data point, a Gaussian is calculated according to equation (3.2) with the transition energy as

the mean value and A_{ki} as the amplitude. For the width, a value of $\sigma = 0.135\,\text{nm}$ was chosen, which is approximately the width of spectral lines in Figure 4.10.
For each calculation, the charge states are plotted in the same manner as Figure 4.6. As the calculations with FAC and AMBiT have different outcomes, both are shown for several charge states in Figure 4.11. They are structured like a discrete energy scan for better comparison. The spectral lines of different charge states can sometimes appear earlier than the ionization energy of this charge state and be visible even after a new charge state begins. Therefore, for the theoretical calculations, the spectrum of each charge state is also made visible in the charge state before and after, but with a lower intensity. This is implemented using a Gaussian (equation (3.2)) weighting with $\sigma = 1$.
For the theoretical energy scans in Figure 4.11, a square root scale was chosen. This was done because a few high-intensity values are dominating the visualization. The square root scale mitigates the impact of extreme values, making the visualization more balanced compared to a logarithmic scale.
In Figure 4.11, the strong carbon lines, listed in Table 4.3 are also displayed as continuous lines, visible at every energy.

When comparing the results from the theoretical calculations to the experimental energy scan in Figure 4.10, not many similarities can be seen. Therefore, the spectra of the individual charge states were analyzed. This was done by comparing both theoretical calculations to a spectrum taken at the energy of the charge state of interest, as well as the difference to the spectrum at the energy of the previous charge state. When only considering the positive part of this difference, one can see which spectral lines are part of the new charge state and which were already visible in the previous one.
This comparison was done for the Pb^{37+} to Pb^{42+} as shown in Figures 4.12 and 4.13. For Pb^{36+} and Pb^{37+}, the AMBiT calculation did not yield any spectral lines in the EUV wavelength, and since there is no measurement for Pb^{35+}, the difference between charge states cannot be calculated for Pb^{36+}. Therefore, no comparison was done for Pb^{36+}.

In Figures 4.12 and 4.13, the spectral lines with a large difference to the previous charge state were identified and marked with the letters A-L. The corresponding positions of these lines are marked with the same letters in Figure 4.10. Additionally, vertical lines at the position of these lines can help identify the charge states, where they appeared first, and if they increase in intensity in the following charge states.
After identifying the most relevant spectral lines, they are compared to the theory. Since it is difficult to determine the ground state energy during FAC calculations precisely, the spectra may be shifted or even stretched or compressed. To sim-

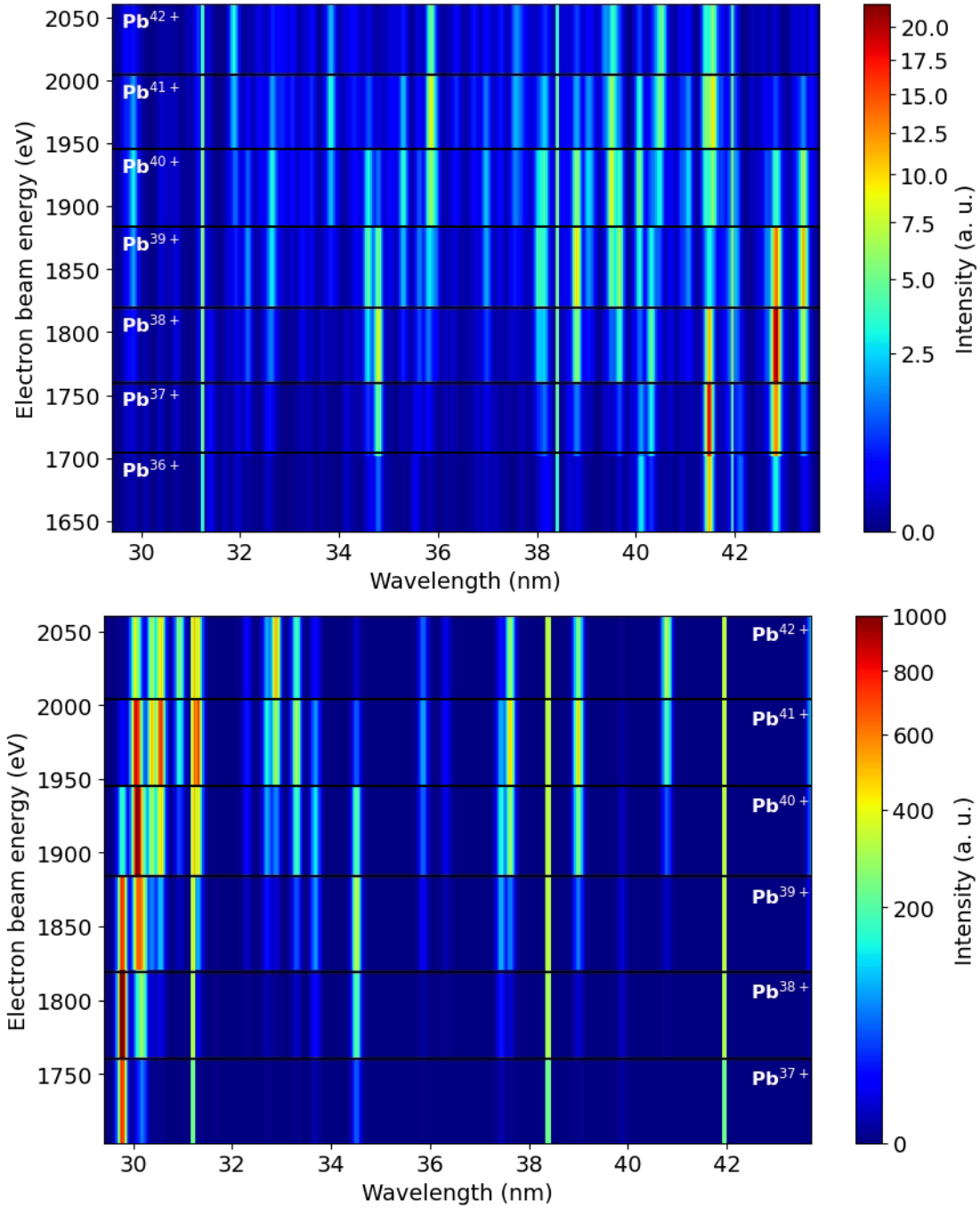

Figure 4.11: Theoretical calculations of different charge states for the EUV wavelength range **top:** with FAC for Pb^{36+} to Pb^{42+} and **bottom:** with AMBiT for Pb^{37+} to Pb^{42+}. The horizontal black lines indicate the ionization energies, taken from the NIST database [50], [51]. The corresponding charge states are labeled on the right and left sides of the diagram. In addition, the strongest spectral lines of carbon are displayed as continuous spectral lines in every charge state

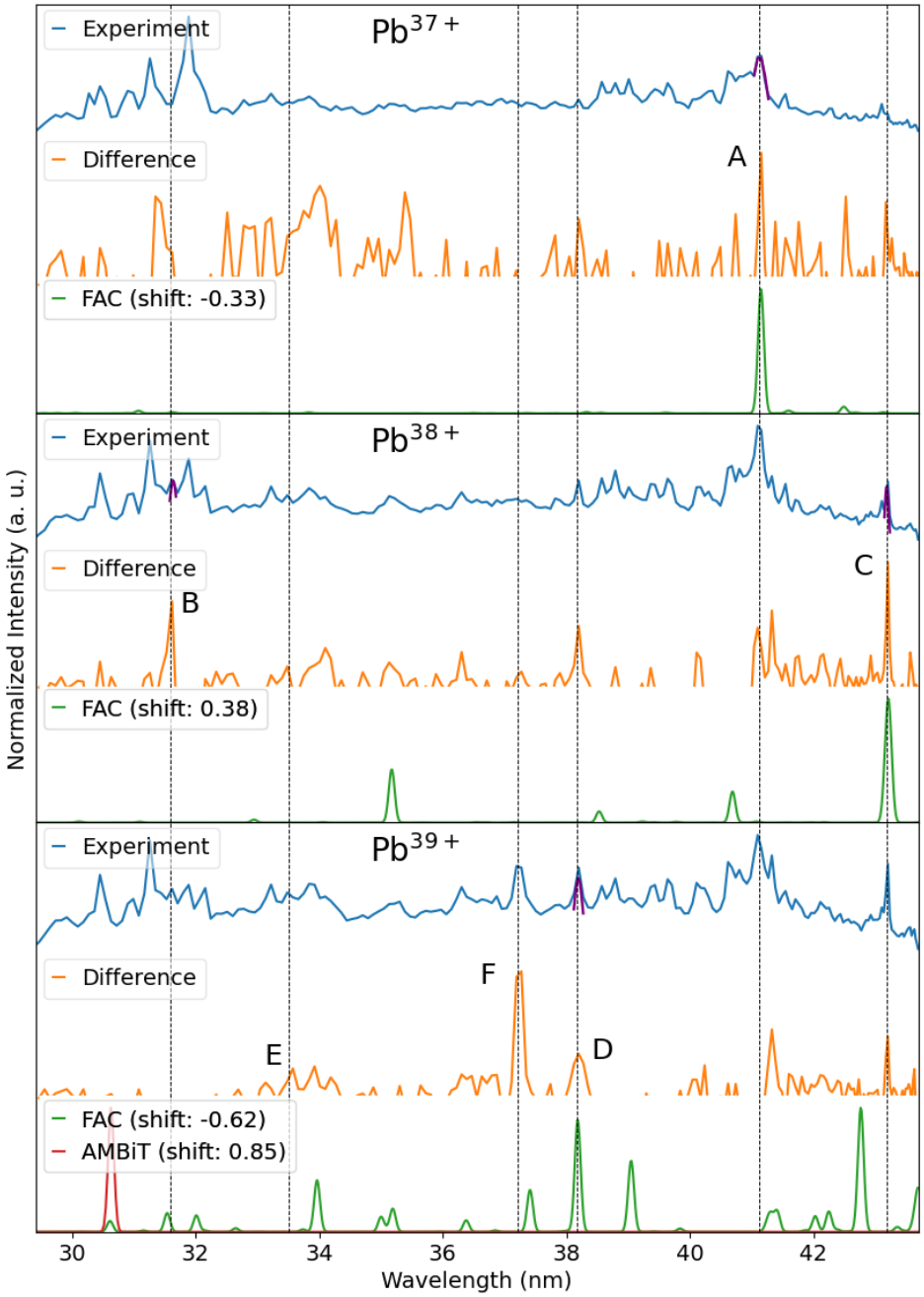

Figure 4.12: Comparison of the individual spectra of the discrete energy scan of the EUV spectrometer and the difference between these and the spectra of the previous charge state to the theoretical calculations with FAC and AMBiT for Pb^{37+} to Pb^{39+}. The letters A-F mark the spectral lines that appear or increase in intensity. Their positions are determined using a least-square Gaussian fit, displayed in purple, and vertical dashed lines are inserted to compare their positions to other charge states. The theoretical spectra are shifted to align with the experimental spectra, and the shift of each theory is displayed in the according legend

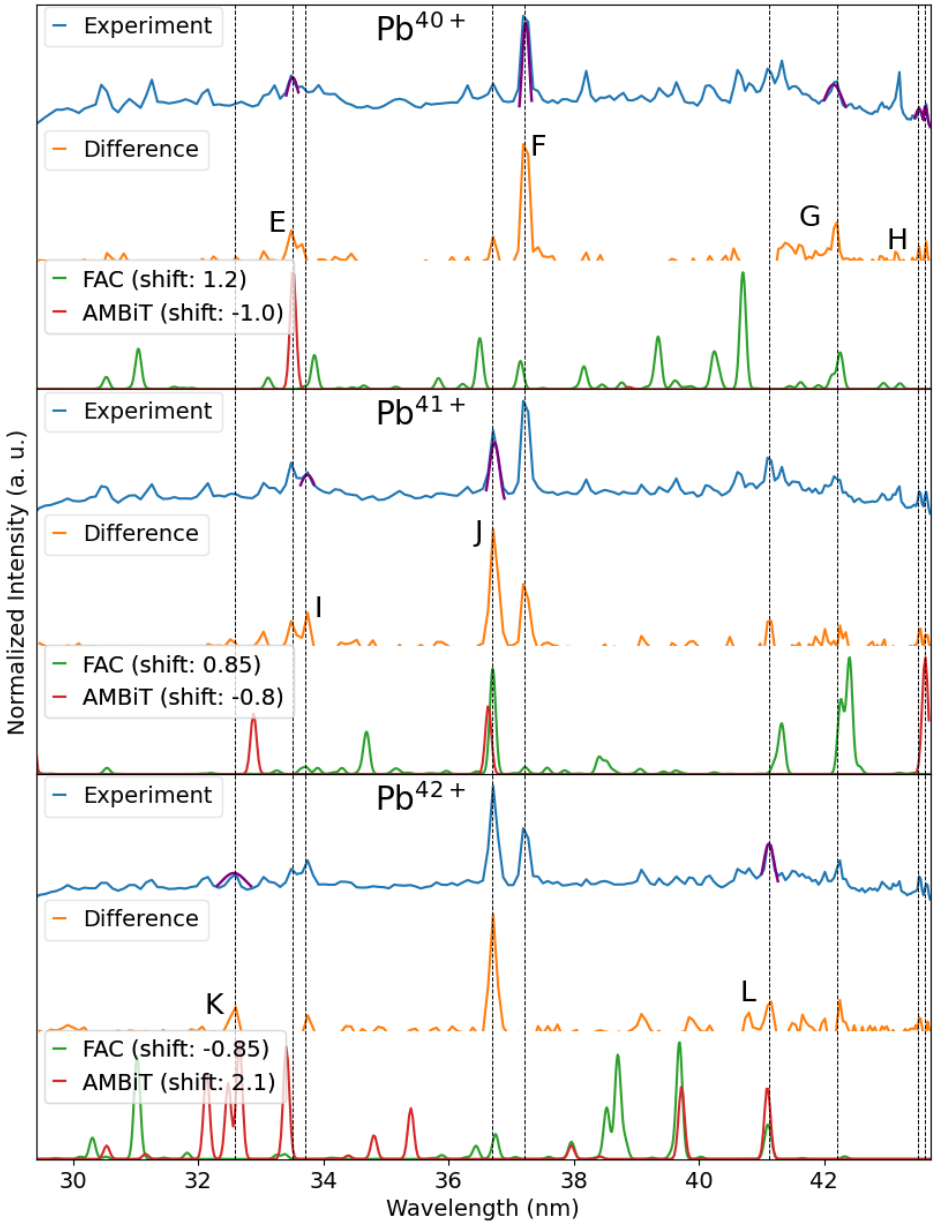

Figure 4.13: Comparison of the individual spectra of the discrete energy scan of the EUV spectrometer and the difference between these and the spectra of the previous charge state to the theoretical calculations with FAC and AMBiT for Pb^{40+} to Pb^{42+}. The letters E-L mark the spectral lines that appear or increase in intensity. Their positions are determined using a least-square Gaussian fit, displayed in purple, and vertical dashed lines are inserted to compare their positions to other charge states. The theoretical spectra are shifted to align with the experimental spectra, and the shift of each theory is displayed in the according legend

plify matters, the FAC spectra were only shifted to best fit the difference between measurements. The amount of the shift in nm is shown in the legend. The same procedure is applied to the AMBiT calculations.
All spectra are normalized to the strongest line in each spectrum for a better comparison.

The spectral lines A-L can now be analyzed and assigned to a possible charge state.

A: This spectral line can be seen at 41.128(8) nm in Pb^{37+} and has the most intense difference to the previous energy step. The strongest corresponding theoretical line was shifted to the position of this spectral line. When shifting the theory like this, a few weak lines can also be identified in the difference to Pb^{36+}. In the following charge state of Pb^{38+}, the line intensity of this line increases. This can be explained by the cross-section in equation (2.8), which states that the intensities of spectral lines can increase even after the ionization energy of a new charge state is reached. In the difference between the measurements of Pb^{39+} and Pb^{38+}, the spectral line vanishes, but it can still be seen in the spectrum, which supports the theory that it is part of Pb^{37+}.
Other lines in the spectrum of Pb^{37+} are not analyzed because in the difference to the previous energy step, a lot of lines are visible, and it is possible that some of these stem from the noise due to higher count rates in the measurement of Pb^{36+}.

B: In Pb^{38+}, the two strongest lines in the difference to Pb^{37+} are analyzed. Line **B** already seems to gradually appear in Pb^{37+} at 31.632(5) nm due to the small peak embedded into the larger one next to it. However, it is not yet visible in the spectrum. In Pb^{38+}, the intensity increases significantly, and in the spectrum of Pb^{39+}, it is visible but does not increase in intensity. This can imply that it is part of Pb^{38+}. However, the line is not found in the theoretical calculations for Pb^{38+}. Instead, a weak line can be seen in the theoretical calculation of Pb^{37+}, and it is, therefore, assumed that this line belongs to Pb^{38+}.

C: The strongest line in the difference between Pb^{38+} and Pb^{37+} is spectral line **C** at 43.1883(17) nm. It is already visible in the difference between Pb^{37+} and the previous energy step, but only as a weak line in the spectrum. In Pb^{38+} and Pb^{39+}, this line continues to increase, but the less strongly. The line of this position is not marked in Pb^{40+}, but it can be seen that it does not increase further. Therefore, spectral line **C** can be assumed to be part of

Pb^{38+} or Pb^{39+}. When shifting the FAC spectrum of Pb^{38+} accordingly, the second strongest line in the theoretical spectra seems to line up with another line that increases in intensity.

D: Another striking line in the difference of Pb^{39+} and Pb^{38+} is spectral line **D** at 38.195(3) nm because it is broader compared to other lines. It can already be seen in the differences between Pb^{37+} and Pb^{38+} and their previous energy steps, but it is narrower there. This line may be part of either Pb^{38+} or Pb^{39+} because it is not visible in the difference of later charge states. Both have theoretical lines FAC, which could be the corresponding spectral line. However, when shifting the theory for Pb^{39+}, some other lines, including the possible line on the right of the spectral line **F**, are fitting. The AMBiT spectrum is not close to any strong lines in the difference of Pb^{39+} and Pb^{38+} and was therefore shifted to be more fitting to the FAC theory.

E: This spectral line has been visible at 33.508(4) nm in the difference of every charge state and also remains visible until Pb^{41+}. However, it was difficult to distinguish it from the noise until Pb^{40+}, and no theoretical lines were present close to line **E**. Therefore, it can be assumed to be part of Pb^{40+}. When shifting the FAC spectrum so that a theoretical line is close to this spectral line, some theoretical lines are also close to the lines **F** and **G**. There is only one strong line in the AMBiT spectrum, which was also shifted to be at the same position as this spectral line.

F: This spectral line can first be seen in Pb^{39+} at 37.2338(14) nm and is the strongest line in the difference to Pb^{38+}. However, it increases even further in Pb^{40+} and Pb^{41+}. Therefore, this line is assumed to be part of Pb^{40+}, and the FAC spectrum is shifted accordingly. When doing so, some other spectral lines seem to align as well. These include spectral line **G**, which supports this assumption. In Pb^{39+}, it also seems like the base of the line **F** is wider on the right side. This could be another weaker line, which already appears slightly in Pb^{38+}. When shifting the FAC spectrum from Pb^{39+} to be fitting for spectral line **D**, a weaker line can be found at this position in the theoretical spectrum.

G: Another interesting line in the spectrum of Pb^{40+} is spectral line **G** at 42.152(4) nm due to its shape with the broader base on the left side of the line. It is also visible in the spectra of previous charge states but only as a weak spectral line without the distinctive shape. This shape can also be found in the FAC theory, and when shifting it, other spectral lines align as well or are close to lines such as the lines **F** and **E**.

H: Spectral lines in the area of the two lines of **H** at 43.5192(19) nm and 43.6225(16) nm can be seen in previous charge states. However, they disappear or are located at a different position until the two lines become visible in the spectrum and the difference of Pb^{40+} and Pb^{39+}. However, the theoretical values of FAC and AMBiT do not predict close spectral lines in this charge state. In Pb^{41+}, one of the two lines can be found in the AMBiT spectrum, so at least one of the two lines is assumed to be of Pb^{41+}. Another indicator for this is that the line **J** also aligns with the theoretical spectrum when shifting it like this. The other one does not have a theoretical prediction but is still noteworthy because it does not belong to previous charge states.

I: This spectral line appears in Pb^{40+} at 33.745(6) nm and becomes stronger in Pb^{41+} and Pb^{42+}. It is assumed to be part of Pb^{41+} because the difference to the previous energy step is strongest. However, aligning the FAC theory to this line is difficult because there are a few weak lines in that area. Therefore, the spectrum is shifted according to line **J**, and the theoretical position of line **I** can be determined.

J: The strongest line for the difference of Pb^{41+} and Pb^{42+} to their previous energy step is line **J**. It appears as a weak line at 36.7340(22) nm in Pb^{39+} and becomes stronger until reaching a maximum difference to the previous charge state in Pb^{41+}. Therefore, it can be assumed to be part of this charge state, and compared to the theoretical spectra, both have lines at this position. When aligning the theory like this, there are also theoretical FAC lines close to line **I** and theoretical AMBiT lines close to one of the spectral lines **H**.

K: This spectral line at 32.568(11) nm is the second strongest one in the difference of Pb^{42+} and Pb^{41+} that does not belong to a previous charge state. This line already appears in the difference of Pb^{41+} and Pb^{40+}, but is very weak there. This line may increase even more in Pb^{43+}, but since it can be found in the theoretical AMBiT spectrum when aligning it to fit to line **L**, one can assume it belongs to Pb^{42+}. Two strong lines are close to it, so both are determined.

L: In the spectrum of Pb^{42}, the strongest line of the difference to Pb^{41+} was line **J** and identified as part of Pb^{41+}. Most of the remaining lines are assumed to be noise. Therefore, the theoretical spectra were shifted to align with line **L** at 41.124(4) nm. This line is at the same position as line **A**. Therefore, it may be the same line as analyzed earlier. However, it becomes weaker in Pb^{39+} and Pb^{40+} before getting stronger again, which can imply that it is a new line at the same position. Both theoretical spectra have a line close

to line **L**, so they are shifted to align. The AMBiT spectrum then also aligns with line **L**; therefore, it can be assumed that both lines belong to Pb^{42+}.

The results of this analysis are summarized in Table 4.4 for the comparison with the FAC calculations and in Table 4.5 for the comparison with the AMBiT calculations. These include the experimental position λ_{exp} and intensity I_{exp} with error, determined from the individual measurement to which the line is assumed to belong. The error of the intensity is the square root of the intensity. This is because Poisson statistics can be applied to model the uncertainty associated with counting events, such as photons. The standard deviation in Poisson statistics is given by the square root of the count.
The experimental values are compared to the theoretical wavelength λ_{FAC} or λ_{AMBiT}, spontaneous emission coefficient A_{ki}, and the quantum number J_k and J_i of the involved states.

Table 4.4: Positions λ_{exp} and intensities I_{exp} of identified experimental lines in the EUV spectrum compared to their theoretical wavelengths λ_{FAC}, transition rates weighted with the upper-state population, and the twice the quantum numbers J_k and J_i of the involved states, calculated with FAC

Line	Charge State	λ_{exp} (nm)	I_{exp} Counts	λ_{FAC} (nm)	Intensity (a. u.)	$2J_k$	$2J_i$
A	Pb^{37+}	41.128(8)	2200(47)	41.482	6.179	3	5
B	Pb^{37+}	31.632(5)	1344(37)	31.955	0.058	13	13
C	Pb^{38+}	43.1883(17)	1228(35)	42.8058	3.348	4	4
	Pb^{38+}	43.1883(17)	1228(35)	42.8537	4.449	6	8
D	Pb^{39+}	38.195(3)	1330(36)	38.805	3.405	9	9
E	Pb^{40+}	33.508(4)	1079(33)	-	-	-	-
F	Pb^{40+}	37.2338(14)	2736(52)	35.9512	0.657	6	6
G	Pb^{40+}	42.153(4)	904(30)	41.062	0.888	4	6
H	Pb^{40+}	43.5192(19)	433(21)	-	-	-	-
	Pb^{40+}	43.6225(16)	512(23)	-	-	-	-
I	Pb^{41+}	33.745(6)	1098(33)	32.880	0.175	7	9
J	Pb^{41+}	36.7340(22)	2121(46)	35.8564	2.993	5	5
K	Pb^{42+}	32.568(11)	345(19)	-	-	-	-
L	Pb^{42+}	41.124(4)	824(29)	41.933	0.204	10	8
	Pb^{42+}	41.124(4)	824(29)	41.979	0.211	4	0

In Table 4.4 the theoretical line for line **L** has a transition with $J_k = 2$ and $J_i = 0$. This means it is a $\Delta J = 2$-transition and, therefore, probably an E2 transition. These are also electric diploe transitions, line E1, but are weaker due

to the selection rule $\Delta J = 2$. However, compared to other theoretical lines, it is not significantly weaker, and therefore, it may still be visible in the spectrum.

Table 4.5: Positions λ_{exp} and intensities I_{exp} of identified experimental lines in the EUV spectrum compared to their theoretical wavelengths λ_{AMBiT}, spontaneous emission coefficient A_{ki}, and the twice the quantum numbers J_k and J_i of the involved states, calculated with AMBiT

Line	Charge State	λ_{exp} (nm)	I_{exp} Counts	λ_{AMBiT} (nm)	A_{ki} (s^{-1})	$2J_k$	$2J_i$
A	Pb^{37+}	41.128(8)	2200(47)	-	-	-	-
B	Pb^{37+}	31.632(5)	1344(37)	-	-	-	-
C	Pb^{38+}	43.1883(17)	1228(35)	-	-	-	-
D	Pb^{39+}	38.195(3)	1330(36)	-	-	-	-
E	Pb^{40+}	33.508(4)	1079(33)	34.514	116.56350712567105	9	7
F	Pb^{40+}	37.2338(14)	2736(52)	-	-	-	-
G	Pb^{40+}	42.153(4)	904(30)	-	-	-	-
H	Pb^{40+}	43.5192(19)	433(21)	-	-	-	-
	Pb^{40+}	43.6225(16)	512(23)	44.4194	87.35379439595206	4	6
I	Pb^{41+}	33.745(6)	1098(33)	-	-	-	-
J	Pb^{41+}	36.7340(22)	2121(46)	37.4357	51.230588752036475	6	8
K	Pb^{42+}	32.568(11)	345(19)	30.377	164.85353191034704	9	7
K	Pb^{42+}	32.568(11)	345(19)	30.556	257.55740894400725	5	3
L	Pb^{42+}	41.124(4)	824(29)	38.998	158.51807039444208	9	7

4.2.2 Static measurement

In addition to the discrete energy scan, a static measurement was conducted at the energy, where the charge state Pb^{41+} was expected, but for a significantly longer duration than each measurement in the discrete energy scan. Therefore, the lines should be better defined, and lines with low intensities are distinguishable from the noise.
The static spectrum is displayed on a section of the discrete energy scan in Figure 4.14 for a better comparison. With this scan, one can now distinguish the weak lines from the noise and determine line positions more accurately.

The theoretical transitions of interest are the three stated in section 2.6. The spontaneous emission coefficient A_{ki} of each line can help to identify the experimental

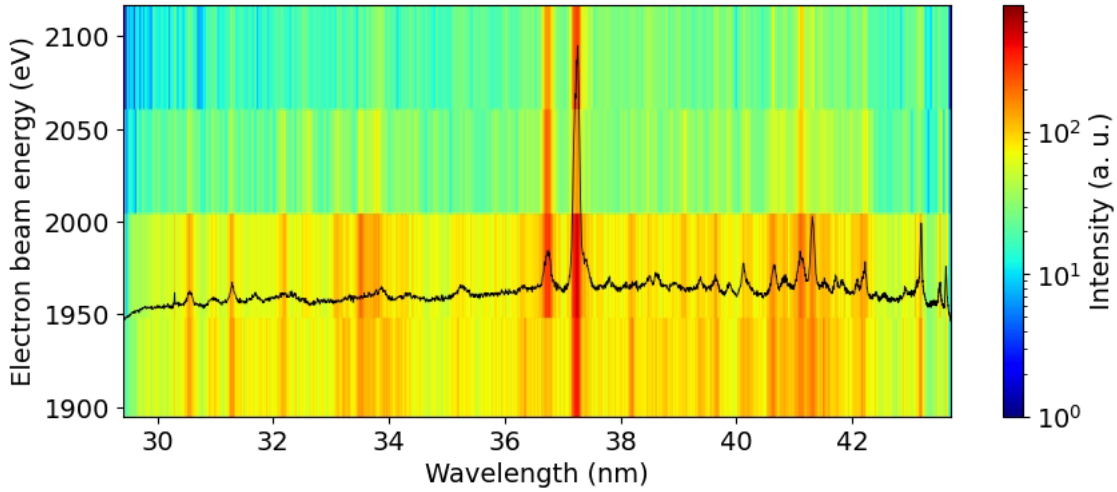

Figure 4.14: The static scan of Pb^{41+} is displayed on a section of the discrete energy scan of the EUV spectrometer to help distinguish weak lines from the noise

lines.

Transition 1: 40.6701 nm, $A_{ki} = 1.328 \cdot 10^5$ s^{-1}
Transition 2: 41.4224 nm, $A_{ki} = 1.134 \cdot 10^5$ s^{-1}
Transition 3: 43.3079 nm, $A_{ki} = 7.365 \cdot 10^4$ s^{-1}

The transitions are assumed to be within a range of the theoretical position and the theoretical position -0.8 nm. This value is the shift of the AMBiT spectrum, as suggested in Figure 4.13. This is because the calculation of the energy of the metastable state was conducted with the AMBiT data, which would also be shifted if the spectrum is shifted.
There are two scenarios that would explain the theoretical positions compared to the experimental positions. It can either be assumed that the theory was calculated without a shift or that the shift in Figure 4.13 is reliable.

I: When assuming that the shift, extracted from the previous energy scan of the theoretical calculations is not reliable, the most likely experimental line for transition 1 is the Gaussian labeled a in Figure 4.15. Transition 2 can either be the strong line b on the left of the theoretical line or the weak line c on the right side. The most probable line for transition 3 is the weak line d directly at the theoretical value. This agrees with the calculation that transition 3 is the weakest of the three.

II: When trusting the shift of the theoretical AMBiT calculations, there is an experimental transition at each newly calculated theoretical value. They are marked Gaussian e, g, and i in Figure 4.15. However, another set of experimental lines is visible slightly to the right of each line. These are labeled f, h, and j.

The possible line fits (see section 3.3.4) for these scenarios and the theoretical transitions are shown in Figure 4.15. The continuous vertical lines indicate the theoretical transitions, and the dashed lines indicate the theoretical lines shifted by $-0.8\,\mathrm{nm}$. Each Gaussian, fitted to a potential experimental transition, is labeled with a letter a-j. Their colors are the same color as the position of their corresponding theoretical line.

The positions λ_{exp} and intensities in counts of the Gaussians a-j and their errors are compared to the wavelengths λ_{theo} and spontaneous emission coefficients a_{ki} of the theoretical AMBiT transitions are displayed in Table 4.6. The errors of the intensities can again be calculated with the square roots of the counts. The errors of the wavelength are divided in statistic and systematic error. The statistic error is determined by the error of the Gaussian fit (see section 3.3.4) and the systematic error is determined by the errors of the calibration in equation (4.2).

Table 4.6: Comparison of theoretical AMBiT wavelengths λ_{theo} and spontaneous emission coefficients A_{ki} of the transitions (Tr.) 1-3 and experimental wavelengths λ_{exp} and counts of the relevant lines, fitted with Gaussians (Ga.) for the EUV range in two different scenarios (Sc.)

Sc.	Tr.	λ_{theo} (nm)	A_{ki} (s^{-1})	Ga.	λ_{exp} (nm)	Counts
I	1	40.6701	$7.365 \cdot 10^4$	a	$40.6517 \pm 0.0021(\mathrm{stat}) \pm 0.11(\mathrm{sys})$	762(28)
	2	41.4224	$1.134 \cdot 10^5$	b	$41.3146 \pm 0.0009(\mathrm{stat}) \pm 0.09(\mathrm{sys})$	1411(38)
				c	$41.499 \pm 0.006(\mathrm{stat}) \pm 0.07(\mathrm{sys})$	575(24)
	3	43.3079	$1.328 \cdot 10^5$	d	$43.423 \pm 0.005(\mathrm{stat}) \pm 0.007(\mathrm{sys})$	298(17)
II	1	40.6701	$7.365 \cdot 10^4$	e	$39.883 \pm 0.004(\mathrm{stat}) \pm 0.14(\mathrm{sys})$	529(23)
				f	$40.125 \pm 0.004(\mathrm{stat}) \pm 0.13(\mathrm{sys})$	740(27)
	2	41.4224	$1.134 \cdot 10^5$	g	$40.6518 \pm 0.0021(\mathrm{stat}) \pm 0.11(\mathrm{sys})$	762(28)
				h	$40.846 \pm 0.006(\mathrm{stat}) \pm 0.10(\mathrm{sys})$	603(25)
	3	43.3079	$1.328 \cdot 10^5$	i	$42.551 \pm 0.007(\mathrm{stat}) \pm 0.03(\mathrm{sys})$	402(20)
				j	$42.922 \pm 0.004(\mathrm{stat}) \pm 0.017(\mathrm{sys})$	473(22)

For scenario I, where the theory was not shifted, the possible experimental lines for transition 2 and lines b and c. When comparing their intensities to the ex-

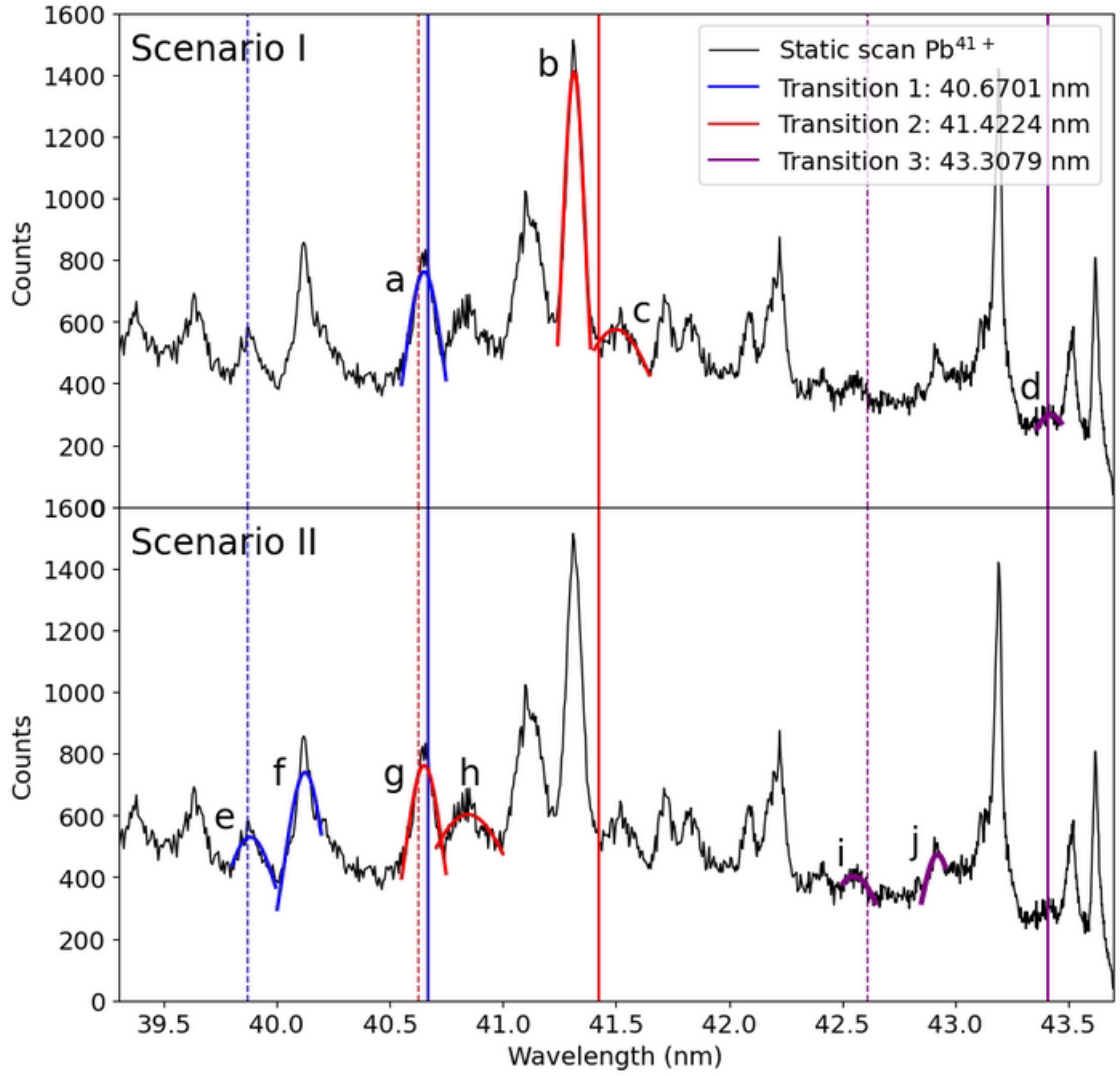

Figure 4.15: Scenarios for the theoretical transitions in the relevant section of the static measurement of the EUV spectrometer. The continuous vertical lines indicate the theoretical positions of the transitions, and the dashed vertical lines indicate the positions of the theoretical positions shifted by −0.8 nm, determined from the comparison of Pb^{41+} to the theoretical spectrum. The experimental lines, which may correspond to the theoretical lines, are fitted with Gaussians and labeled a-j. The colors of the dashed vertical lines and the Gaussians correspond to the theoretical positions of the continuous vertical lines. Scenario I is adapted to the theoretical positions and scenario II to the shifted theoretical position

perimental lines for transition 3 and 2 and the theoretical spontaneous emission coefficients in Table 4.6, experimental line c seems like the more probable option. In scenario II, there are six possible experimental lines, two for each theoretical transition. The distances between them should be similar to the theoretical calculations. Therefore, the possible combinations for the experimental lines are e, g, and i and f, h, and j. The positions of the former lines are similar to the shifted theory, but the latter has a better suiting intensity distribution.
The wavelength of the metastable state is then determined by adding transition 2 and 1 and then subtracting transition 3. The errors can be calculated by the error propagation for the addition and subtraction of uncorrelated errors

$$\Delta\lambda_{\mathrm{tot}} = \sqrt{(\Delta\lambda_1^2) + (\Delta\lambda_2)^2 + (\Delta\lambda_3)^2} \tag{4.6}$$

The result for each of the combinations (a, c, and d; e, g, and i; and f, h, and j) for the three transitions are

$$\begin{aligned} &\lambda_{\mathrm{acd}} = 38.692 \pm 0.022(\mathrm{stat}) \pm 0.13(\mathrm{sys})\,\mathrm{nm} \\ \Rightarrow\ &E_{\mathrm{acd}} = 32.044 \pm 0.010(\mathrm{stat}) \pm 0.011(\mathrm{sys})\,\mathrm{eV} \end{aligned}$$

$$\begin{aligned} &\lambda_{\mathrm{egi}} = 37.934 \pm 0.008(\mathrm{stat}) \pm 0.18(\mathrm{sys})\,\mathrm{nm} \\ \Rightarrow\ &E_{\mathrm{egi}} = 32.684 \pm 0.007(\mathrm{stat}) \pm 0.015(\mathrm{sys})\,\mathrm{eV} \end{aligned}$$

$$\begin{aligned} &\lambda_{\mathrm{fhj}} = 38.049 \pm 0.008(\mathrm{stat}) \pm 0.24(\mathrm{sys})\,\mathrm{nm} \\ \Rightarrow\ &E_{\mathrm{fhj}} = 32.585 \pm 0.007(\mathrm{stat}) \pm 0.020(\mathrm{sys})\,\mathrm{eV} \end{aligned}$$

The energies were calculated with equation (2.1).

4.3 VUV measurements

Simultaneously with the measurements with lead of the EUV spectrometer, measurements with the same settings were conducted with the VUV spectrometer. The spectral lines visible in the first order in the EUV range are visible in the second order in the VUV range. Therefore, a discrete energy scan was made to determine which lines belong to which charge state. In addition, a longer static measurement was conducted at the energy, where the spectrum of Pb^{41+} was expected. Both are compared to the theoretical spectra calculated with FAC and AMBiT, as explained in section 2.8.

4.3.1 Discrete electron energy scan

The same discrete energy scan of the EUV spectrometer was conducted with the VUV spectrometer with the settings listed in Table 3.3. This scan can be seen in Figure 4.16. Again, a logarithmic scale was chosen to bring out the weaker spectral lines, because of the very high count rates of the three strongest lines.

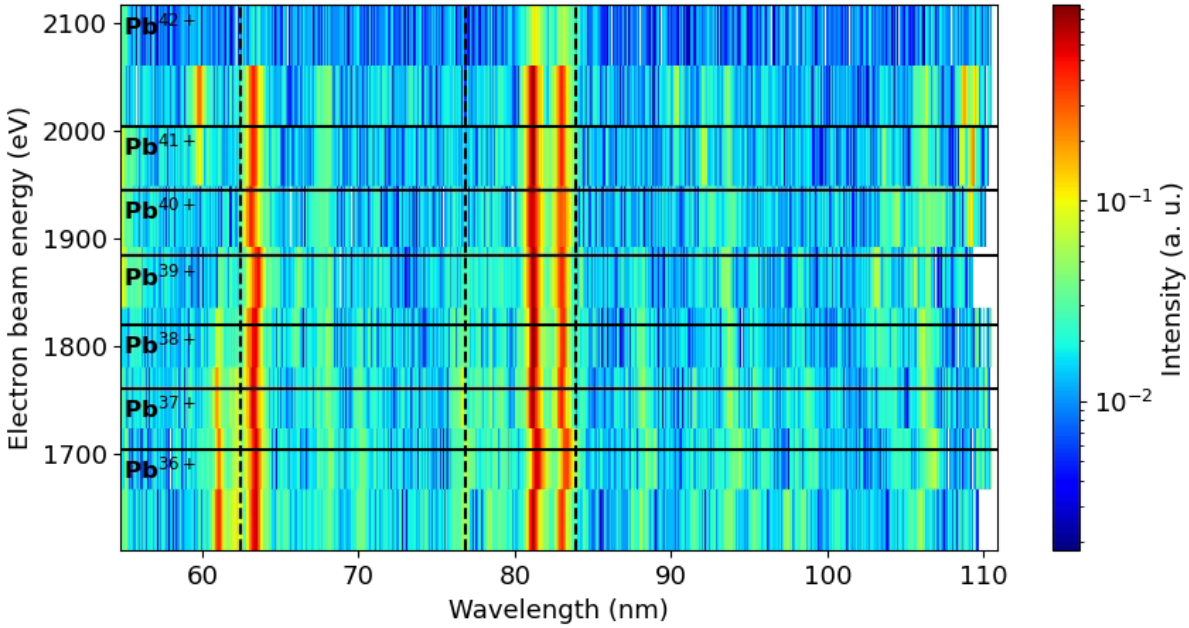

Figure 4.16: Discrete energy scan of lead, detected with the VUV spectrometer and corrected for space charge. The horizontal black lines indicate the ionization energies, taken from the NIST database [50], [51]. The corresponding charge states Pb^{36+} to Pb^{42+} are labeled on the right side of the diagram. The dashed vertical lines indicate theoretical positions of strong carbon lines [52]

When subtracting the space charge determined in section 4.1.3, the visible charge states are Pb^{36+} to Pb^{42+}. The ionization energy of each new charge state, taken from the NIST database [50], [51], is indicated with black horizontal lines. Again, the space charge was determined using a more profound trap than in this energy scan, but in section 4.2.1, it was argued that the determined space charge is viable regardless.
The dashed vertical lines in this scan are the second-order lines of the strong carbon lines of the NIST database, listed in Table 4.3. They are, therefore, found at

twice the wavelength. One can see that two of the carbon lines are close to spectral lines, which are continuously visible in the energy scan. This could indicate that these lines are carbon lines, and the weaker lines that appear or disappear belong to lead.
This assumption is valid, even though the carbon lines are not at the exact position of the strong lines in the discrete energy scan because of the stretching and compressing of the individual measurements towards other measurements, mentioned in section 4.1.4. This can be seen again in this energy scan. When calibrating the spectrometer, the measurements were used where the lines shifted the least compared to other measurements. However, the lines in this spectrum may all be stretched or compressed compared to the energy scan with neon. Therefore, the calibration is only reliable until the largest shift, which was $\lambda_{\text{shift}} = 0.35\,\text{nm}$. The shift of the carbon lines are $\lambda_{\text{left}} = 0.48\,\text{nm}$ and $\lambda_{\text{right}} = 0.37\,\text{nm}$.
Even though these values are both larger than the furthest shift, it is a reasonable explanation because the three lines visible in every step of the energy scan have a distinguishable structure compared to other spectral lines. Therefore, it is assumed that only the lines that appear or disappear during this energy scan belong to lead. The third strong line does not seem to be part of carbon because there are no strong first- or second-order lines at this wavelength. However, it could belong to an intense line of a previous charge state and is, therefore, irrelevant to the analysis.

This energy scan can also be compared to the theory calculated with FAC and AMBiT(see section 2.8). They are displayed like the discrete energy scan in Figure 4.17.
The calculation to get the spectrum from the theoretical data points is the same as for the EUV spectrometer in section 4.2.1. However, the second order of the theoretical spectral lines of the EUV wavelength range was added to the theoretical lines found in the VUV range. Therefore, the theoretical VUV spectra are a combination of second- and first-order lines. Since only a few theoretical lines are in the VUV range, the spectra may look similar to the theoretical EUV spectra.
Again, a square root scale was chosen for the theoretical energy scans in Figure 4.17 because it mitigates the impact of extreme values, making the visualization more balanced compared to a logarithmic scale.

4.3.2 Static measurement

After the discrete energy scan, a longer static measurement was conducted at the energy, at which Pb^{41+} was expected. This can be seen in Figure 4.18 along

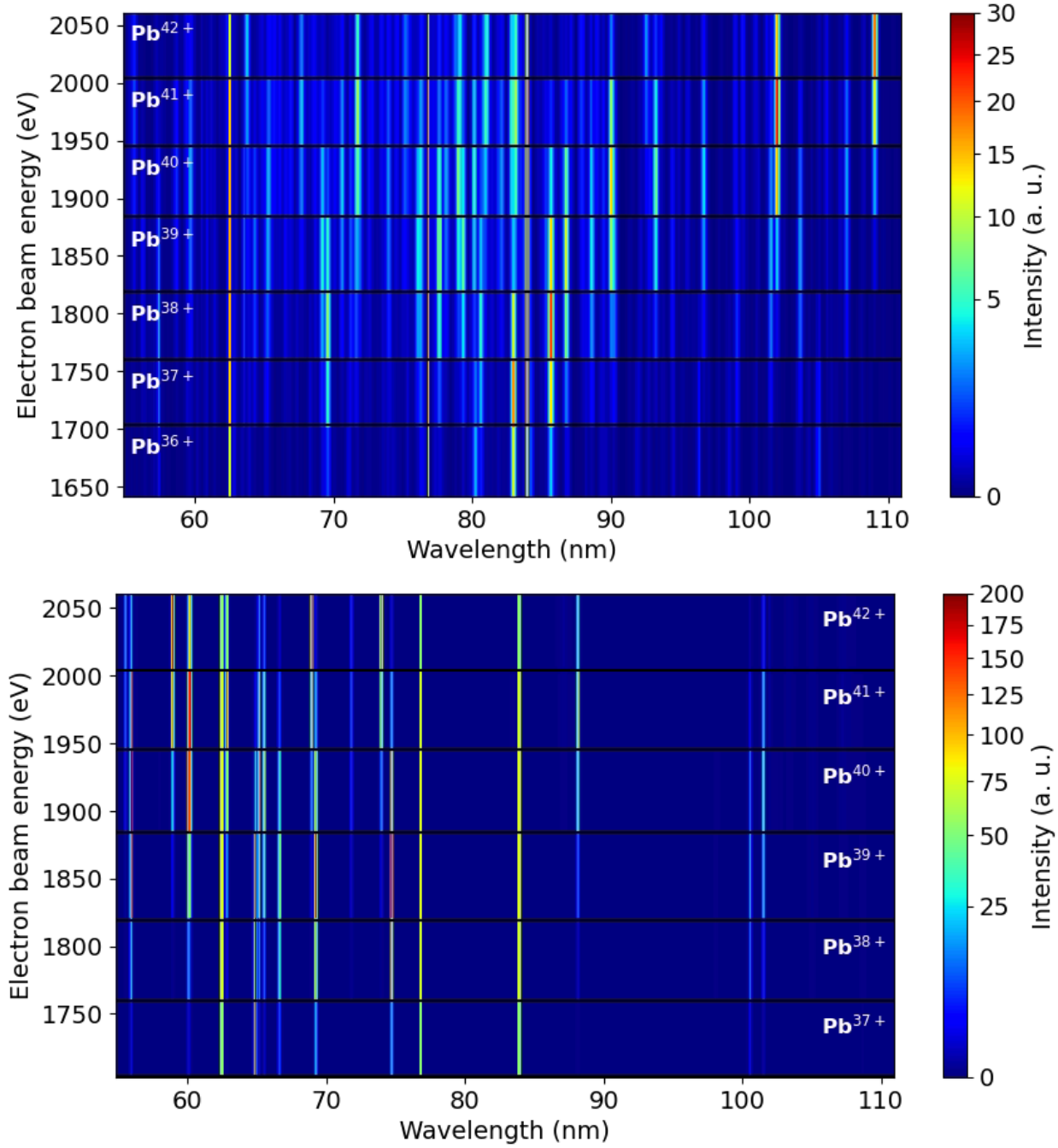

Figure 4.17: Theoretical calculations of different charge states for the VUV wavelength range **top:** with FAC for Pb^{36+} to Pb^{42+} and **bottom:** with AMBiT for Pb^{37+} to Pb^{42+}. The horizontal black lines indicate the ionization energies, taken from the NIST database [50], [51]. The corresponding charge states are labeled on the right and left sides of the diagram. In addition, the strongest spectral lines of carbon are displayed as continuous spectral lines in every charge state

with a section of the discrete energy scan to better compare the long and short measurements.

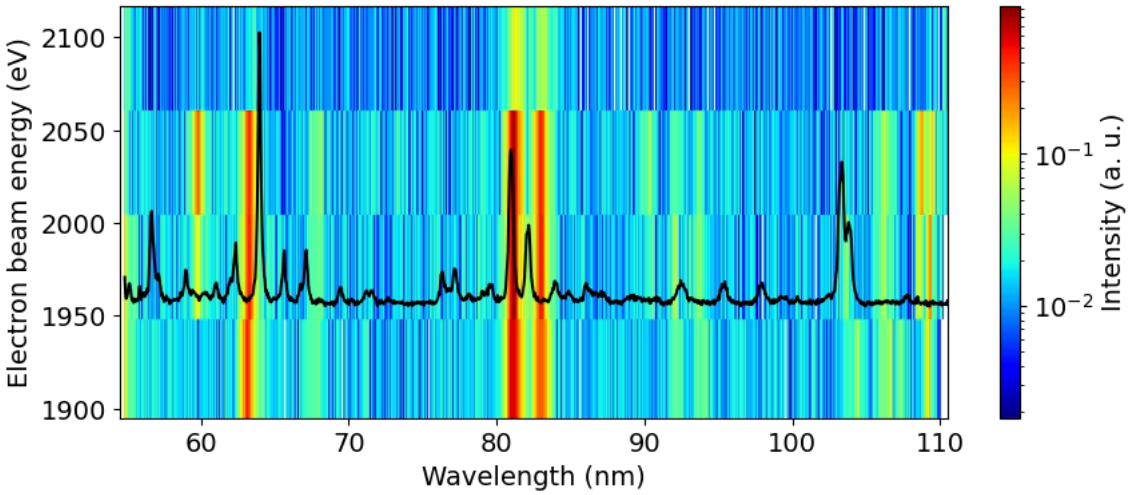

Figure 4.18: The static scan of Pb^{41+} is displayed on a section of the discrete energy scan of the VUV spectrometer to help distinguish weak lines from the noise

The issue of the stretching and compressing of the individual spectra can be seen again in Figure 4.18. It is especially visible for the three strongest lines because two of them are not at the same position as the measurements of the discrete energy scan. Furthermore, some stronger lines are seen in the static spectrum, which cannot be identified in the energy scan. Especially the lines at around 56.5 nm, 62 nm, and 65.5 nm. On the right side of the spectrum, some stronger lines are visible in the energy scan but are not distinguishable from the noise in the static measurement.
These differences in the measurement can be attributed to the slightly different settings of the EBIT parameter in these measurements (see Tables 3.1 and 3.3), such as the voltage of the focus electrode, the drift tube bias, the bucking coil voltage, and the dump settings. However, these differences are not seen in the EUV spectrometer (Figure 4.14). Therefore, another reason could be some residual gas from other measurements, which does not have strong lines in the EUV wavelength range.
Due to these differences between the discrete energy scan and the static measurement, as well as the differences between the individual measurements of the energy scan, a detailed comparison to the theoretical spectra seems to have little practical use or importance within the context of this thesis.

However, the energy of the metastable state can be calculated when assuming that the transitions are visible in the second order, and the shift of the AMBiT calculation, determined in Figure 4.13 is also valid here. Therefore, the values for the theoretical transitions are double the values used in section 4.2.2, and the shift also doubled to −1.6 nm. Continuous vertical lines mark the theoretical transitions, and dashed vertical lines mark the theoretical transition −1.6 nm in Figure 4.19
As mentioned in section 4.1.4, the line width of the spectral lines is larger in the longer static scan with $\sigma_{\text{long}} = 0.3\,\text{nm}$ than in the shorter steps of the discrete energy scan with $\sigma_{\text{short}} = 0.05\,\text{nm}$. This is due to the stretching and compressing of the spectrum over time. Therefore, there are fewer spectral lines within the theoretical value for the transitions and the shifted values for the transitions.
The position of these lines can be determined with a Gaussian least-square fit, as described in section 3.3.4. They are displayed in Figure 4.19 and labeled k-m.

The results of the positions λ_{exp}, errors, and intensity I for the comparison to the theoretical AMBiT wavelength λ_{theo} and spontaneous emission coefficient A_{ki} are displayed in Table 4.7. The intensity errors are not calculated because when creating the spectrum, the intensities are time-normalized with the time spent at each specific angle. Therefore, the values are often lower than 1, so the errors would be larger than the values. The errors of the wavelength are divided in statistic and systematic error. The statistic error is determined by the error of the Gaussian fit (see section 3.3.4) and the systematic error is determined by the errors of the calibration in equation (4.5). In addition to the errors of the calibration, the systematic error also contains the error of the maximum shift 0.35 nm seen in the energy scan in Figure 4.8. The resulting error is calculated via the error propagation in equation (4.6).

Table 4.7: Comparison of theoretical AMBiT wavelengths λ_{theo} and spontaneous emission coefficients A_{ki} of the theoretical transitions (Tr.) 1-3 and experimental wavelengths λ_{exp} and intensities I of the relevant lines for the VUV range, which are fitted with Gaussians (Gauss.)

Tr.	λ_{theo} (nm)	A_{ki} (s^{-1})	Gauss.	λ_{exp} (nm)	I (a. u.)
1	81.3402	$7.365 \cdot 10^4$	k	$80.979 \pm 0.005(\text{stat}) \pm 1.7(\text{sys})$	0.234
2	82.8448	$1.134 \cdot 10^5$	l	$82.133 \pm 0.006(\text{stat}) \pm 1.8(\text{sys})$	0.130
3	86.6158	$1.328 \cdot 10^5$	m	$86.132 \pm 0.020(\text{stat}) \pm 1.8(\text{sys})$	0.054

The wavelength for the transition of the metastable to the ground state in the second order can again be calculated by adding transition 2 and 1 and then subtracting transition 3. To get the result in the first order, this value has to be

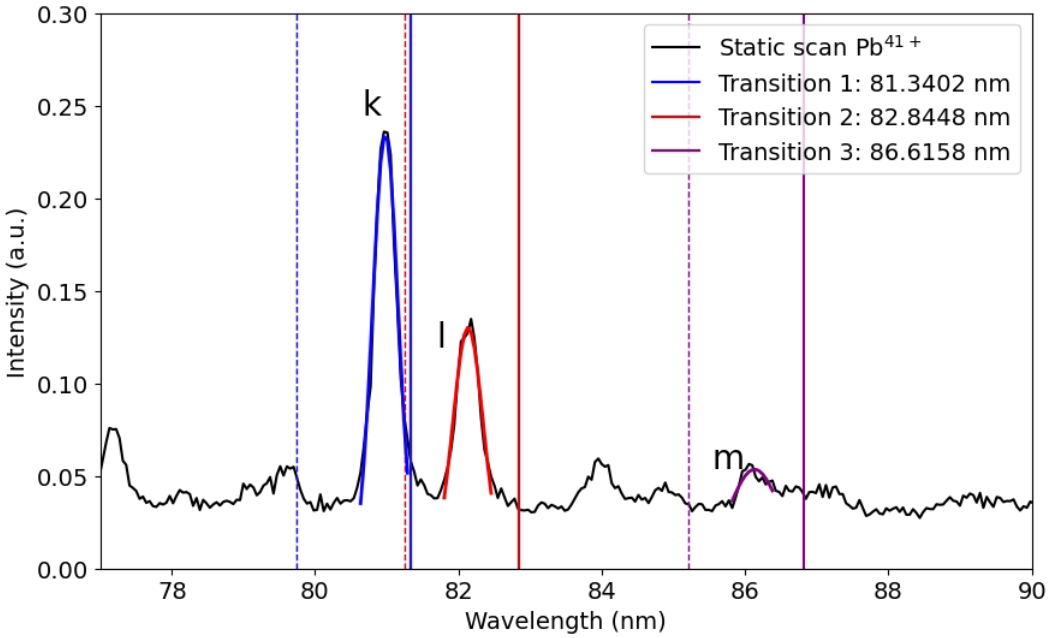

Figure 4.19: Possible experimental lines for the theoretical transitions in the relevant section of the static measurement with the VUV spectrometer. The continuous vertical lines indicate the theoretical positions of the transitions, and the dashed vertical lines indicate the positions of the theoretical positions shifted by $-1.6\,\mathrm{nm}$, determined from the comparison of Pb^{41+} to the theoretical spectrum. The experimental lines, which may correspond to the theoretical lines, are fitted with Gaussians and labeled k-m. The colors of the dashed vertical lines and the Gaussians are corresponding to the theoretical positions of the continuous vertical lines

divided by two. The error can be calculated by the error propagation, given in equation (4.6). The result is:

$$\begin{aligned} 2\lambda_{\mathrm{klm}} &= 76.98 \pm 0.20(\mathrm{stat}) \pm 3(\mathrm{sys})\,\mathrm{nm} \\ \lambda_{\mathrm{klm}} &= 38.49 \pm 0.10(\mathrm{stat}) \pm 1.5(\mathrm{sys})\,\mathrm{nm} \\ \Rightarrow\quad E_{\mathrm{klm}} &= 32.21 \pm 0.08(\mathrm{stat}) \pm 1.2(\mathrm{sys})\,\mathrm{eV} \end{aligned}$$

The energy was calculated using equation (2.1).

5 Summary and discussion

The spectra of different charge states of highly charged lead were analyzed using the FLASH-EBIT at the Max-Planck Institute for Nuclear Physics to determine the energy of a metastable state in Pb XLII. This metastable state is a potential extreme ultraviolet (XUV) clock transition and can contribute to the research of optical atomic clocks.
For this, gaseous tetraethyl lead was injected into the EBIT and collisionally ionized by the electron beam. The different charge states were produced by varying the kinetic energy of the electrons, and the energy at which Pb^{41+} is visible was determined. A longer measurement was conducted at this energy to get more defined lines and to be able to distinguish weak lines from the noise. The results were compared to the theoretical spectra, calculated with FAC and AMBiT.

Before starting with the measurement for the main part, the EUV spectrometer was moved from its original place to be able to measure wavelengths in the relevant range between 40 nm and 44 nm. The spectrometer can detect wavelengths in this range but was designed for wavelengths between 5 nm and 35 nm, and therefore, has a lower efficiency. By using a spectrometer more suited for this wavelength, the efficiency can be increased.
The space charge of the electron beam is responsible for the radial trapping of the HCIs, but the energy that is set has to be corrected to get the real electron beam energy. When determining the space charge, it was assumed that a deeper trap was preferred when trapping highly charged lead ions. Therefore, the measurements were conducted with a deep trap. During later measurements, it became clear that a shallower trap increased the count rate, especially in the VUV spectrometer. For the measurements in the main part, a shallow trap was used, but the energy was corrected with the space charge using a deep trap. When looking at the appearing and disappearing spectral lines in the discrete energy scan conducted with lead, it can be argued that the determined space charge is reasonable. This can be explained by the low injection pressure and, therefore, a limited amount of ions in the trap, which contribute to the space charge. However, a measurement to confirm this would be useful.
In addition, the space charge was only determined for the high electron beam energies used during lead measurements and not for the lower energies used for the

calibration with neon. The approximation at high energies is inaccurate because the errors increase substantially due to the wide extrapolation and the compensation of the space charge by the trapped ions. The space charge was estimated according to appearing spectral lines, but an additional measurement for an exact determination can improve the calibration.
In the discrete energy scan of neon in the VUV spectrometer, some shifts are visible in the spectral lines, which makes it clear that individual measurements are stretched or compressed towards other measurements. When calibrating the spectrometer, only measurements whose spectral lines aligned most with the rest of the energy scan were used. However, it is possible that these differ from other measurements, and therefore, the calibration accuracy is constrained. The calibration is only deemed reliable within a margin of error equivalent to the maximum observed shift in any measurement.
For both calibrations, a χ^2_{red} significantly under the optimal value 1 was determined. This suggests that the errors for the calibration were overestimated. A possible explanation for this it that the errors of the NIST database are slightly overestimated. The errors stemming from the fit of the line position could be reduced by taking longer measurements so the peaks are more defined and better fit the Gaussian profile.
The stretching and compressing of the individual measurements can be attributed to the rotation stage used to generate rotations or the rotary encoder, which measures the angle of the grating. This problem can be resolved by scaling each measurement with at least two strong carbon lines visible in different areas of the spectrum. These may also serve as a calibration because if the calibration is done in a different measurement, the spectra may shift between the calibration and the following measurement.
From the data used for the calibration, the resolution of the spectrometers was determined. The resolution was higher for the VUV spectrometer than the EUV spectrometer, which can be expected because some spectral lines can be seen in the second order in the VUV spectrometer. The lines become narrower in the second order, and the wavelength increases, which enhances the resolution. However, the errors stemming from the standard deviation of the calculations are high due to the varying width of the lines. It is possible that some of these are two lines close to each other, which have been fitted as one. To decrease this fitting error, longer measurements and more defined peaks are necessary.

After the preparatory measurements, lead was injected for the central part of the experiment, and a discrete energy scan was conducted. This energy scan comprises the charge states Pb^{36+} to Pb^{42+}. For a more certain determination of the charge states, it would be beneficial to have the spectra of the following charge

states as well. However, during the energy scan, the voltage of the cathode was increased and reached its maximum on the penultimate measurement. The last measurement was conducted by setting the drift tube bias high, which decreases the count rate. When going to even higher drift tube biases, the count rate declines even further, and in measurements with a longer duration, it is difficult to distinguish the spectral lines from the noise. This likely happens because some HCIs are produced outside the trap and drift into it, but if the drift tube bias is high, this process cannot happen.
In addition, the determination of the charge state of the ions could be determined by installing an extraction beamline. The ions cross an electric field, accelerating them differently according to their mass-to-charge ratio before reaching an extractor. This can measure at what time specific ions reach the extractor. When comparing the signals to signals of known ions, the charge states can be determined more accurately and compared to the determination using the spectra of the different charge states to make sure the identification is correct.
The individual spectra of the discrete energy scan with the EUV spectrometer were then compared to the corresponding charge state of the theoretical calculations with FAC and AMBiT. It is noticeable that the calculations deviate from each other. This is because the open subshell is the $4d$-shell, which has ten electrons or holes depending on the charge state. This makes the calculations very complex, and slight configuration differences can greatly impact the spectrum. Especially for Pb^{41+}, the relevant charge state, which has the configuration $4d^5$, which has the same amount of electrons and holes in the subshell. It, therefore, has the most possible allowed terms of any open nd^q shell [10].
Furthermore, when equating the collisional excitation rate with the radiative deexcitation rate in the FAC calculations, some values for the electron energy and density have to be included in the calculation. The electron energy was determined for each charge state using the experimental setup, and the electron density was chosen to be $5 \cdot 10^{10}$ cm^{-3}. Since these values are not included in the AMBiT calculations, this could lead to further differences between the spectra.
For comparing experiment and theory, the theoretical spectra were shifted to fit the experimental spectra better. When calculating the FAC spectra, it is difficult to precisely determine the energy of the ground state, which creates a shift in the whole spectrum. This is less of a problem when using the many-body perturbation theory like AMBiT, but a short shift can still be expected. When comparing the shift of the FAC and AMBiT is towards the left or right depending on the spectrum. The same error in determining the ground state is likely made in all calculations; therefore, all spectra are shifted in the same direction. However, some theoretical spectra are only shifted to fit one line of the experimental spectrum, which makes the shift less significant. The relevant shift for Pb^{41+} was based on a few FAC and

AMBiT lines, which were also aligned with each other.
After identifying the charge state Pb^{41+} and the corresponding shift of the theoretical calculations, the line positions of the relevant transitions were determined using a static measurement of longer duration. The three transitions needed to infer the metastable state were chosen according to their position in the range of the theoretical transitions and the shift toward the right, as determined by comparing the discrete energy scan to the theory. There are three combinations for calculating the energy of the metastable state using the measurements of the EUV spectrometer: $E_{\mathrm{acd}} = 32.044 \pm 0.010(\mathrm{stat}) \pm 0.011(\mathrm{sys})\,\mathrm{eV}$, $E_{\mathrm{egi}} = 32.684 \pm 0.007(\mathrm{stat}) \pm 0.015(\mathrm{sys})\,\mathrm{eV}$, and $E_{\mathrm{fhj}} = 32.585 \pm 0.007(\mathrm{stat}) \pm 0.020(\mathrm{sys})\,\mathrm{eV}$. The energy E_{adc} was determined with the experimental lines closest to the original theoretical values, while the energy E_{egi} was determined with experimental lines closest to the shifted theoretical line and the energy E_{fhj} was determined with experimental lines in between the other two.
The least plausible combination for calculating the energy is E_{fhj} because it uses neither the original nor the shifted theoretical transitions for the calculation. When shifting the theoretical spectrum by the difference between these experimental positions to the theoretical spectrum, the other theoretical transitions do not align with the experimental results of the discrete energy scan. It can also be assumed that the combination for calculating the energy E_{egi} is inaccurate because the intensity distributions of the experimental and theoretical lines do not match. Furthermore, the shift of the theoretical spectrum is larger than expected for AMBiT calculations. Therefore, the energy of the metastable state determined with the EUV spectrometer is expected to be the calculation with the unshifted theory $E_{\mathrm{EUV}} = 32.044 \pm 0.010(\mathrm{stat}) \pm 0.011(\mathrm{sys})\,\mathrm{eV}$
In [1], the energy of this metastable state was determined to be 31.2(8) eV and it was compared to two partially different ab initio multiconfiguration Dirac-Hartree-Fock calculations of 31.68(13) eV and 31.76(35) eV. The value determined in this experiment deviates from the value in the other experiment by 1.0σ and to the theoretical values by 2.8σ and 0.8σ. Therefore, the result determined in this experiment agrees with the result of [1] and one of the theoretical calculations.
The same discrete energy scan and static measurement were conducted with the VUV spectrometer, but in the energy scan, the stretching and compressing of the individual measurements are visible, as mentioned earlier. It, therefore, becomes difficult to determine the position of spectral lines and to identify if an appearing line is a new spectral line or a shifted line from a previous charge state. When displaying the discrete energy scan in the same graph as the spectrum obtained from the static measurement, it becomes clear that the line positions and intensities differ from each other.
When comparing the static VUV spectrum to the theoretical determination of

the transitions and again choosing a combination with an intensity distribution similar to the theoretical one, the energy of the metastable state is determined as $32.21 \pm 0.08(\text{stat}) \pm 1.2(\text{sys})$ eV. This deviates by 0.1σ to the value calculated with the measurement of the EUV spectrometer, by 0.7σ to the experimental value in [1] and by 0.4σ and 0.4σ to the theoretical values stated in [1]. These deviations are lower than the results of the EUV spectrometer, but this is mainly due to the high statistical error, which stems from the calibration and the maximum shift observed in the discrete energy scan with neon.
While a result has been obtained, the numerous errors due to the shifting of spectral lines have to be acknowledged, rendering the outcome highly likely to be inaccurate. Consequently, the obtained result is considered irrelevant for this experiment.
In order to further improve the resolution of the spectral lines, a charge-coupled device (CCD) [53] could be installed in the EUV spectrometer instead of an MCP. However, the MCP was chosen for both spectrometers because it can provide information on the time of each event. This is crucial for energy ramp measurements. The time resolution needed for these measurements cannot be achieved by a CCD.

This precision measurement of a potential XUV-clock transition in highly charged lead is a step forward in finding stable clocks in the XUV range. For future advancements in optical atomic clocks, more metastable transitions at high energies, such as the one presented in [1] and investigated in this thesis, have to be detected. Furthermore, the transition of this metastable state could be determined with even higher accuracy with laser spectroscopy before it is tested in an atomic clock. The high precision of optical clocks allows the exploration of fundamental principles in physics. Furthermore, these findings have broader implications for exploring physics beyond the standard model. Therefore, it is important to keep working on the research on optical clocks.

A Lists

A.1 List of Figures

A.2 List of Tables

B Bibliography

[1] K. Kromer et al. “Observation of a Low-Lying Metastable Electronic State in Highly Charged Lead by Penning-Trap Mass Spectrometry”. In: *Phys. Rev. Lett. 131, 223002* (2023).

[2] A. D. Ludlow et al. “Optical atomic clocks”. In: *Rev. Mod. Phys. 87, 637* (2015).

[3] E. R. Clements et al. “Lifetime-Limited Interrogation of Two Independent 27Al+ Clocks Using Correlation Spectroscopy”. In: *Phys. Rev. Lett. 125, 243602* (2021).

[4] L. Maleki J. D. Prestage R. L. Tjoelker. “Atomic clocks and variations of the fine structure constant”. In: *Phys. Rev. Lett. 74, 3511* (1995).

[5] R. Godun et al. “Frequency ratio of two optical clock transitions in 171Yb+ and constraints on the time variation of fundamental constants”. In: *Phys. Rev. Lett. 113, 210801* (2014).

[6] R. Lange et al. “Improved limits for violations of local position invariance from atomic clock comparison”. In: *Phys. Rev. Lett. 126, 011102* (2021).

[7] L. S. Brown and G. Gabrielse. “Geonium theory: Physics of a single electron or ion in a Penning trap”. In: *Rev. Mod. Phys. 58, 233* (1986).

[8] M. A. Levine et al. “The Electron Beam Ion Trap: A New Instrument for Atomic Physics Measurements”. In: *Physica Scripta. Vol. T22, 157-163* (1988).

[9] W. Demtröder. *Atoms, Molecules and Photons. An Introduction to Atomic-, Molecular- and Quantum Physics*. Springer, 2010.

[10] E. Träbert P. H. Heckmann. *Introduction to the Spectroscopy of Atoms*. North-Holland Personal Library, 1989.

[11] C. F. Fischer. *Hartree-fock method for atoms. A numerical approach*. Wiley, 1977.

[12] E. M. Siegbahn. *The configuration interaction method, Lecture Notes in Quantum Chemistry*. Springer, 1992.

[13] M. F. Gu. “The flexible atomic code”. In: *Canadian Journal of Physics, 86(5):675–689* (2008).

[14] J. C. Berengut E. V. Kahl. “AMBiT: A program for high-precision relativistic atomic structure calculations”. In: *Computer Physics Communications, Vol. 238* (2018).

[15] M. F. Gu. “Indirect x-ray line-formation processes in iron L-shell ions”. In: *The Astrophysical Journal, 582:1241-1250* (2003).

[16] V. A. Dzuba et al. “Combination of the many-body perturbation theory with the configuration-interaction method”. In: *Physical Review A. Vol. 54 nr. 5* (1996).

[17] Z. Harman J. Crespo López-Urrutia. *Emission and Laser Spectroscopy of Trapped Highly Charged Ions in Electron Beam Ion Traps*. Springer, 2014.

[18] W. Lotz. “An Empirical Formula for the Electron-Impact Ionization Cross-Section”. In: *Zeitschrift ftir Physik 206, 205–211* (1967).

[19] M. A. Levine et al. “The Electron Beam Ion Trap: A New Instrument for Atomic Physics Measurements”. In: *Phys. Scr. 1988 157* (1987).

[20] S. Dobrodey. “Charge-exchange studies of bare and hydrogen-like low-Z ions in the X-ray and extreme-ultraviolet ranges inside an electron beam ion trap”. PhD thesis. Ruperto-Carola-University of Heidelberg, Germany, 2019.

[21] S. W. Epp. “Röntgen–Laserspektroskopie hochgeladener Ionen in einer EBIT am Freie–Elektronen–Laser FLASH”. PhD thesis. Ruperto-Carola-University of Heidelberg, Germany, 2007.

[22] G. Herrmann. “Optical theory of thermal velocity effects in cylindrical electron beams”. In: *Journal of Applied Physics, 29(2):127–136* (1985).

[23] R. F. Steinbrügge. “Weiterentwicklung eines Geschwindigkeitsfilters zur Beobachtung ladungsändernder Prozesse hochgeladener Ionen (Unveröffentlichte Dissertation)”. PhD thesis. Ruperto-Carola-University of Heidelberg, Germany, 2010.

[24] T. Baumann. “Entwicklung eines Gitterspektrometers zur Untersuchung vakuumultravioletter Strahlung von hochgeladenen Ionen”. PhD thesis. Ruperto-Carola-University of Heidelberg, Germany, 2008.

[25] J. L. Wiza. “Microchannel plate detectors”. In: *Reprinted from Nuclear Instruments and Methods, Vol. 162, pages 587 to 601* (1979).

[26] P. Bolton et al. “Instrumentation for diagnostics and control of laser-accelerated proton (ion) beams”. In: *Physica Medica 30 255 270* (2013).

[27] M. B. Williams S. E. Sobottka. “Delay line readout of microchannel plates”. In: *348 IEEE Transactions on Nuclear Science, Vol. 35, No. 1* (1988).

[28] K. D. Berry et al. “A Neutron Sensitive Microchannel Plate Detector with Cross Delay Line Readout”. In: *IEEE Nuclear Science Symposium Conference Record 192-198* (2012).

[29] M. Botz. *Experimental Determination of Relative Electron Collision Excitation Cross Sections of Highly Charged Tin in an EBIT*. 2022.

[30] M. A. Blessenohl. “Fine-structure investigations in highly charged ions using spectroscopy in the vacuum ultraviolet regime”. PhD thesis. Ruperto-Carola-University of Heidelberg, Germany, 2020.

[31] H. A. Rowland. “XXIX. On concave gratings for optical purposes”. In: *The London, Edinburgh, and Dublin Philosophical Magazine and Journal of Science, vol. 16(99), pages: 197–210* (1883).

[32] C. Martin et al. “Wedge-and-strip anodes for centroid-finding position-sensitive photon and particle detectors”. In: *Rev. Sci. Instrum. 52, 1067–1074* (1981).

[33] A. C. Laforge. “Three-Body Dynamics in Single Ionization of Atomic Hydrogen by 75 keV Proton Impact”. In: *Physical Review Letters 103(5):053201* (2009).

[34] P. Lechner et al. “Silicon drift detectors for high count rate X-ray spectroscopy at room temperature”. In: *Nuclear Instruments and Methods in Physics Research A 458 (2001) 281-287* (2001).

[35] H. Weiß Y. A. W. Shardt. *Methoden der Statistik und Prozessanalyse, Eine anwendungsorientierte Einführung*. Springer, 2021.

[36] *SciPy documentation, Version: 1.12.0*. 2024.

[37] A. E. Kramida and G. Nave. “New FTS Measurements, Optimized Energy Levels and Refined VUV Standards in the Ne III Spectrum”. In: *Eur. Phys. J. D 37, 1–21* (2006).

[38] A. E. Kramida et al. “A Critical Compilation and Extended Analysis of the Ne IV Spectrum”. In: *Eur. Phys. J. D 7, 525–546* (1999).

[39] A. E. Kramida et al. “A Critical Compilation and Extended Analysis of the Ne V Spectrum”. In: *Eur. Phys. J. D 7, 547–565* (1999).

[40] A. E. Kramida et al. “Ne IV Spectrum”. In: *J. Opt. Soc. Am. B 16, 1966–1987* (1999).

[41] A. E. Kramida and M.-C. Buchet-Poulizac. “Energy Levels and Spectral Lines of Ne VII”. In: *Eur. Phys. J. D 38, 265–276* (2006).

[42] A. E. Kramida and M.-C. Buchet-Poulizac. “Energy Levels and Spectral Lines of Ne VIII”. In: *Eur. Phys. J. D 39, 173-188* (2006).

[43] H. D. Polster F. W. Paul. “The Extreme Ultraviolet Spectra of Ne IV, V and VI”. In: *Phys. Rev. 59, 424–430* (1941).

[44] S. Lindeberg. “An Experimental Analysis of the Energy Levels with n=2 in the Spectra Ne IV, V, VI and VII”. In: *Uppsala Univ. Inst. Phys. Report UUIP-759* (1972).

[45] J. W. Brosius et al. “SERTS-95 Measurements of Wavelength Shifts in Coronal Emission Lines Across a Solar Active Region”. In: *Astrophys. J. 526, 494–504* (1999).

[46] A. E. Kramida et al. “Extension and New Level Optimization of the Ne IV Spectrum”. In: *Phys. Scr. 85, 025303* (2012).

[47] A. K. Pradhan D. Luo. “Atomic data for opacity calculations: XI. The carbon isoelectronic sequence”. In: *J. Phys. B 22, 3377–3395* (1989).

[48] J. A. Fernley et al. “Atomic data for opacity calculations: XXIV. The boron-like sequence”. In: *J. Phys. B 32, 5507–5522* (1999).

[49] J. A. Tully et al. “Atomic data for opacity calculations: XIV. The beryllium sequence”. In: *J. Phys. B 23, 3811–3837* (1990).

[50] T. A. Carlson et al. “Calculated Ionization Potentials for Multiply Charged Ions”. In: *At. Data Nucl. Data Tables 2, 63–99* (1970).

[51] G. C. Rodrigues et al. “Systematic Calculation of Total Atomic Energies of Ground State Configurations”. In: *At. Data Nucl. Data Tables 86, 117–233* (2004).

[52] B. Edlén. “Wellenlängen und Termsysteme zu den Atomspectren der Elemente Lithium, Beryllium, Bor, Kohlenstoff, Stickstoff und Sauerstoff,” in: *Nova Acta Reg. Soc. Sci. Upsalien., Ser. IV 9(6), 1–153* (1934).

[53] S. B. Howell. “Handbook of CCD astronomy, volume 5”. In: *Cambridge University Press* (2006).

Acknowledgements

I want to thank all the people who supported and helped me in the course of this thesis. First of all, José for allowing me to conduct this experiment and contribute with my own ideas. He also took his time to discuss my results and answer my questions when no one was around to help me.
I also want to thank Thomas for taking on the second correction of this thesis.
Special thanks to Marc, who helped me throughout the whole process and gave me hints on conducting useful measurements. In addition, he answered all of my questions, no matter how trivial or difficult, and even provided remote help when he was not at the institute. I greatly appreciate the countless and last-minute comments and tips on improving this thesis, without which I would have overlooked several mistakes.
I would also like to extend thanks to Moto for taking the time to try to make sense of some puzzling data and for the constructive criticism of my thesis.
I also want to thank Nils and Karl for helping me with the AMBiT calculations and Ruben for proofreading my thesis and giving me suggestions for improvement.
Lastly, I want to thank everyone in the work group who contributed to the pleasant lunch breaks.